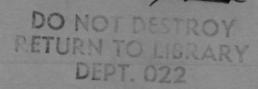
NASA Technical Memorandum 85702



Research and Technology

1983 Annual Report of the Langley Research Center



NASA

19 DEC' 1983

MCDONA

RESEARCH & ENGINEERING LIBRARY

ST. LOUIS

Foreword

The role of the Langley Research Center is to engage in the basic and applied research necessary for the advancement of aeronautics and space flight, to generate new and advanced concepts for the accomplishment of related national goals, and to provide research advice, technological support, and assistance to other NASA installations, other government agencies, and industry. This Langley Research Center 1983 Annual Report on Research and Technology contains highlights of our major accomplishments and applications made during the past year. The highlights illustrate both the broad range of the research and technology activities at the Langley Research Center and the contributions of this work toward maintaining United States leadership in aeronautics and space research. For further information about the report contact Robert H. Tolson, Chief Scientist, Mail Stop 103, Langley Research Center, Hampton, Virginia 23665, (804) 865-3316.

Donald P. Hearth

Director

Availability Information

The NASA program office and the corresponding Agency-wide Research and Technology Objectives and Plans (RTOP) work breakdown structure are listed for each research and technology accomplishment in the Contents. OAST designates the Office of Aeronautics and Space Technology; OSSA designates the Office of Space Science and Applications; AD designates the Deputy Administrator; OER designates the Office of External Relations; and OSF designates the Office of Space Flight.

For additional information on any summary, contact the individual identified with the highlight. This individual is generally either a member or a leader of the research group submitting the highlight. Commercial telephone users may dial the listed extension preceded by (804) 865. Telephone users with access to the Federal Telecommunications System (FTS) may dial the extension preceded by 928.

CONTENTS

Foreword	
Availability Information	ij
Aeronautics Directorate	
Aeronautics Directorate	1
Three-Dimensional Navier-Stokes Code for Scramjet Inlet Flow Field]
Supersonic Shear Flow Past a Circular Cylinder	2
Cartesian Finite-Volume Transonic Potential Method	3
Improved Efficiency in Solutions of Inviscid Transonic Rotational Flow	3
Validation of a Three-Dimensional Transonic Wing-Body-Pod-Pylon-Winglet Computer Code	4
OAST (505-31-03)	
Turbulent Drag Reduction Using Longitudinal Surface Grooves	
Vortex Flap Shaping	5
An Investigation of Aft-Mounted Nacelles on a Supercritical Wing	5
Compressibility Correction for Eppler Airfoil Program	6
CAST 10-2 Airfoil Studies With Sidewall Boundary Layer Removal	6
Development of Wind Tunnel Wall Interference Assessment/Correction (WIAC)	
Methods for Three-Dimensional Transonic Flows	7
Orifice-Induced Pressure Error at High Reynolds Number	8
Wing Deflections and Pressures in Transonic Flow	9
Free-Flight Tests of Three-Surface Fighter Configuration	9
Subsonic Investigation of Cranked Wings Suitable for High-Maneuver Supersonic Fighters	0
Trimming Advanced STOL Fighter Configurations	1
Numerical Simulation of Shuttle Solid-Rocket Booster Ignition Transients	1
Leading-Edge Flows at Supersonic Speeds	1
Enhancement of Hydrogen and Hydrocarbon Combustion by Silane	2
Hydrocarbon Combustion Model for Scramjet Applications	3

	Aircraft Research (505-43-83)	14
	Characteristics of Light Twin Aircraft	14
General Avi	ation Stall/Spin Flight Tests	15
Insect Conta	amination Protection for Laminar-Flow Wings	15
	Electronics Directorate	
Electronics 1	Directorate	17
	ns and Flight Station Concepts for 1995 Transport Aircraft	17
	uter Graphics for Low-Cost Integrated Cockpit Displays	18
	LED Programmable Legend Switch Used for Multifunction Control	19
	grammable Display Generator Application	19
	ontroller for Advanced Transport Cockpit Design	20
	antages of a Stochastic Discrete Optimal-Output Feedback Program	20
	Estimation in Nonlinear Flight Regimes	21
Controls Co	ntrol Effectiveness Technique With Application to Aircraft ordination	21
	Design of Aircraft Using Optimization Techniques	22
	of Cloud Encounter on Long-Range Airline Routes	23
	cle Detector	24
	ng Reliability	24
	r Control With Simulated Transport Delays	24
	hniques for Interface Demarcation in Compound Semiconductors	25
	Microwave Radiometer	25
	Feedback Decoupler Demonstrated	26
	of Catalysts for Closed-Cycle Operation of CO ₂ Laser	26
Fiber Optic 2	(506-54-23) Zig-Zag Wavelength Demultiplexer Demonstrated	27
High-Density	y Wide-Temperature-Range Bubble Device	27

CMOS Sum-of-Products Integrated-Circuit Development	28
Feature Classification in Hardware OAST (506-58-13)	28
Adaptive Optic Nodes for Computer Networks	29
Information Adaptive System	30
Image Plane Processing of Visual Information	
Multiple-Beam Feeds in Large Space Antenna Systems	30
Computer Analysis of Shuttle Infrared Lee-Side Thermal Sensing Experimental Data OAST (506-63-34)	31
Computational Approach Resolves Questions on Chemistry of Fluorine Oxide Radical	31
Efficient Sparse Matrix Multiplication Scheme for CYBER 203	32
Integrated Verification and Testing System for HAL/S Programs	32
Database Processor	33
Design Methodology for Concurrent Systems	
Dynamic Pressure Standard Sets Accuracy of Wind Tunnel Data	
Raman Doppler Velocimeter Tests at Supersonic Speeds	
Method of Measuring Mixing Ratio of Film Cooling Nitrogen to Tunnel Gas	
Acoustic Radiation Stress in Solids	
Acoustic Ground Impedance Meter	
Noncontacting Suction Force Generator	36
Space Directorate	
Space Directorate	
OAST (506-51-13)	3/
Calculation of Radiation Effects Produced by Cosmic Rays Interacting With Matter OSSA (199-20-76)	38
Infrared Spectroscopic Measurements of Atmospheric Composition	38
Aerosols in the El Chichon Stratospheric Cloud	39

Remote-Sensing Applications	40
OSSA (665-40-40)	
Solar-Pumped Continuously Pulsed Laser	40
High-Angle-of-Attack Inviscid Flow Calculations Over a	4 1
Shuttle-Like Vehicle With Comparisons to Flight Data	41
Space Station System Synthesis	41
High-Quality Thin-Film Germanium Single Crystals	42
Heat Transfer on Space Shuttle Orbiter Models With	
Differentially Deflected Elevons	43
Future Space Transportation Systems Study OAST (506-63-23)	43
Hypersonic Flow Characteristics of Aero-Assisted Orbital	
Transfer Vehicles OAST (506-51-13)	44
Diurnal Cloud Variations	44
OSSA (672-22-04) Earth Surface Radiation Studies	45
OSSA (672-40-06)	
Landsat-Derived Cloud Populations	45
Analysis Method for Fourier Transform Spectroscopy	46
AD (307-03-02)	
Satellite and Lidar Measurements of El Chichon Stratospheric Cloud	47
OSSA (672-21-15)	
Satellite Observations of Stratospheric NO ₂ by SAGE	47
Stratospheric Aerosol Climatology in Polar Regions as	40
Observed by SAM II	48
Remote and In Situ Aerosol Measurements Over the Atlantic	48
Global Distributions of Cirrus Clouds Determined From SAGE Data	49
Airborne Lidar Observations of Long-Range Transport in the Free	
OSSA (176-40-04)	50
Sulfur Budget of the Troposphere	50
OSSA (176-20-02) Sources of NO _x to the Global Troposphere	51
OSSA (176-20-02)	. 1
Development of Interactive Aeroheating-Thermostructural	
Analysis Capability for AVID)2

Hemispheric Differences in Ozone May Be a Result of	50
Large-Scale Pollution	52
Effects of Transport and Photochemistry on Stratospheric NO ₂	53
OSSA (147-31-05)	53
Modeling Seasonal Cycles of Tropospheric Trace Gases	54
SAGE Observations of Cirrus Clouds in Lower Tropical Stratosphere	55
Airborne Measurements of Shuttle Exhaust Constituents	55
Stability of the Surface Layer and Its Relation to Dispersion	
of Primary Pollutants in St. Louis	56
Structures Directorate	
Structures Directorate	
Lightly Crosslinked High-Temperature Structural Resins	57
Advanced Powder Metallurgy Aluminum Alloys Develop High Strength-Toughness Combinations	58
Metal-Ion-Containing Epoxies	58
A Fracture Mechanics Approach to Impact Delamination Damage	59
Damage Tolerance of Stringer-Stiffened Composite Panels	60
Improved Structural Efficiency Offered by SPF/WB and Selective	
Reinforcement	
Improved Tension-Stabilized Cable Materials	
Sealed and Doped Coatings Reduce Mass Loss of Carbon-Carbon Materials	
Guyed Space Boom Nonlinear Dynamic Response Predicted	
Damage Containment Concept Tested for Composite Compression Panels	
Impact Damping Substantially Reduces Slender-Strut Vibrations	
Limits of Achievable Accuracy Defined for Truss Antenna	
Tendon-Controlled Boom Concept	65
Stitching Improves Strength of Composite Joints	
Friction and Wear Behavior of Composite and Aluminum Airplane Skins	66

Higher Harmonic Control System Effective in Reducing Helicopter Vibrations	67
Transonic Pressure Distributions Measured on a Rectangular Supercritical Wing Oscillating in Pitch OAST (505-33-43)	67
Hingeless-Rotor Experiments Validate Analytical Method	68
Transonic Flutter Studies of Effects of Winglets Extended to Twin-Engine Transport Type Wing OAST (505-33-43)	68
Mass Addition Film Cooling Tests at Mach 6.8	69
Noncatalytic Coating for Metallic TPS Reduces Heating	69
Analytical Technique Demonstrates Control of Space Structure Thermal Distortion by Applied Heating	70
Airfoil Self-Noise: Effect of Scale	70
Shock Noise Associated With Supersonic Jet Plumes	71
Shear Layer Instability Related to Screech Generation	72
Boundary Layer Effect on Propfan Noise	72
Comparison of Pusher and Tractor Propeller Noise	73
Analytical Prediction of Aircraft Interior Noise	
Reduction of Structureborne Noise	
Noise Transmission Loss of Advanced Composite Panels	74
Evaluation of Ride Quality Prediction Methods for Operational Military Helicopters OAST (505-35-13)	75
Projects Directorate	
Projects Directorate	76
Advanced Composite Structures Technology	76
Laminar-Flow-Control Technology	76
New Thermal Design/Integration Concept	77
Technology Integration for Subsonic Transport Aircraft	77
Application of Emerging Technologies to Supersonic Fighter Concept	78

Systems Engineering and Operations Directorate

Systems Engineering and Operations Directorate	79
Five-Axis Adjusting Mechanism	79
Radio-Controlled Positive Propulsion System for Tunnel Model Spin Recovery	
Low-Temperature Cryoseals	80
Structural Verification Test and Dynamic Analysis for LDEF	
Improved GN ₂ Flow Blocker for NTF Fan Shaft	81
Grain Refining Heat Treatments To Improve Cryogenic	
Toughness of High-Strength Steels	
Solid-Particle Seeding for Laser Velocimeters	82
Technology Utilization Office	
Technology Utilization Office	
Ultrasonic Temperature Monitor for Hyperthermia	
Lightweight Composite Wheelchair	83
Vehicle Ride Quality Meter	84

Aeronautics Directorate

The Aeronautics Directorate at NASA Langley is composed of approximately 300 scientists and engineers engaged in research in the various aeronautics disciplines. The Directorate is organized into three research divisions, which conduct aeronautical research to advance the state of the art throughout the complete aerodynamic speed range.

The Low-Speed Aerodynamics Division conducts research in the areas of basic fluid mechanics, low-speed aerodynamics, flight dynamics, and flight management, aircraft operations, aviation safety, and improved test methods. The Division develops and validates theoretical aerodynamic methods for subsonic conditions and design methodology required to improve subsonic aerodynamic performance, stall/spin behavior, handling qualities, and takeoff

and landing performance.

The High-Speed Aerodynamics Division conducts research to advance the state of the art for supersonic aircraft, hypersonic aircraft, and missiles, and to support the development of high-performance military aircraft, advanced cruise and tactical missiles, the Space Shuttle, and follow-on advanced space transportation systems. New analytical methods for design and analysis are derived and applied to advanced high-speed aircraft and missile concepts. Key experiments are conducted to validate the analytical methods, explore the potential of advanced concepts, and provide a data base for use by industry design teams. Conceptual designs for advanced highspeed vehicles are conceived and analyzed in order to determine the performance payoff from the application of advanced research results.

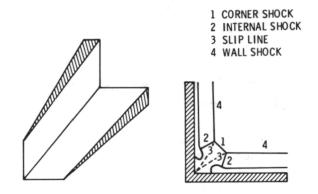
The Transonic Aerodynamics Division conducts research to advance the state of the art of transonic aircraft technology in the areas of fundamental aerodynamics, with particular emphasis on Reynolds number effects, laminar-flow concepts, stability and control, performance analysis, configuration concepts, and related aerodynamic phenomena. Particular areas of emphasis include improving the efficiency and reducing the fuel consumption of conventional jet transports, developing the technology for advanced military combat aircraft, developing theoretical and analytical methods for predicting aerodynamic characteristics in separated and in transonic flows, developing advanced airfoils for low-speed and transonic aircraft and for helicopters, and developing advanced experimental techniques, including advanced wall concepts, for transonic wind tunnels, cryogenic wind tunnel technology, and magnetic suspension and balance systems. Research analysis is performed using advanced analytical techniques with

Langley's large computer complex. These research results are obtained from tests conducted in Langley's unique experimental facilities, which span the range from subsonic through transonic (including the new National Transonic Facility) to supersonic.

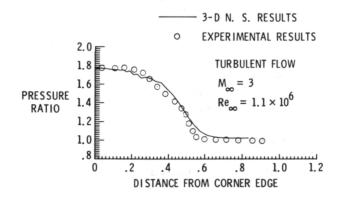
Three-Dimensional Navier-Stokes Code for Scramjet Inlet Flow Field

A computer code has been developed to analyze the viscous flow in supersonic-combustion ramjet (scramjet) inlets. This code uses the three-dimensional Navier-Stokes (N.S.) equations in conservation form to describe the inlet flow. The equations in the physical domain are transformed to a regular computational domain by using an algebraic numerical coordinate transformation that generates a set of boundary-fitted curvilinear coordinates. The transformed equations are solved by the well-known unsplit, explicit method of MacCormack. In the case of turbulent flow calculations, an algebraic two-layer eddy viscosity model is used.

To assess the computer code, calculations were made for turbulent flow in a three-dimensional 9.48°



Symmetric wedge corner and schematic of corner flow.



Comparison of sidewall pressure distribution.

symmetric wedge corner for which detailed experimental results were available. The flow in such a corner is representative of the type of flow inside a scramjet inlet. The basic characteristics of the corner flow are shown here schematically. The flow has a very complex structure that includes wall shocks, corner shock, internal shocks, and slip lines. To predict such a complex flow field, it is necessary to properly discretize the corner geometry. In the present calculations, a grid of $39 \times 61 \times 61$ points was used, with suitable grid refinement near the corner walls. Flow was calculated at a free-stream Mach number of 3.0 and a Reynolds number of 1.1×10^6 .

A comparison between computer-generated sidewall pressure distribution and the experiment is shown. It can be seen that the computed results are in excellent agreement with the experimental results.

The code is written for the Control Data CYBER 203 vector-processing computer and uses 32-bit word arithmetic. The maximum grid size that can be computed without going out of primary memory of the computer is approximately 150,000 points. The compute rate is approximately 1.4×10^{-5} sec/grid point/time-step for the viscous flow. Since its development, the code has been used successfully to calculate viscous flow in a variety of scramjet inlet configurations.

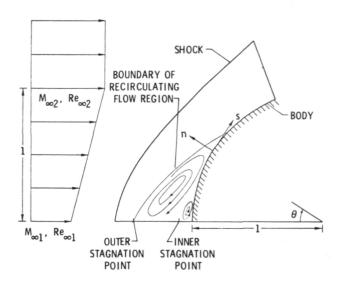
Ajay Kumar, 3171

Supersonic Shear Flow Past a Circular Cylinder

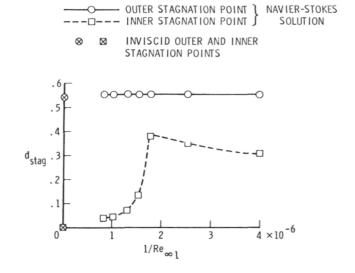
Several recent numerical studies have been able to predict separation phenomena over smooth surfaces with the Euler equations. This inviscid separation occurs in rotational flows as a result of the premature retardation of the surface velocity caused by vorticity in the flow. An example of one such flow is the supersonic shear flow past a circular cylinder. The Euler solution for this flow exhibits a large region of recirculating flow ahead of the front stagnation point. The emphasis of the present study is to investigate the structure of the recirculating region for inviscid as well as viscous flow. An attempt is made to find out whether the Navier-Stokes (N.S.) solution of the problem in any way approaches the Euler solution as the Reynolds number is increased.

The basic structure of the supersonic shear flow as calculated by the N.S. equations is shown here schematically. A large recirculating flow region is formed around the front stagnation point with relatively low energy. Inside the recirculating region, there are two counter rotating vortices that give rise

to two additional stagnation points along the symmetry line other than the stagnation point on the body. This is in contrast to the structure of the inviscid recirculating region, where only one vortex is found to exist and only one additional stagnation point occurs along the symmetry line. The inner vortex in the N.S. solution is formed because of the viscous effects, and its size is found to be dependent on the Reynolds number. A plot is shown of the distances of inner and outer stagnation points from the body surface relative to the reciprocal of free-stream Reynolds number, $Re_{\infty 1}$. For each calculation, the



Schematic of viscous supersonic sheer flow past a circular cylinder.



Variation of outer and inner stagnation point distances with Reynolds number.

free-stream shear is kept constant at Mach numbers between 10 and 18. Inviscid values obtained from a solution of the Euler equations are also marked by the symbol x on the vertical axis, corresponding to infinity Reynolds number. It is seen that the distance of the outer stagnation point remains practically constant at all the Reynolds numbers, and its value is about the same as for the inviscid flow. The distance of the inner stagnation point also does not change significantly up to about $Re_{\infty 1} = 0.5 \times 10^6$, but with further increase in Reynolds number, the distance drops rather quickly; in fact, it appears as if it will approach zero asymptotically at very high Reynolds numbers.

Ajay Kumar, 3171

Cartesian Finite-Volume Transonic Potential Method

The solution of the transonic full-potential equation (FPE) about complex configurations (e.g., a fighter with stores) is limited presently by the generation of a suitable body-conforming grid. On the other hand, the transonic small-disturbance equation (TSDE) is now solved routinely for complex configurations. The reason for the success of the TSDE is the simplicity of the boundary condition formulation, the use of nearly Cartesian grids, and grid embedding. With these considerations, a method is under development to combine the grid simplicity of the TSDE codes with the improved accuracy of FPE.

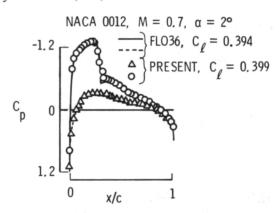
In this method, the FPE is solved in a Cartesian coordinate system using a finite-volume formulation. In a typical two-dimensional rectangular cell, the flux balance is written as

$$(\rho \phi_{\rm X} A)_{\rm E^-} (\rho \phi_{\rm X} A)_{\rm W} + (\rho \phi_{\rm V} A)_{\rm N^{-1}} (\rho \phi_{\rm V} A)_{\rm S} = 0$$

where the density ρ and the potential ϕ are stored at cell centers, A is the area of a cell face, and the cell faces are labeled as points of the compass (N, E, S, W). The subscripts x and y denote differentiation of ϕ to yield the Cartesian velocity components at the cell faces using central differences between adjacent cell centers. Where a solid boundary surface cuts through a cell, the cell face areas A in the equation are simply reduced by the amount that extends inside the surface; this procedure yields the proper flux balance for boundary-intersecting cells.

The computational accuracy and versatility of the method have proved to be extremely good. The figure shows a comparison of results for a lifting transonic airfoil (NACA 0012 section) obtained by the present method and by FLO36, a potential code using a body-fitted grid generated by conformal mapping. The free-stream Mach number M is 0.7, and the angle of attack α is 2°. Shown in the figure are plots of the pressure coefficient C_p along the upper and lower surface of the airfoil. The jump in C_p on the upper surface is a shock wave. The lift coefficient Co is also shown in the key for both methods, and they agree within 1 percent. Similar good agreement has been obtained between the present method and other body-fitted methods for a variety of flows, including axisymmetric missile shapes with concave and convex corners in the body contour and airfoils in wind tunnel channels. Current research is directed to extending the method to threedimensional configurations. This project is a cooperative effort between Northrop Corporation and NASA Langley.

Jerry C. South, Jr., 2627



Comparison of transonic lifting airfoil pressure distributions obtained by Cartesian finite-volume method and method using body-fitted grid.

Improved Efficiency in Solutions of Inviscid Transonic Rotational Flow

In a joint effort between Princeton University, NASA Langley, and the Institute for Computer Applications in Science and Engineering (ICASE) at Langley, large improvements in efficiency have been obtained in solving the Euler equations (the equations that describe inviscid, rotational flow) for steady transonic flow with shock waves. The latest method combines a finite-volume scheme for the spatial approximation to the inviscid laws of conservation of mass, momentum, and energy; a Runge-Kutta time-stepping scheme for integrating the time-dependent equations toward a steady state; a "residual smooth-

ing" stage that allows a large time step without causing instability; and a multigrid convergence acceleration method that uses a sequence of coarser grids to successively reduce the low-frequency components in the convergence error, or residual.

As recently as 1981, several existing methods using "standard" procedures for solving the Euler equations required 10,000 to 20,000 time steps to reach a steady-state solution. By 1982, the present effort had reduced the number of required steps to about 1.000. The latest method, embodied in a code called FLO52MG, achieves transonic solutions in the equivalent of about 50 steps on a Control Data CYBER 203 computer in 40 seconds without utilizing the vector-processing capability of the 203. The use of vector instructions and 32-bit arithmetic in the code should reduce solution times to 5 seconds. Similar technology is being developed for a three-dimensional version of the method now being used in industry. The current version, without the residual smoothing and multigrid acceleration, obtains solutions for a transonic wing with 40,000 mesh points in about 7 minutes on a CRAY-1 and 3.6 minutes on a 203 (using vector instructions and 32-bit arithmetic). Solution times of less than 5 minutes should be obtainable for "serious" three-dimensional cases with finer meshes (500,000 points) using the new mathematical methods coupled with vector-coding instructions and 32-bit arithmetic.

Jerry C. South, Jr., 2627

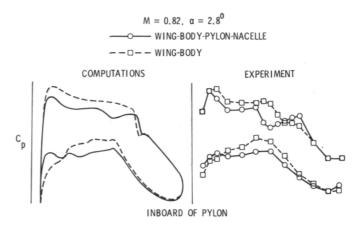
Validation of a Three-Dimensional Transonic Wing-Body-Pod-Pylon-Winglet Computer Code

A computer code for aerodynamic analysis of complete aircraft configurations at transonic flight speeds has been developed by the Grumman Aerospace Corporation under contract to NASA Langley. The code has the capability to analyze a wing-body-pod-pylon-winglet (WBPPW) configuration. It incorporates the transonic small-disturbance potential approximation and nearly Cartesian grids with embedded fine grids in regions where flow gradients are expected to be large. Viscous effects can be included in the wing solution.

To provide confidence in the use of the code by the aircraft design community, an extensive effort has been undertaken to validate the pylon-nacelle capability of the WBPPW code by comparing computed results with experimental data. The data were obtained during experimental research conducted in support of the Energy Efficient Transport effort at

Langley. The subject configuration is an advanced transport developed at Langley. Computed results were obtained on the baseline wing-body configuration with and without engine nacelles. Two engine nacelles, Energy Efficient Engine (E3) mixed flow and long-core separate flow (LCSF), were analyzed at various positions and orientations beneath the wing. These computed results were compared with experimental data. Typical results showing the comparison of computed and experimental data are presented in the figure. These comparisons show the variation in wing pressure distributions resulting from adding the E³ engine nacelle to the baseline wing-body configuration. Trends and magnitudes of the effects observed in the experimental data are accurately predicted in the computations. Results of the study indicate that the WBPPW code can accurately predict differences in wing pressure distributions resulting from the addition of a pylon-nacelle to a wing-body configuration. In addition, variations in wing pressure distributions resulting from nacelle translation and vaw orientation were accurately predicted using the code. Overall, the results were encouraging for using the code to complement wind tunnel testing in a design environment.

E. G. Waggoner, 2627



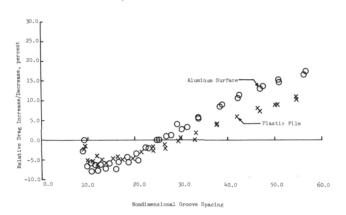
Comparison of computed and experimental data.

Turbulent Drag Reduction Using Longitudinal Surface Grooves

Experiments at NASA Langley over the past 5 years have demonstrated that various riblets or small longitudinal (flow-aligned) surface grooves machined into flat surfaces can produce reductions in net turbulent drag of up to 10 percent compared to ungrooved smooth surfaces. These longitudinal grooves typically have heights and spacings on the

order of 0.020 in. or less. Recently, practical light-weight riblet surfaces (i.e., extruded plastic films with adhesive backing) have been tested in the 15-in. low-turbulence wind tunnel at Langley. Net drag measurements with these grooved plastic films indicate turbulent drag reductions as good as or better than those obtained for machined aluminum surfaces having the same groove geometries. This vinyl material promises to be an economical and efficient way of mass producing and applying riblet surfaces to candidate aircraft surfaces.

Michael J. Walsh, 4546



Comparison of grooved aluminum and plastic surfaces.

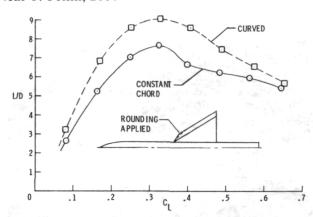
Vortex Flap Shaping

Vortex flaps are deflectable surfaces attached to the leading edges of highly swept wings to exploit the naturally occurring leading-edge vortices present on these wings. When properly designed, the leading-edge vortex will form along the forward-facing deflection surface and promote smooth transition to attached flow onto the wing upper surface. The vortex induces strong suction pressures on the forward-facing flap surface, thereby generating a large lift increase as well as an axial thrust force component which is useful for drag reduction.

Experimental parametric studies conducted at subsonic speeds have demonstrated that planform shaping of the vortex flap is important for improving aerodynamic performance. As shown in the figure, for a 58° delta wing, a small amount of planform rounding applied to the apex region (indicated by a dashed line) resulted in increases in lift-to-drag ratio of 1.5 to 2 over a large lift range. A maximum performance improvement of 26 percent is noted at a lift coefficient of 0.4.

This increase in performance is particularly important for aircraft that are climbing or executing sustained transonic maneuvers. The lower drag at a constant lift means that smaller, lighter engines are required for the same design lift condition. This technology will allow future tactical aircraft to have both sustained supersonic cruise and transonic maneuver capability.

Neal T. Frink, 2601



Performance improvement through vortex flap shaping.

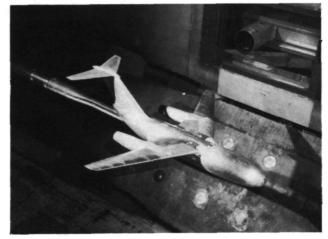
An Investigation of Aft-Mounted Nacelles on a Supercritical Wing

The installation of engine nacelles on the wing, the fuselage, or the tail of an aircraft has a decided effect on the aerodynamic performance of the aircraft. As part of the overall propulsion-airframe integration program, a wind tunnel test has recently been conducted with long-duct flow-through nacelles mounted at an extreme aft chord position beneath the wing of a typical twin-engine transonic transport configuration, as shown in the figure. Nacelles having circular and D-shaped inlets located at 75 percent of the local chord were tested at the 0.37 semispan station over a Mach number range from 0.70 to 0.85.

Test results indicate that the form interference drag of the aft-mounted D-nacelle configuration is approximately one-third that of a comparable pylon-mounted nacelle located beneath the wing. This results in a total installed drag reduction of approximately 35 percent. The drag of the circular nacelle is slightly higher; this may be due to drag from the flow diverter required between the wing lower surface and the nacelle.

The favorable effect obtained with the aftmounted nacelles is due to a large deceleration of the flow beneath the wing. The introduction of the flow field of the D-nacelle below the wing acts similar to a flap, causing an increase in the pressure coefficients on the wing lower surface and an increase in lift relative to the wing alone. This lift increase is approximately equal to the usual lift loss associated with the installation of the pylon-mounted nacelle. It should also be noted that the usual shock formation, with its resulting wave drag on the wing lower surface associated with the pylon-mounted nacelle, is not present.

James C. Patterson, 2675



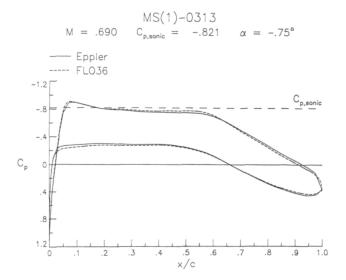
Aft-mounted nacelles on a supercritical wing.

Compressibility Correction for Eppler Airfoil Program

An advanced compressibility correction has recently been incorporated into the Eppler Airfoil Design and Analysis Program. The correction, developed by Labrujére of NRL (The Netherlands national aerospace laboratory) accounts for the effect of Mach number on pressure distributions. Extensive comparisons with the latest full-potential equation solution by Jameson of Princeton University (FLO36) and the subcritical method of Jäger of the University of Stuttgart show excellent agreement even for cases with locally supersonic flow. This correction is, of course, applicable only to shock-free flows. A typical comparison is shown in the figure. Additional comparisons with the classic Kármán-Tsien correction show the Labrujére correction to be significantly superior.

The incorporation and evaluation of this correction were performed by Richard Eppler and Helmut Jäger of the University of Stuttgart in cooperation with NASA Langley.

Dan M. Somers, 4514



Comparison of methods for calculation of pressure distribution.

CAST 10-2 Airfoil Studies With Sidewall Boundary Layer Removal

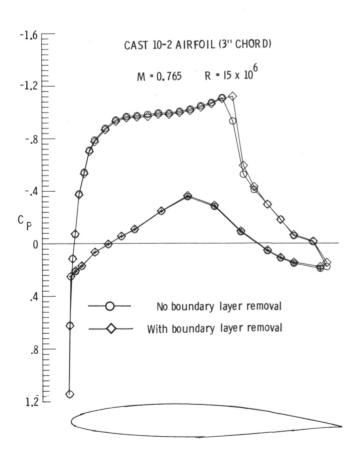
A sophisticated sidewall boundary layer removal system has been incorporated to the 0.3-Meter Transonic Cryogenic Tunnel (TCT) to minimize the influence of the sidewall boundary layer on the airfoil test data. Recently, tests were conducted using this boundary layer removal system on two DFVLR CAST 10-2 airfoil models. The purpose of this investigation was to evaluate the extent to which the test data on the airfoils was influenced by the sidewall boundary layer and also to validate the method and technique of sidewall boundary layer removal. The experimental apparatus used in this investigation included a pair of perforated panels fixed to the tunnel test section sidewalls upstream of the model location. These perforated panels, developed using the electron beam technique, had a nominal porosity of about 10 percent with a hole diameter of 0.27 mm and a spacing of 0.75 mm. The quantity of boundary layer mass flow removed from either of the sidewalls through the perforated panels was controlled precisely by two separate flow control digital valves.

In the first phase of the tests, the test section was calibrated to determine the correction for test Mach number due to mass removal and also to determine the extent of the boundary layer thinning obtainable in the airfoil region. With the present boundary layer removal system operating in the passive mode, the maximum mass flow removal rate was equal to the liquid nitrogen injected into the tunnel to maintain steady operating conditions. The maximum boundary

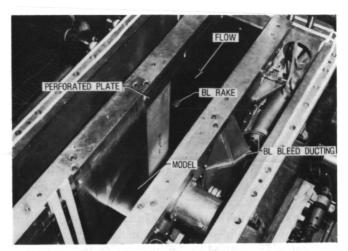
layer removal at transonic speeds was equal to about 2 percent of the test section mass flow, and at this condition, the boundary layer thickness in the region of model location was about 1 percent of the test section width.

In the second phase of the tests, pressure measurements were made on two different chord models (3 in. and 6 in.) of the CAST 10-2 airfoil employing sidewall boundary layer removal. These advancedtechnology airfoil models developed and fabricated at the DFVLR, West Germany, had a thickness-tochord ratio of 12.1 percent. The test conditions covered a Mach number range from 0.6 to 0.8 at chord Reynolds numbers 6, 10, 15, and 30 million. The test results in the figure show that the perforated panels used for boundary layer removal did not cause any major changes on the airfoil aerodynamics when there was no boundary layer removal. It was also observed that when the sidewall boundary layer was removed, the shock position on the upper surface moved downstream initially and appeared to have a reversal in direction of movement at higher lift.

Charles B. Johnson, 4380



Effect of boundary layer removal on airfoil pressure distribution.



Installation of perforated plates on 0.3-m TCT sidewalls for boundary layer removal.

Development of Wind Tunnel Wall Interference Assessment/Correction (WIAC) Methods for Three-Dimensional Transonic Flows

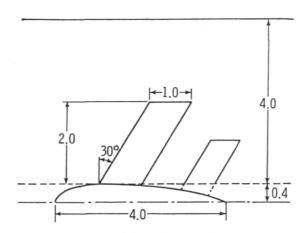
NASA Langley expanded its research effort related to transonic wind tunnel wall interference to support the National Transonic Facility (NTF) technology, which included a conventional slotted-wall test section. For transonic flow conditions in ventilated-wall tunnels, the classical linear-theory wall interference predictions were known to be unsatisfactory. Using concepts and capabilities from both adaptive-wall and computational transonic (CFD) technologies, post-test assessment/correction procedures were formulated which circumvent many short-comings of the classical theory. The major software item in a correction procedure for a given facility is the WIAC code.

As part of this effort, the Flow Research Company (under contract to NASA) has developed and delivered three 3-D WIAC codes that are now being validated and incorporated into correction procedures for the NTF. All of these codes use measured tunnel wall data in the outer boundary conditions and approximate the model based on its hard geometry and measured force data. They differ primarily in the assumed governing flow equation and solution technique. The code LINCOR solves a linear Prandtl-Glauert equation for the interference flow field appropriate to a wing-body-tail model in a rectangular-cross-section tunnel. The code TUNCOR solves the nonlinear 3-D transonic small disturbance equation (TSDE) for equivalent inviscid tunnel and freeair flows for the same model-tunnel geometries. The

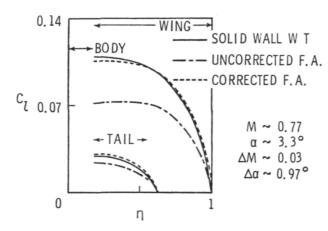
code SLENCOR uses slender lifting-body equivalence rule concepts in solving the nonlinear 3-D TSDE for equivalent tunnel and free-air flows; it is appropriate to slender 3-D configurations at small incidence in near-sonic flows.

Wall interference corrections of computer-simulated wind tunnel flows have been made with all three WIAC codes. Typical results from TUNCOR for a wing-body-tail configuration in a solid-wall tunnel are shown in the figure. Both wing and tail have NACA 0012 airfoil sections, and the model is located on the tunnel axis with dimensions as shown. The spanwise lift distributions on both wing and tail for the simulated solid-wall wind tunnel (WT), uncorrected free air (FA) at M and α , and corrected free air at M + Δ M and α + $\Delta\alpha$ are shown in the plot of spanwise lift distributions. The corrected free-air results are seen to compare very favorably with the simulated tunnel data, thus lending confidence to the WIAC procedure.

Perry A. Newman, 2627



Wing-body-tail in solid-wall tunnel.

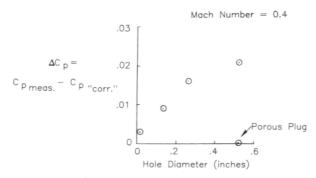


Wall interference corrections to Mach number and angle of attack from WIAC code TUNCOR, shown for spanwise lift distributions.

Orifice-Induced Pressure Error at High Reynolds Number

For some time it has been known that a hole drilled perpendicular to a stream surface for the purpose of measuring static pressure will disturb the local flow and induce an error in the measured pressure. For conventional wind tunnels, the boundary layer over a model's surface is much larger than the size of the orifice used to measure static pressure. Previous studies have indicated that for such cases. the induced error is negligible. However, with the advent of facilities such as the National Transonic Facility (NTF) and the 0.3-Meter Transonic Cryogenic Tunnel (TCT), which can attain flight Reynolds numbers, the boundary layer thickness could be an order of magnitude thinner than those in a conventional wind tunnel. The orifice diameter would then be much larger with respect to the boundary layer thickness, and it is expected that the orifice would have more of an effect on the boundary layer and cause a larger error, possibly one which could not be neglected.

To study this problem in a conventional wind tunnel, it was necessary to use static pressure orifices with larger hole diameters to enable modeling of the larger ratios of orifice diameter to boundary-layer displacement thickness which are obtainable in high Reynolds number flow. The inner diameters of the static pressure orifices to be tested ranged from 0.020 in. (the size commonly considered to give "correct" measurements in a conventional wind tunnel) to 0.520 in. A modification was made to the 0.520-in. orifice to enable a circular plug of porous metal to be pressed into the orifice flush with the upper surface. The various sizes of orifices were mounted on a flatplate model and tested in the Langley 7- by 10-Foot High-Speed Tunnel (HST). From the data shown in the figure, it can be seen that as the orifice hole diameter increases, the pressure error ΔC_p increases, and, in fact, can no longer be considered negligible. Notice that the orifice with the porous metal plug, which was constructed from the 0.520-in. orifice,



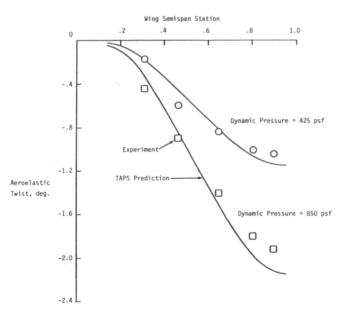
Effect of orifice size on pressure error.

appears to eliminate the pressure error. Though studies still need to be conducted on many aspects of porous-plug technology, the porous-plug orifices appear to be a viable means of reducing orifice-induced pressure error and providing more accurate pressure measurements.

E. B. Plentovich, 2601

Wing Deflections and Pressures in Transonic Flow

In order to accurately predict the effect of changing Revnolds number and dynamic pressure on a wind tunnel model at transonic speeds, it is necessary to include wing deflections as well as viscous effects in the aerodynamic calculations. An analytical method known as TAPS (Transonic Aeroelastic Program System) has been developed at NASA Langley which includes these effects when computing wing pressures and deflections. The system is set up to iterate between an aerodynamic and a structural analysis code until converged results from both codes are obtained. The current version of TAPS utilizes the WIBCO wing-body transonic potential flow code (with boundary layer) developed by Boppe (at Grumman Aerospace Corp.) and the SPAR finite-element structural code developed by Whetstone (at Engineering Information Systems, Inc.). Using the structural analysis code eliminates the need to experimentally determine the structural response characteristics of the wing to static loadings. An added benefit is that wing camber as well as twist



Spanwise twist distributions for TF-8A model.

changes due to aerodynamic loading can easily be determined and included in the aerodynamic calculations.

The figure shows the spanwise distribution of aeroelastic twist calculated for the TF-8A airplane model using TAPS. Included for comparison are data acquired in the Langley 8-Foot Transonic Pressure Tunnel using a stereophotogrammetry system. The TAPS predictions correlated very well with the measured data for this case at a Mach number of 0.95. A substantial increase in wing twist resulting from an increase in dynamic pressure was both predicted and measured. This illustrates the importance of accounting for model deformation in tunnels such as the National Transonic Facility which operate over a broad range of pressure.

Richard Campbell, 2601

Free-Flight Tests of Three-Surface Fighter Configuration

The three-surface (canard, wing, and tail) arrangement applied to combat aircraft offers potential performance advantages and is therefore being considered for future fighter designs. To explore the high-angle-of-attack flight characteristics of this concept, a broad research program has been conducted involving wind tunnel tests, dynamic model tests, and simulation. As part of this program, free-flight tests of a 0.18-scale model of a three-surface fighter design based on the F-18 were recently conducted in the Langley 30- by 60-Foot Tunnel. The primary purposes of the tests were to study stability and control characteristics up to the stall and to make an initial assessment of control system requirements for high-angle-of-attack flight.

In the tests, the model was flown unconstrained in the test section of the tunnel. The model was controlled remotely by pilots situated at appropriate positions around the test section. Inputs from the pilots and motion sensor signals from the model were fed into a digital computer that generated commands to drive the control surfaces on the model.

In the free-flight tests, the configuration exhibited good characteristics up to the angle of attack for wing stall ($\alpha \approx 20^{\circ}$). At higher angles of attack, the model was susceptible to large-amplitude undamped roll oscillations caused by loss of roll damping. A roll-damping augmentation system was developed which eliminated this problem and allowed the model to be flown up to the angle of attack at which maximum lift is developed ($\alpha = 35^{\circ}$). The test results

also showed that the high-angle-of-attack characteristics of the configuration are strongly influenced by the canard because of the strong coupling between the canard-wing-empennage flow fields.

Mark A. Croom, 2184



Three-surface fighter model in free-flight tests.

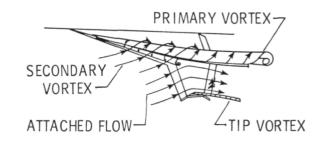
Subsonic Investigation of Cranked Wings Suitable for High-Maneuver Supersonic Fighters

Cranked wings may have major advantages for supersonic fighter aircraft that must have good subsonic and transonic maneuver capability. The cranked wing can provide good supersonic efficiency, and more importantly can provide sufficient aspect ratio which, if combined with efficient aerodynamic wing flow, could provide an effective subsonic/transonic-maneuver wing design. A cranked wing is typically divided into two major areas: a highly swept inboard section, and an outboard section of a lesser sweep. Conceptually, the possibility arises of designing each panel of the wing (inboard and outboard) to use either attached or leading-edge vortex flow to provide efficient lift.

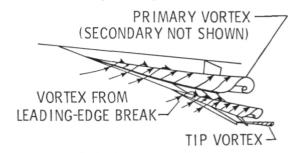
Two such possibilities are shown in the figure. A low-sweep outboard panel is shown which develops efficient attached flow through leading- and trailing-edge flap deflections. The highly swept inboard section would develop vortex flow over a leading-edge flap. The other wing has a more highly swept outboard panel, which is postulated to produce a leading-edge vortex system similar to that of the inboard section. Both concepts would depend on scheduling leading- and trailing-edge flap deflections for optimum drag due to lift at maneuver conditions.

To investigate the possibilities of these crankedwing concepts, an initial low-speed investigation of a series of wings of this type has been completed in the Langley 12-Foot Low-Speed Tunnel. Flow visualization techniques and force measurements were used in order to understand the type of flow structure developed over the various wing surfaces. Results from these tests showed that a mixed-flow condition (vortex flow on the highly swept inboard section and attached flow on the cranked outboard section) is possible for wings with low-sweep (20°) outboard cranked sections. Intermediate outboard sweeps (46°) show difficulties in obtaining either attached flow or vortex flows on the outer panel due to large spanwise flow from a large inboard panel vortex. Further sweeping of the outboard panel to 60° results in a leading-edge vortex system for both inboard and outboard panels. Both the low-sweep and the highsweep outer-panel designs thus show promise as viable solutions for supersonic wings at subsonic maneuvering conditions.

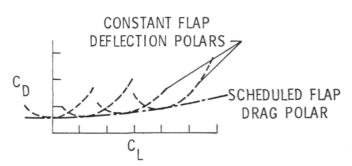
Kam W. Hom, 3294



Postulated low tip sweep flow.



Postulated high tip sweep flow.



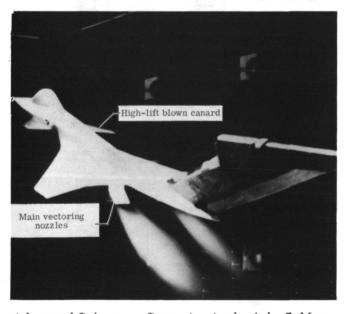
Flap-scheduling concept.

Trimming Advanced STOL Fighter Configurations

A wind tunnel investigation was conducted by NASA in conjunction with the Air Force Wright Aeronautical Laboratory and Grumman Aerospace Corporation to determine the trim capability of a blown high-lift canard for an advanced STOL fighter configuration with vectoring main nozzles. The use of vectoring nozzles to provide the proper lift and drag required for STOL operations is typically limited because the reduced control power available at low speed from canards or horizontal tails cannot trim the nose-down pitching moments produced by the vectored thrust. In order to increase the control power and thereby improve the trim capability of the canard on an advanced fighter configuration, a blown trailing-edge flap and leading-edge Krueger flap were installed on the canard. For this design, only a small amount of blowing is used to provide boundary layer control on the canard full-span trailing-edge flap to maintain attached flow.

The results of the investigation indicate that the configuration (which is untrimmable with a conventional canard) can be trimmed across the angle-of-attack range tested with the main nozzles vectored 40° and thrust levels set at military power. This trimmed condition is maintained at a lift coefficient greater than 1.5 at 14° angle of attack (typical of approach conditions) and drag appropriate to allow a STOL approach.

J. W. Paulson, Jr., 3611



Advanced fighter configuration in the 4- by 7-Meter Tunnel.

Numerical Simulation of Shuttle Solid-Rocket Booster Ignition Transients

The first Shuttle launch produced overpressure waves resulting from ignition of the solid-rocket boosters that were significantly larger than expected. Extensive ground testing and analysis provided an engineering correction for this potential problem which has worked successfully on all subsequent launches. However, considerable interest was generated to better understand the fluid dynamics associated with such ignition overpressure phenomena. As a result of this interest, a numerical simulation effort was undertaken jointly by NASA Langley and the Los Alamos National Laboratory. This effort involved the use of an existing computer program developed for treating time-dependent, two-dimensional, compressible turbulent flow in and about relatively general nozzle-afterbody configurations. The program was developed under partial Langley sponsorship by M.C. Cline of Los Alamos.

One of the test cases selected for this effort was an isolated solid-rocket booster that had been fired statically and for which experimental data were obtained. Mach number contours at selected time intervals after ignition of the booster resulting from a fully viscous calculation, together with computergenerated color movies simulation, indicated that a significant overpressure wave was associated with the flow separating from the nozzle wall shortly after ignition and then expanding rapidly in a radial direction as the flow completely filled the nozzle. The predicted pressure transients were in good qualitative agreement with available data. The significant conclusion resulting from this calculation is that viscous effects can be extremely important in ignition overpressure predictions. This conclusion is confirmed by comparisons with an inviscid calculation for this same case.

Richard G. Wilmoth, 2675

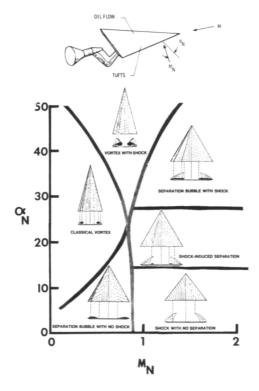
Leading-Edge Flows at Supersonic Speeds

Investigations at subsonic and transonic speeds of the vortex behavior on the leeward surface of wings have led to the development of various vortex flap concepts for producing high levels of efficient lift on highly swept wings. To provide information on this subject at supersonic speeds, an experimental investigation of the upper-surface flow on a series of sharp leading-edge delta wings has been conducted.

Surface pressure data were obtained to determine the effects of Mach number, angle of attack, and leadingedge sweep angle on vortex strength and vortex location. Also, three types of flow visualization data (oil flow, tuft, and vapor screen) were obtained. The oil flow and tuft data give information only about wing surface conditions, but the vapor screen data give a clear picture of the various flow mechanisms occurring above the wing surface. Using mainly the vapor screen data, the upper-surface flows were classified into seven distinct types, depending on the flow conditions α_N and M_N normal to the leading edge of the wing. Six of the seven flow types are shown in the figure. The α_N - M_N space is divided into regions and the type of flow is indicated by the sketch placed in each region. The seventh type, shockless attached flow, was observed only at $\alpha_N = 0$ and is not shown in the figure.

It had been reported in the literature previously, with limited flow visualization data, that a single boundary existed near M_N = 1 dividing the flow into one region of attached flow (M_N > 1) and one region of separated flow (M_N < 1). This latest expanded classification provides considerably more information, and it should be beneficial in the development of theoretical prediction methods and in the application of leading-edge vortex flows to supersonic wing design problems.

David S. Miller, 3181

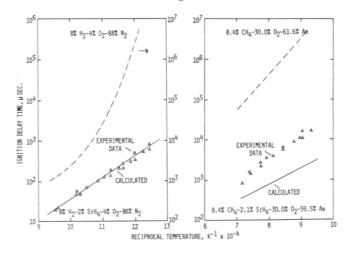


Classification of flow types.

Enhancement of Hydrogen and Hydrocarbon Combustion by Silane

Considerable attention is being given to the use of silane (SiH₄) as a combustion aid for both hydrogen-fueled and hydrocarbon-fueled supersoniccombustion ramjet engines. Experiments in the LaRC Hypersonic Propulsion Test Cells and at contractor test facilities have demonstrated that the addition of silane helps sustain stable combustion. In addition. recent shock tube studies have shown that adding silane to hydrogen-oxygen and methane-oxygen mixtures decreases ignition delay times substantially (see figure). To take full advantage of the effect of silane, a better understanding of the physics by which silane participates in the combustion process is needed. To help achieve this understanding, a chemical kinetic reaction scheme that describes the oxidation of silane was assembled. Since the silane molecule has a structure similar to that of the methane molecule, the silane oxidation scheme was assembled by analogy with the accepted methane oxidation scheme. The mechanism was refined by comparing the observed kinetic behavior in shock tube studies of silanehydrogen mixtures with that predicted by the mechanism. The results predicted by the model are shown in the figure. The model satisfactorily reproduced the experimental results for the silane-hydrogen mixture. However, predicted ignition delay times for the methane-silane mixture were lower than the experimental results. This suggests that some interaction between the silane and methane reaction products may be occurring. Reactions describing these interactions were not included in the reaction model.

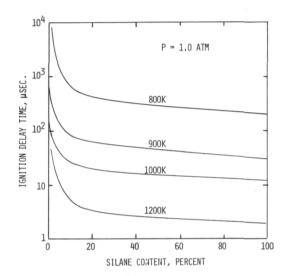
To acquire a better understanding of the effect of the relative quantity of silane on the ignition characteristics of hydrogen-air mixtures, a series of calculations were made for a range of fuel mixture ratios



Effect of silane on hydrogen and methane ignition.

ranging from pure hydrogen to pure silane. The results of some of these calculations are shown for overall stoichiometric mixtures at 1 atm pressure. The results illustrate the rapid sensitization of ignition which can be achieved by adding only small amounts of silane. These results suggest that only small amounts of silane (approximately 10 percent) may be needed to enhance and sustain combustion in hydrogenfueled scramjet combustors.

A. G. McLain, 2803



Effect of silane content on ignition delay times at various temperatures.

Hydrocarbon Combustion Model for Scramjet Applications

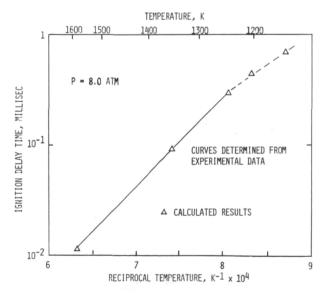
Increased interest in the possible use of a hydrocarbon-fueled scramjet as the propulsion unit for cruise missiles has led to the need for combustion models that can appropriately describe the combustion behavior of practical hydrocarbon-based fuels. It is anticipated that such combustion models will become valuable research tools in the study of hydrocarbon fuels in the same way that reaction models have been used to study and explain the combustion behavior of hydrogen at supersonic conditions.

A chemical kinetic reaction model has been developed at NASA Langley which describes the combusion behavior of a hydrocarbon fuel. The model is based on the oxidation characteristics of propane. It has been generally accepted that propane is the simplest hydrocarbon that has thermochemical and combustion properties which are similar in many ways to those of more complex practical hydrocarbon-

based fuels, including scramjet fuels. In the model, the propane is assumed to pyrolyze rapidly and react to form lower molecular weight products such as ethylene, methane, and propylene, followed by the oxidation of these products. The model consists of 83 elementary reactions among 27 chemical species. It was validated by comparing calculated results with experimental results on the ignition and oxidation of propane mixtures in shock tubes. A comparison of the calculated results with some experimental ignition results is shown in the figure. The calculated results are in very good agreement with the experimental results over the entire temperature range; this is true even at temperatures below 1250 K, where the increase in ignition delay time with decreasing temperature is not as large as the increase for temperatures between 1600 and 1250 K. The ability of the model to reproduce this and other experimental results suggests that it provides an acceptable description of the combustion properties of propane (and other hydrocarbons) at conditions relevant to supersonic application.

The combustion model has also been used to parametrically investigate the combustion behavior of hydrocarbon fuels at typical scramjet conditions. Preliminary results from these studies are in general agreement with experimental observation. Experiments have demonstrated that autoignition of hydrocarbon fuels at supersonic conditions is not feasible within reasonable combustor lengths. However, with an ignition source such as a pilot or flame stabilization zone, combustion can be achieved within reasonable combustor lengths.

C. J. Jachimowski, 2803



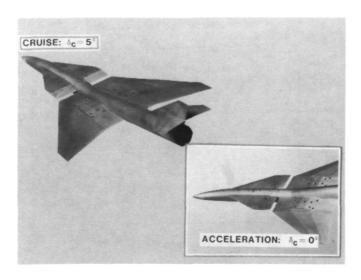
Comparison of calculated and experimental ignition delay times for stoichiometric propane-air.

High-Speed Aircraft Research

Wind tunnel tests have been completed in the Unitary Plan Wind Tunnel at speeds from Mach 1.5 to 4.63 on several configurations representing highspeed cruise aircraft concepts. These aircraft concepts were designed to operate at high altitudes and speeds up to Mach 5. High-speed acceleration and cruise require a large inlet to supply air to the engines. These large inlets impose a weight penalty on the configuration, increase airframe drag at transonic speeds, and complicate the geometric integration of the propulsion system and vehicle airframe. One of the configurations tested included a novel approach to inletairframe integration which utilized a close-coupled canard to precompress the airflow ahead of the engine inlets. Precompression is achieved by deflecting flaps (located on the trailing edge of the canard) down ahead of the inlets to accomplish some of the airflow compression that would normally be provided by the engine inlets. The net result is a smaller and lighter inlet system that has the additional advantage of eliminating the canard flap deflection at transonic speeds to reduce overall aircraft drag.

During the wind tunnel investigation, the performance of the precompression canard concept was compared with that of a similar configuration, but without the precompression canard feature. Results of the tests indicated that no aerodynamic penalties occurred at the high Mach numbers as a result of the precompression canard. In addition, drag was reduced at lower supersonic speeds by moving the canard flaps upward to deflect excess air over the top of the inlets.

John P. Weidner, 3294



Precompression canard concept.

Engine-Out Characteristics of Light Twin Aircraft

The failure of an engine is a major cause of fatal accidents on current light twin aircraft. As the first phase of a research program to address this problem, a piloted simulation study is being conducted on the Langley General Aviation Simulator. The primary objectives of the study are to provide further understanding of the basic flight dynamics and piloting problems associated with engine-out and to define automatic control concepts to improve safety under this condition.

The simulation aerodynamic model represents a generic twin and was developed using data from earlier tests conducted in the Langley 30- by 60-Foot Tunnel and from more recent qualitative flight tests of two NASA airplanes. The simulation cockpit is mounted on a three-degree-of-freedom motion base and incorporates an out-the-window visual scene generated by a terrain board system.

A preliminary research program to explore the effects of various performance and control characteristics on engine-out controllability and handling qualities has been completed. The results show that although the control deflections and forces required after an engine failure are large, the pilots were generally able to maintain control of the airplane.



Twin-engine simulation cockpit.

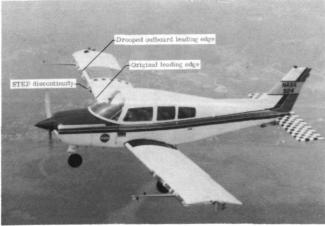
The most difficult piloting task appears to be the mental task of determining the correct propeller to feather. In the high-workload, high-stress environment after the simulated engine failures near the ground, many potentially fatal blunders such as feathering the wrong propeller were committed by most of the pilots who flew the simulator. The next phase of the simulation study will build on this experience and will include an evaluation of automatic control systems to ease the pilot workload in engine-out situations. It is expected that a lowered workload will reduce the chances of the pilot making the potentially fatal mistakes observed in the earlier study.

Eric C. Stewart, 2184

General Aviation Stall/Spin Flight Tests

Stall/spin is a leading cause of fatal general aviation accidents. The majority of such accidents has been attributed to inadvertent stalls and departure from controlled flight at low altitude. Recent flight experiments at NASA Langley have shown that a discontinuous-wing leading-edge design can provide a large increase in outer-wing-panel stall angle of attack and a significant improvement in airplane spin resistance. For example, with its original wing the airplane pictured will enter a spin almost every time that prospin controls are applied. However, with the discontinuous-wing leading edge shown, it will spin less than 3 percent of the time when prospin controls are applied.

Tests conducted with this and another low-wing, single-engine airplane have related autorotative tendencies to the difference between the angle of attack



Research aircraft with discontinuous-wing leading edge.

and the stall angle of attack of the outer wing panels. The summation of increments in angle of attack due to maximum pitch control input, center-of-gravity location, power effects, and dynamic effects have been quantified and correlated well with spinning tendencies. Evaluations by NASA, industry, and FAA pilots of one airplane with a discontinuous-wing leading edge have identified the need to define standards of departure resistance and spin resistance and to establish analytical and/or experimental techniques to determine the level of resistance provided by a given configuration.

H. Paul Stough, 2184

Insect Contamination Protection for Laminar-Flow Wings

Obtaining the maximum benefit of laminar flow for aircraft drag reduction requires maintaining minimum leading-edge contamination from insects. NASA Langley is investigating insect contamination protection methods for laminar-flow surfaces. One promising method currently being investigated is a porous leading edge that has been certificated for ice protection on some aircraft. By seeping a glycol-based solution through a porous leading edge, the wing is kept wet, and, in turn, ice free and potentially insect free. Wind tunnel and flight experiments are in progress to provide design data on the use of such ice protection systems in an insect protection mode.

The flight experiments, conducted from the NASA Wallops Flight Facility, provided data on the factors affecting insect population, insect debris accumulation behavior, and the effectiveness of the porous leading edge for insect protection. The preliminary results show that some of the most significant factors affecting insect population are the type of terrain (water, marsh, grass, and asphalt were tested), local rain accumulation, temperature, and to a much smaller degree, wind speed. It was found that insect collection efficiency varied greatly with altitude and



Test aircraft with porous wing leading edge.

airspeed. Altitudes below 50 ft and airspeeds above 100 mph increased the insect debris accumulation rate. In order to evaluate the effectiveness of this system, it was operated on one wing only, so that direct comparison with the other wing could be made. The initial test results indicate that the porous leading edge offers great promise as a viable insect contamination protection system. Based on these preliminary results, the protection of laminar-flow wings against insect debris contamination appears feasible.

Cynthia C. Croom, 3611

Electronics Directorate

The Electronics Directorate conducts basic research and technology development activities in the areas of aircraft theoretical dynamics and control, aircraft flight management, aircraft flight control systems, spacecraft theoretical dynamics and control, spacecraft information handling systems, remote sensing systems, fault-tolerant systems, electromagnetics, computer science, measurements technology, and simulation technology. These electronics-related research and technology development activities are focused toward application to the next generation of aircraft and spacecraft.

The Analysis and Computation Division provides computational support for all theoretical and experimental aerospace research activities performed at Langley. The Division conducts research and development required to provide mathematical and computer techniques, procedures, and equipment for numerical analysis, problem formulation and programming, electronic computation, simulation, data recording, transcription, transmission, and presentation. Additional responsibilities include conception, design, implementation, and management of advanced centralized data processing systems, flight software systems, and flight simulators, as well as providing consultation on Langley application of computer technology.

The Instrument Research Division provides instrumentation and measurement support for all experimental aerospace research activities performed at Langley, with primary responsibility for the instrumentation of ground-based facilities. The Division conducts research and development programs on sensor materials, components and devices, nonintrusive (optical) and immersion sensing systems, nondestructive measurement of materials, and measurement devices for operating in a cryogenic or reentry environment, and in instrument areas where data requirements exceed capabilities. Additional responsibilities include providing engineering and application expertise to support computer-based data acquisition and control requirements, developing and maintaining measurement standards, calibrating and repairing instruments, and managing an instrument pool.

The Flight Control Systems Division conducts research on flight systems technology for the next generation of aerospace vehicles. The activities of the Division encompass concept formulation, analytical studies, and flight evaluation for flight management capabilities and flight-crucial applications. Specific research involves investigation of fault-tolerant system architectures and their implementation; advanced crew station concepts, including configura-

tions, display media, and input/output technology; and applied controls technology. Flight systems integration and validation research is conducted in AIRLAB, a major new NASA national laboratory. Additional major research efforts are directed to provide more efficient operations of transport aircraft in the evolving national airspace system, cockpit systems to improve crew-vehicle interfaces, aircraft systems and procedures to reduce operating cost and complexity, and improved techniques for performance analysis, workload assessment, and simulation.

The Flight Dynamics and Control Division conducts research on flight control technology for the next-generation aircraft and spacecraft using analysis, simulation, and flight testing. The Division develops and applies new and improved mathematical and optimization techniques to control problems, develops and evaluates manual and automatic digital control system concepts for aircraft and spacecraft, conducts generic research in dynamic system modeling, and performs analysis and simulation studies of the optimal trajectories of flight vehicles. Other research performed in the Division contributes to the technology base required for the design, development, and utilization of teleoperator and robotic devices for space operations.

The Flight Electronics Division conducts research and technology development activities in the areas of environmental sensors, laser components and systems, solid-state electronics, antenna and microwave components, subsystems and systems, and related disciplines for application to sensor, communication, and information processing and data management systems. This technology development is directed toward conceptual design, breadboard fabrication, and proof-of concept evaluation of ground and flight electronics for incorporation in spacecraft and aircraft flight programs.

Crew Systems and Flight Station Concepts for 1995 Transport Aircraft

Until recently, aircraft flight station designs have evolved through the incorporation of improved or modernized controls and displays for individual systems. New displays and controls have simply replaced outmoded units. This ad hoc process, coupled with a continuing increase in the amount of information displayed, has, in many instances, not only produced a complex and cluttered conglomeration of knobs, switches, annunciators, and electromechanical displays, but also frequently contributed

to a high crew workload, missed signals, and misinterpreted information. Now, however, advances in electronic technology offer new concepts in flight station design which provide for safer and more efficient system operation through a reduction in clutter and a more orderly, logical control and communication of information to the flight crew.

A joint effort by NASA Langley, NASA Ames, and the Lockheed-Georgia Company has led to the baseline design of an advanced flight station concept for a 1995 transport aircraft. This has been accomplished through a lengthy process involving mission analysis, technology forecasts, preliminary design, and pilot evaluation in soft mockup. A revolutionary desk top design base was chosen. The location of primary flight controllers was examined for five different designs. The final choice was determined via a complex rating system and was verified through soft-mockup pilot evaluations. Display content locations, color coding, failure switching, and secondary control placements were also evaluated via the soft-mockup evaluation.

The design is being incorporated into flight simulation facilities at Langley, Ames, and Lockheed-Georgia. When interfaced with advanced air traffic control system models, these facilities will provide full mission capabilities for researching issues that will affect transport aircraft flight stations and crews in the 1990's.

Samuel A. Morello, 3621



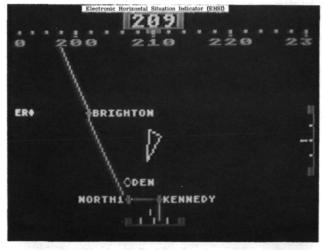
Advanced flight station concept.

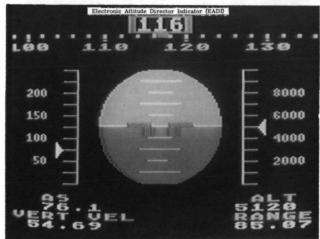
Microcomputer Graphics for Low-Cost Integrated Cockpit Displays

With the increase in graphics capability of personal computers and industrial microprocessors,

the opportunity may now exist to use raster scan, TV-type technology to generate low-cost, pictorially integrated displays for the cockpit environment. The use of this technology is being studied within the Crew Station Technology R&T base program in backup display generators for large, complex cockpits and in primary display generators for small, simple cockpits. In a small cockpit, for example, the new technology might be used to replace several lower reliability electromechanical instruments with one high-reliability microcomputer-driven electronic display.

The research has analyzed graphics-oriented microcomputers, selected a very low-cost candidate, and developed the software to generate a family of experimental integrated flight displays to determine the efficacy of the technology for transfer of information to the pilot. Candidate displays include: Electronic Attitude Director Indicators (EADIs); Navigation Map Display; Engine/Systems Status Indicator; and Check List Display. The analysis has indicated that the microprocessor features needed to support cockpit graphics tasks are vertical blank interrupt for





Microcomputer graphics display.

multitasking, horizontal/vertical fine scrolling of windows or whole display, programmable hardware graphics overlay capability, hardware assists for rapid animation, mixing of graphics and text modes, bit-mapped architecture that allows the programmer to "point" to symbols/graphics, and memory architecture allowing "page flipping" for multimode displays.

The experimental electronics and software have been integrated into a low-cost simulator to allow subjects to "fly" the graphic flight display formats. The simulator has been exhibited at the Experimental Aircraft Association's 1983 Fly-In and Convention at Oshkosh, Wisconsin. Early results of the research indicate that the following performance criteria can be met with very low cost microprocessors: (1) update rates of 2 to 60 Hz; (2) instantaneous switching to selected displays; (3) adequate resolution for medium-complexity pictorial presentation (192 × 320 picture elements); (4) displays using eight or more simultaneous colors; and (5) enhancement of information presentation using aural/voice warnings.

Anthony M. Busquets, 3404

Full-Surface LED Programmable Legend Switch Used for Multifunction Control

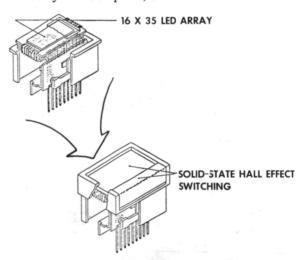
The Crew Station Technology R&T base program has been engaged in joint research efforts with the Air Force and Navy aimed at consolidation of cockpit controls through development of multifunction keyboards consisting of programmable legend switches. One of these research efforts has produced guidelines for the utilization of advanced electro-optical display media and a highly reliable, programmable switch/display technology. The technology consists of a combination of programmable display pushbuttons (PDP) and a logic and refresh control unit (LRCU) which provide the basis for multifunction system architectures designed to declutter vehicle cockpits by reducing the number of dedicated switches and controls.

The PDP features highly reliable solid-state Hall effect switching, a 16 × 35 dot matrix LED array, and tactile feedback. Alphanumeric characters or graphics can be displayed at any location on the array with a resolution of 40 lines per in. The logic unit (LRCU) accepts a seven-bit ASCII code to display two rows of six 5 × 7 characters or one row of three 10 × 14 characters. Individual pixel data are accepted for displaying graphics. The brightness of the display can be controlled in multiple steps under software control

through the LRCU, thus providing full sunlight-to-darkness readability. Display flashing can also be software controlled at 1.5 Hz. The display reliability is ultra-high (over 10⁵ hours).

The LRCU interfaces with the integrated-drive circuitry in the PDP module. The logic and refresh memory is controlled through a fully programmed microprocessor with RS422 or RS232 serial interface to an external host. This programmable switch/display system can be used in a Multi-Function Keyboard (MFK) configuration (by combining multiple PDP's and LRCU's) or individually dedicated to a particular subsystem as a Control/Display Unit (CDU). Laboratory and simulator evaluations are being planned for use as a controller for navigation, communications, and systems management in both the MFK and CDU modes.

Anthony M. Busquets, 3404



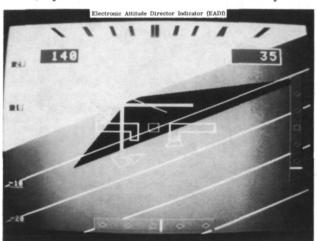
Highly reliable programmable control components.

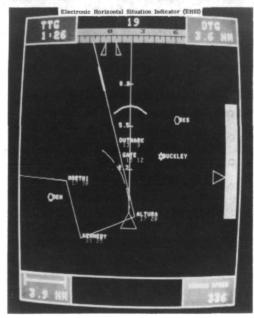
Cockpit Programmable Display Generator Application

Research at NASA Langley has resulted in the readiness of a new Programmable Display Generator (PDG) technology and the demonstration of simultaneous, full-color, three-dimensional, shaded, flicker-free primary flight displays. These advanced displays contain Electronic Attitude Director Indicator (EADI) and Electronic Horizontal Situation Indicator (EHSI) information. Basic concepts, hardware approach, and software development were aided by a research grant to North Carolina State University and development contracts to Ikonas Graphics Systems for hardware and programming language development and to Research Triangle Institute for the

developmental applications software. The culmination of these efforts early this year enabled a demonstration of the dual displays to the aerospace community and over 100 observers. In addition, the system has been selected for incorporation into next-generation simulators now being constructed at Lockheed-Georgia and NASA Ames Research Center, as well as for the Advanced Concepts Simulator at NASA Langley.

The PDG utilizes raster scan (TV-like) technology, color coding, and shading techniques to convey large amounts of pictorially integrated information to the pilot in the most efficient manner. Major features of the PDG include hardware and software character generation of multiple fonts and symbols, dynamic sky/ground shader, variable resolution, variable frame/field rate, interlaced/repeat field modes, dynamic hardware-fill of bounded symbols,





Advanced primary flight displays generated simultaneously.

two- and three-dimensional hardware coordinate transformation, and two-and three-dimensional clipping for windowing, viewporting, and zoom capability. The PDG is expected to have direct application to the next generation of display media, which is flat-panel technology.

M. Jack Neubauer, 3457

Sidestick Controller for Advanced Transport Cockpit Design

Opportunities for more efficient cockpit design in commercial aircraft are numerous with the rapidly changing digital avionics technology. One such opportunity lies in the replacement of the massive control yoke, present in most commercial aircraft today, with less intrusive controllers, since mechanical leverage would not be required in future electric control systems. Major design advantages of using less intrusive controllers include minimizing equipment space, optimizing usable viewing area of the front panel, and improving the pilot interface with subsystems.

As one step toward establishing a design data base for flight deck designers, a piloted simulation experiment comparing a sidestick with panel-mounted controllers was conducted. The experimental setting also contrasted two advanced control-display systems - attitude and velocity vector. The pilot's task included curved approach-through-landing under changing wind and turbulent conditions. Both commercial airline captains and NASA test pilots participated in the experiment.

Results of the control-display system evaluation showed improved tracking and lower physical workload with the velocity vector mode (over the attitude mode). A comparison between performance with sidestick and panel-mounted controllers showed very little difference. Since performance is unaffected and some pilots prefer the sidestick, cockpit designers should seriously consider sidestick configurations for advanced flight deck layouts.

George G. Steinmetz, 3621

Design Advantages of a Stochastic Discrete Optimal-Output Feedback Program

A computer program has been developed by Halyo and Broussard of Information and Control

Systems, Inc., for the stochastic infinite-time optimaloutput feedback problem. The design program has been applied to several types of control problems, including a large-order flutter model with constrained dynamic compensation. Some of the design advantages for the output feedback approach are described here.

- 1. Only chosen states are used for feedback purposes. The inner-loop control system can remain unaltered as desired.
- 2. Estimates of all states are not required. A time-varying Kalman filter with its associated complexity and real-time implementation requirements is not used.
- 3. Low-order filters, such as analog prefilters and digital complementary filters, can be included in the aircraft design model, and their effect on control performance is accommodated when the control gains are computed.
- 4. Actuator dynamics and gust dynamics can be included in the aircraft design model. Their effect on control performance is taken into account when the quadratic cost is minimized, but their states are not fed back and hence do not have to be measured or estimated.
- 5. There is no separation of stochastic performance and closed-loop performance. Increasing the measurement noise on some feedback variables causes the corresponding feedback gains to be reduced when the quadratic cost function is minimized.
- 6. There is an increased flexibility in choosing a control structure when using optimal-output feedback. Each control loop can be designed individually in a hierarchical approach using different measurements for each loop closure.
- 7. The control law can also be designed in an integrated manner; that is, the various controls work in cooperation to achieve the desired maneuvers.
- 8. The new numerical algorithm can be applied to relatively large-order plant models without difficulty.

Aaron J. Ostroff, 3209

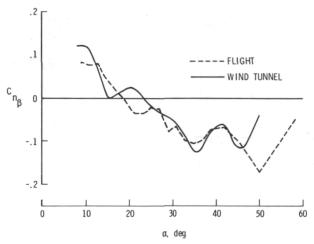
Parameter Estimation in Nonlinear Flight Regimes

As the operating envelope of modern jet fighters is expanded and flight control systems become more complex and crucial, the need for a good aerodynamic mathematical model of the airplane also increases. Currently, math models are derived from extensive wind tunnel testing. Current research in system

identification is aimed at allowing nonlinear model structure determination and parameter estimation from flight test data. In particular, a procedure for the determination of airplane model structure and parameters from flight data has been applied to a modern fighter airplane that exhibits highly nonlinear characteristics. The aerodynamic model equations are based either on polynomials in airplane response and input variables or on polynomial splines that approximate the aerodynamic functions. The selection of an adequate model proceeds through the application of a modified stepwise regression algorithm (MSR) with several information and statistical criteria. The MSR can be applied either to standard small-perturbation maneuvers or to maneuvers involving larger excursions from trim conditions.

An example of the results from the application of MSR to the latter maneuver is presented in the plot of the directional stability parameter $C_{n_{\beta}}$. The solid line represents the wind tunnel test results and the broken line gives the results from the application of MSR to several large-excursion maneuvers performed by the fighter aircraft.

James G. Batterson, 4591

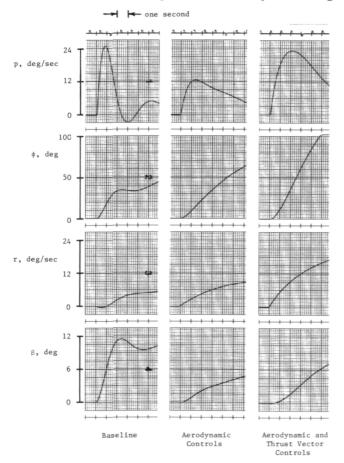


Directional stability derivative determined from flight and wind tunnel tests as a function of angle of attack.

Relative Control Effectiveness Technique With Application to Aircraft Controls Coordination

A relative control effectiveness technique has been developed to give a quantitative measure of the effectiveness of each of several control effectors upon the fundamental modes of a linear dynamic system. By postulating linear combinations of the controls, a set of pseudo controls is formed. The relative control effectiveness measure is then used to formulate a set of optimization problems which yields the proportions of the controls to be assigned to each of the pseudocontrols, with the objective that each pseudocontrol would strongly affect a specific fundamental mode of the system while weakly affecting the remaining modes. The procedure has been demonstrated using the linearized lateral dynamics of a highperformance fighter aircraft. A pseudocontrol designed to affect primarily the Dutch roll mode and another pseudocontrol that primarily affects the roll and spiral modes have been obtained. The figure illustrates the effectiveness of the design procedure in calculating control mixing combinations intended to control the rolling motion of the aircraft.

The first set of baseline traces illustrates the response of the aircraft to a preconceived baseline case that employs ailerons and differential tail operated in unison. This case is objectionable because of (1) the oscillatory nature of the roll rate (p) which causes the bank angle (ϕ) to ratchet, (2) the initial negative response of the yaw rate (r), (3) the rapid rise of the sideslip angle (β), and (4) the eventual cessation of the bank rate, which implies the necessity of holding a



Responses to calculated controls coordination ratios.

substantial lateral control input in order to maintain a desired bank angle. The second set of traces (aerodynamic controls) shows the effect of applying the developed design procedure to the aircraft, considering aileron, rudder, and differential horizontal tail as the control effectors. This case exhibits a smooth increase in bank angle with well-behaved vaw rate and reduced sideslip. The last set of traces shows the effect of adding thrust-vectoring nozzles that produce roll and yaw moments. The addition of thrustvectoring controls has nearly doubled the roll rate capability of the airplane while using modest deflection angles. The apparent improvement of the stability of the airplane was achieved by appropriate gearing of the control effectors without using any feedback loops.

Frederick J. Lallman, 4681

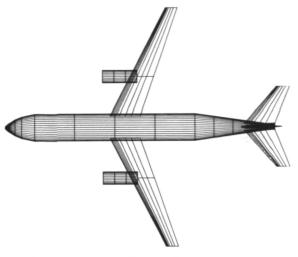
Preliminary Design of Aircraft Using Optimization Techniques

A computer program has been developed at NASA Langley to evaluate the impact of new technologies on commercial aircraft. OPDOT (Optimum Preliminary Design of Transports) utilizes nonlinear programming techniques for finding optimum conceptual designs of subsonic transport aircraft. Program inputs include mission profiles, economic assumptions, nonlinear aerodynamics, operating requirements, and design constraints. OPDOT finds the best set of design parameters (e.g., wing area, wing aspect ratio, installed thrust, etc.) to optimize a performance index, such as return on investment, while satisfying all constraints and mission requirements. By properly specifying in the input data a new technology under consideration, a sensitivity study illustrating the economic trade-offs of applying that technology can be made. In this manner, research results can be hypothetically included in a resized configuration that realizes the maximum synergistic benefits obtainable from its use.

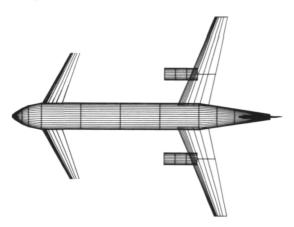
OPDOT has been used to document the expected gains in commercial aircraft performance from the utilization of active controls. Optimized designs with and without the assumption of active controls were compared to show that transports that take full advantage of relaxed static stability, gust load alleviation, and flutter suppression are expected to achieve nearly 10 percent fuel savings. Recently, comparisons have been made between conventional aft-tail and proposed canard configurations, as shown in the figure. Studies showed that conventional configura-

tions were economically superior to canard configurations for this class of airplane, indicating that other areas of research are more promising. Research is continuing in the areas of multibody (two or more fuselages), multisurface (canard with aft-tail), poweredlift, and commuter transports.

Steven M. Sliwa, 4681



Baseline conventional aft-tail transport design generated by OPDOT.



Baseline canard transport design generated by OPDOT.

Probability of Cloud Encounter on Long-Range Airline Routes

Cloud detection observations previously obtained in the Global Atmospheric Sampling Program (GASP) have been analyzed further to develop an empirical model for estimating the probability of cloud encounter on long-range airline routes. Such estimates are needed because theory and limited operational experience to date predict the laminar

flow control (LFC) effectiveness will be degraded during cloud encounters. Therefore, to assess the economic practicality of flying an LFC-equipped aircraft on a given route, the probability of cloud encounter along that route must be estimated. The current study is an extension of the work previously reported (NASA Langley 1982 Research and Technology Annual Report), which presented the probability of encountering clouds at any one location. That analysis has been extended to model the average percentage of time-in-clouds to be expected along entire routes.

Frequency distributions of the route average percentage time-in-clouds encountered along several long-range routes were analyzed and calculations were performed for three altitude bands in the 8.7- to 13.3-km-altitude (28,500 to 43,000 ft) region. It was found that the distributions for all routes and altitude bands could be modeled well empirically by gamma probability density functions of the form

$$f(TIC_F, \alpha, \beta) = \frac{1}{\Gamma(\alpha)\beta^{\alpha}} (TIC_F)^{\alpha-1} \exp(-TIC_F/\beta)$$

with α = 0.7 and β = TIC_F/0.7. Thus, a mathematical model for calculating the probability of encountering a specified amount of cloud coverage along a given route-altitude profile has been developed for the first time. The model requires only an estimate of the average time-in-clouds for the given route; this is readily available from the previous analyses of GASP data.

In the preceding equation, f denotes the expected frequency on any given route-altitude band of a route-average percentage time-in-clouds TIC_F, and TIC_F is the average value derived from the GASP sample of all flights in the route-altitude band.

From analysis of these routes, it was concluded that upper bounds for probability exceedance are as presented in the table. Thus, these results indicate that the probability of encountering extensive cloud cover on long-range airline routes is not, a priori, high enough to make LFC economically unfeasible.

Richard E. Davis, 3761

Probability that Average Enroute Altitude band Cloudiness Will Exceed				
	5%	10%	25%	50%
8.7–10.2 km (28,500-33,500 ft)	0.55	0.35	0.10	0.02
10.2-11.7 km (33,500-38,500 ft)	.50	.31	.08	.01
11.7-13.3 km (38,500-43,500 ft)	.25	.08	.01	~ 0

Cloud Particle Detector

Recent studies and ongoing flight tests indicate that application of laminar-flow technology to the wings of medium and large commercial transport aircraft may result in significant drag reduction with mission fuel savings of about 25 percent. A flight test program conducted in the 1960's which incorporated laminar-flow control (LFC) on a swept-wing aircraft (X-21) illustrated that laminar flow was lost while encountering cirrus clouds. Therefore, to realize optimum laminar-flow effectiveness, it is desirable to fly LFC aircraft outside of clouds, and a reliable cloud detector device is required as a cloud avoidance aid.

Taking advantage of the phenomenon that leading edges of aircraft surfaces are charged when ice and water particles strike them during flight, a durable, low-cost cloud particle detector was developed by NASA Langley. A miniature electronic amplifier conditions the signal from the chargemeasuring surface to form a high-sensitivity cloud particle sensor. A small electrically isolated section (patch) of aircraft-quality aluminum was bonded to the leading edge of the vertical stabilizer on the Langley F-106 research aircraft. A series of laboratory experiments with various nonconductive bonding materials revealed that a thin layer of silicon rubber provided excellent adhesion and superior chargesensing characteristics when compared to several types of epoxy adhesives. The epoxy adhesives tested exhibited undesirable long-term charge retention properties. The electronic circuitry consists of a current sensing resistor and a two-stage integratedcircuit voltage amplifier to measure the charging rate as well as to provide dual-range particle sensitivity.

Data from more than 20 flights of the F-106 research aircraft revealed that the detector is a very reliable indicator of the type of clouds that will cause problems for LFC aircraft at cruise altitude. The detector was able to detect and survive heavy rain conditions and was also able to detect subvisible ice particles in very thin cirrus clouds. Future plans call for the detector to be flown onboard the NASA Jetstar aircraft as part of the Leading-Edge Flight Test Laminar Flow Program.

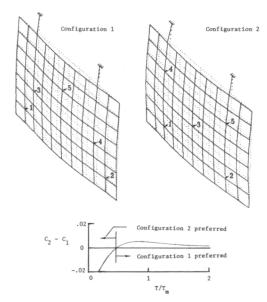
Richard E. Campbell, 3761

Incorporating Reliability

A minimization criterion has been developed to determine optimal sensor and actuator placement considering mission life and the reliability of control system components. It has been applied to determine the optimal actuator placement for vibration control of a grid, as shown in the figure. It is assumed that the actuator loads are to be readjusted following failures, but that the locations cannot be changed. The goal of the design is to minimize an integral quadratic performance index involving deflection and control effort terms. When the reliability of the actuators is considered, a more useful measure is the expected value of the integral error, that is, the sum of the integral square error for each possible failure state considered, multiplied by the probability that the failure state will occur. This, then, is the criterion used to select the actuator locations.

The figure shows the difference in the optimal criterion for the two sets of actuator locations considered as a function of the ratio of the design mission life or reservicing interval (T) to the mean time to failure of the components (T_m) . The figure shows that the optimal location of the actuators corresponds to configuration 2 for short mission life and configuration 1 for long mission life.

Raymond C. Montgomery, 4591



Selection of optimal actuator location as a function of ratio of design mission lifetime to mean time to failure.

Teleoperator Control With Simulated Transport Delays

A teleoperator/robotic system simulation capability is being developed to support research and technology programs related to remote space operations. Inputs to the simulation are from a manned control station in Langley's Intelligent Systems Research Laboratory (ISRL). The simulation can generate high-resolution graphics displays and/or drive manipulators in ISRL. The initial version of the simulation used a computer graphics display to examine the effects of two control modes (joint-byjoint and resolved rate), a proximity display scheme, and time delays (up to 2 seconds) on the control of a five-degree-of-freedom manipulator performing an end effector alignment task. Results of the study showed that the task took more than three times as long with joint-by-joint control as with resolved rate control, which decoupled translation and rotation control. Subjects replaced continuous control with a move-and-wait strategy for time delays of 0.25 sec and longer. The time required to perform the simulated task increased linearly with time delay, but time delays had no effect on alignment accuracy. Later studies will investigate displays and controls utilizing force, torque, and proximity sensors from the manipulator end effector, and automated trajectory planning methods that consider time and energy requirements and physical constraints.

Jack E. Pennington, 3871

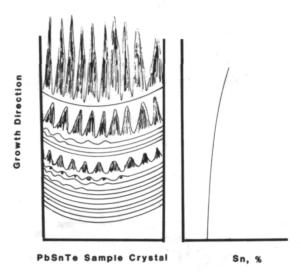
Etching Techniques for Interface Demarcation in Compound Semiconductors

Interface demarcation during the growth of semiconductor crystals from the melt have been studied. A short current pulse through a sample during the growth of a crystal from the melt results in slight variations in the composition of the crystal. Delineating etches that show these compositional variations result in a time history of the evolution of the interface shape during the growth process. This study deals with the development of delineating etches for the compound semiconductor lead-tintelluride (LTT).

Thermodynamic calculations for LTT indicate that the solvated ions react spontaneously in solution to produce lead, tin, and tellurium metals, which deposit back onto the surface immediately. This results in an obscuring plaster that coats the freshly etched surface and prevents observation of the surface. Electrochemical etching leads to a controlled process that prevents the formation of this metallic deposit. Dilute chemical reagents, controlled voltages, high ionic strengths, complexing reagents, and heterogeneous surfaces were used to develop etches

for LTT. Successfull etches have been based upon the chemistry of collodial sulfur, potassium hexacyanoferrate, and ethylenediaminetetraacetic acid (EDTA). The results are illuminating, showing periodic lines during the initial growth. As growth proceeds, oscillatory instabilities begin to occur with the interface, which eventually breaks down completely. This is the first time such behavior has been observed, although it has been predicted theoretically.

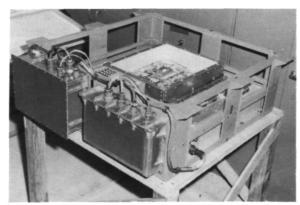
Roger K. Crouch, 3777

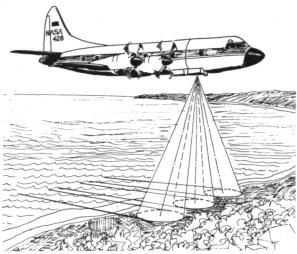


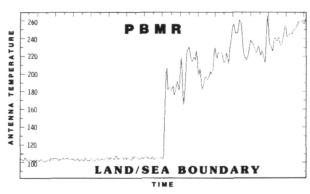
Schematic diagram of interface growth shapes of lead-tin-telluride and accompanying tin content of sample.

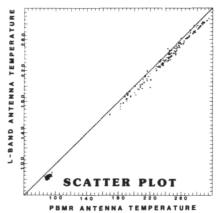
Pushbroom Microwave Radiometer

The fabrication, development, and testing of the Pushbroom Microwave Radiometer (PBMR) was completed this fiscal year. The PBMR was developed to provide technology and form a test bed for pushbroom radiometer technology for proposed radiometric missions on large space systems. The photograph shows the completed PBMR hardware as well as a portion of the flight test results. In the photograph of the PBMR radiometer assembly, the thermal enclosure is removed to show the four front ends and the mixer-preamp section. The sketch illustrates the pushbroom concept and the flight test configuration. In addition to the PBMR, an existing verified singlebeam L-band radiometer was also onboard the aircraft. The output of this verified instrument was then compared to the center beam of the PBMR. The graph is the response of the PBMR measured antenna temperature as the beam passes from water to land. These data were then compared to the antenna









Microwave sensor technology.

temperature measured with the verified instrument and are presented in the scatter plot.

Further results of measured salinity and soil moisture also verified that the PBMR was performing as designed. The PBMR was then installed on the NASA Wallops Skyvan as the primary sensor on the 1983 AgriSTARS soil experiment. The PBMR performed without anomaly throughout the entire mission. During the next fiscal year the PBMR will be flight tested on a four-beam pushbroom configuration. The technical objective of the second flight test phase is to investigate the effect of different beam-to-beam pattern crossover levels and their effect on geophysical parameter imaging.

Richard F. Harrington, 3631

Wedge Fiber Feedback Decoupler Demonstrated

A "roof"-type wedge fiber was developed to eliminate optical feedback into semiconductor lasers. An optical fiber (125 μm diameter) was polished to a wedge angle of 110°. It was then used to couple the output of the semiconductor laser into the optical fiber. With proper alinement through use of micromanipulation to position (then glue in place) the fiber and monitoring of the spectral output, increased power coupling (20 percent) and spectral control of the semiconductor laser were achieved. The wedge fiber feedback decoupler allows normal spectral tuning of the laser as a function of drive current and cooler heat sink temperature without the abnormal wavelength and modal shifts experienced when optical feedback was present.

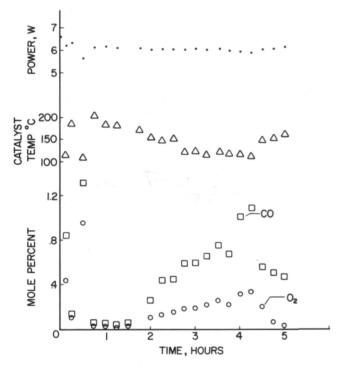
Herbert D. Hendricks, 3777

Evaluation of Catalysts for Closed-Cycle Operation of CO₂ Laser

High-energy pulsed CO₂ lasers have a potential for measuring many different features of the Earth's atmosphere. For this purpose they are most useful on an airborne or space platform. In this application, the laser must be operated closed-cycle to conserve gas, especially rare chemical isotopes of CO₂. The laser discharge decomposes the CO₂to CO and O₂, which causes a rapid loss in power and leads to erratic behavior. To maintain operation, the CO and O₂ must be recombined to form CO₂. This conversion can be done by passing the gas mixture over a heated catalyst.

Two different catalysts have been evaluated inhouse for conversion efficiency. One was a mixture of copper, cuprous oxide, and cupric oxide (Cu/Cu₂O/CuO) and the other was platinum chemisorbed on tin oxide (Pt/SnO₂). With the coppercopper-oxide catalyst at 265°, the laser was operated continuously for 6-1/2 hours at 80 percent of open system power. With the Pt/SnO₂ catalyst, the laser was operated continuously for 5 hours, during which time the emitted power was 95 percent of the opensystem power at a catalyst temperature of 200°C and 90 percent at 120°C. Operating results for the Pt/SnO₂ catalyst are plotted in the figure. The dissociated CO and O2 recombined to form CO2 as the catalyst temperature was increased after 4 hours of operation.

Irvin M. Miller, 2466



Closed-cycle operation of CO_2 laser (10 pps) using platinum on tin oxide catalyst.

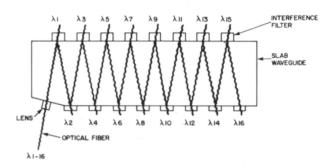
Fiber Optic Zig-Zag Wavelength Demultiplexer Demonstrated

The transmission of light signals over fiber optic cables has been fully demonstrated, but it remains to continue the expansion of the data transmission capability by controlled addition of optical data on different wavelengths. This concept, called wavelength division multiplexing, has been developing at a fast

pace and requires new lasers with different wavelengths and new methods to separate the different wavelengths (i.e., a wavelength demultiplexer).

A demultiplexing concept demonstrated at NASA Langley is based on the design shown in the figure. The zig-zag wavelength demultiplexer uses a glass waveguide to contain the light and interference filters (790 to 860 nm) placed along the waveguide to select a specific wavelength and reflect the other wavelengths down the waveguide. The initial design was demonstrated to work at 20 Mbits with a 10^{-9} bit error rate with an insertion loss of 8 dB at the ninth channel. Currently a miniaturized version is being developed to further reduce the insertion loss.

Herbert D. Hendricks, 3777



Ten-nanometer zig-zag wavelength demultiplexer.

High-Density Wide-Temperature-Range Bubble Device

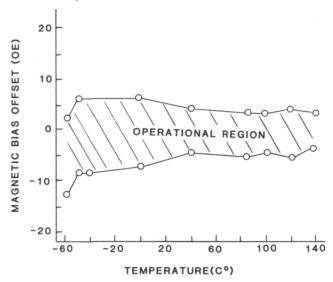
A new bubble domain material and advanced magnet tracking technique have been combined to develop a high-density bubble memory device. Device operation over the range from -54°C to +140°C was successfully demonstrated with a 2-Mbit device based on 8-µm-period data site spacing and wide-gap permalloy component technology (see figure). The new bubble material is a bismuth-based garnet with the composition (YBiGdHoCa)₃ (FeSiGe)₅ O₁₂.

To overcome the temperature tracking mismatch between the bias magnet and the garnet material, a composite magnet structure was developed. With this structure, several insert plates of Cu-Ni alloys and polycrystalline dysprosium iron garnet are located in series with the conventional plates of barium and MnZn ferrites. The selection of insert plates optimizes the temperature tracking over the range of operation.

These device advancements were accomplished as part of a joint DOD-NASA research contract with Bell Laboratories in an effort to simultaneously increase device density and temperature range. The work is being extended over the next year to demon-

strate a similar operating temperature range for 4-Mbit devices. Bubble devices of 4-Mbit capacity and greater are expected to meet a need in onboard memory systems for critical-data storage.

Paul J. Hayes, 3777



Wide-temperature operation of 2-Mbit device.

CMOS Sum-of-Products Integrated-Circuit Development

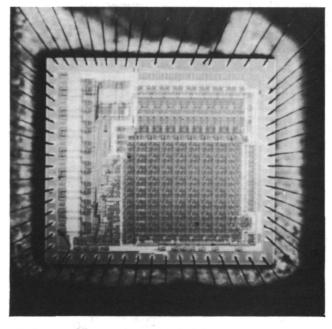
Before any NASA Earth Resources Satellite multispectral imagery data can be processed, sensing element nonuniformities must be removed and scene illumination differences and map projection to standard topological projections must be accomplished. Previous study results indicated that a recurring mathematical primitive computational element that is necessary to the solution of a broad host of these problems is the inner product, or vector dot product. To relieve the general-purpose computer of the calculational burden of this simple functional calculation on all the sensor data through the calibration, scene intensity normalization, and projection processes, it was decided to implement a sum-of-products device on a single chip in low-power complementary metal oxide silicon technology.

This high-speed low-power complementary metal oxide silicon (CMOS) integrated circuit was initially designed, modeled, and fabricated with NASA funding and is now commercially available. In addition to in-house evaluation to determine suitability for multispectral data processing, initial production run chips were also made available through the Office of Aeronautics and Space Technology to the Jet Propulsion Laboratory Advanced SAR (synthetic-

aperture radar) and Venus Mapper developmental process. The CMOS circuit has been tested to achieve equivalent performance at one-tenth the power of previously available processing elements.

The manufacturer of this product, Analog Devices, is continuing to offer similar products in the commercial and military marketplace, and NASA involvement in the actual design and production has been completed.

Harry F. Benz, 3535



High-speed low-power CMOS integrated circuit.

Feature Classification in Hardware

Vast amounts of multispectral imagery are generated by the NASA Earth Resources Satellite systems. Processing these imagery data to extract significant feature data requires extensive statistical calculation and modeling. This processing is lengthy in general-purpose Von Neumann type computer architectures, which limits the utilization of these data to land use application because of the simple algorithms and to geologic exploration because of the high payoff. Other applications such as flood plane mapping, forest management, crop estimation, and crop health evaluation are not suitable because of the prohibitive cost of reducing these data.

Preliminary studies conducted by NASA Langley have shown that maximum-likelihood classification rules solve a broad class of Earth resources classification. This classification methodology has been implemented in special-purpose hardware. The first

technology implementations have been in charge transfer analog device technology and, more recently, in low-power complementary metal oxide silicon (CMOS) technology. A joint effort by NASA Langley, North Carolina State University, Research Triangle Institute, Texas Instruments, Analog Devices, and Chronometrics has led to the final development of this hardware classifier.

The supporting equipment for this hardware feature classifier has been installed and debugged at Research Triangle Institute. The development of the special-purpose hardware is nearing completion. The necessary boards have been fabricated and are undergoing debugging at a reduced level of effort. Ultimately, over the next year, this system will be used as a stand-alone classification facility for a broad number of governmental and non-governmental users.

Harry F. Benz, 3535

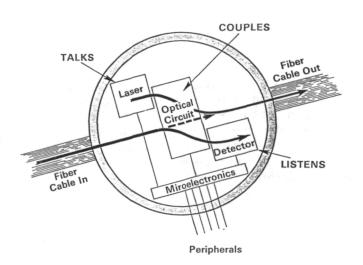
Adaptive Optic Nodes for Computer Networks

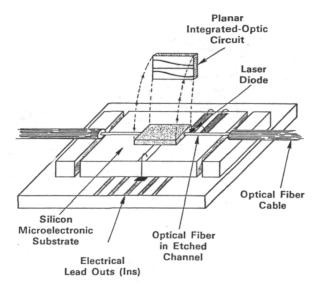
A major problem facing NASA in the design of an overall Space Station information system is the implementation of a self-correcting, self-repairing computer network with adaptive nodes. In view of the projected data rate this network will have to handle (over 90 MHz), it has been generally agreed that the network communication links will have to be optical fibers. However, with the technology available presently, the use of optical fibers requires the use of optical-to-electrical (O/E) and E/O conversion at each node. Since these conversions require additional components and power, and represent a potential system bottleneck, there would seem to be much to be gained by constructing nodes which minimally would allow the passage of optical signals without O/E and E/O conversion and which should, ideally, perform many of the smart-node logic functions using optical rather than electronic techniques.

A study has been completed which developed the definition of smart optical nodes for implementation in a self-correcting, repairing computer network to be used in an overall Space Station information system. This study also investigated the ability to use smart optical nodes combined with optical fiber network communication techniques. Several likely device concepts were addressed which can be implemented into a Space Station information system. Several points emerged quite clearly from the study. The most important is that in order to make optimum use of the advantage offered by the optical approach and to

minimize the effect of the accompanying disadvantages, the network architecture, protocol design, and nodal hardware design must be undertaken with the characteristics and capabilities of the optical approach kept firmly in mind. This means that, at the present time, it is impossible to specify the details of nodal designs, since these will have to evolve along with the other network concepts. However, a conclusion of the study was that there are a number of hardware features that are common to almost all conceivable nodal designs. These features include items such as fiber-to-node coupling, single-mode channel waveguides, and switches of varying degrees of complexity. A result of this work will be a fully assembled fourport switch with attached fiber pigtails. This integrated optical circuit will then be the basis for more sophisticated future devices.

Marvin E. Beatty III, 3535





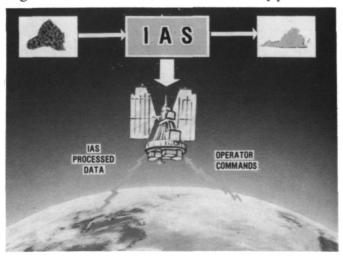
Adaptive optic-node concept.

Information Adaptive System

Space applications and science missions generate vast quantities of sensor data that are currently transmitted in entirety to the ground regardless of information content or user interest in the data. This mode of operation places a significant burden on the ground facilities and results in high processing costs and long delays in providing users with processed data. One solution is to introduce intelligence into the sensor by coupling it with an adaptable, onboard processor. Information could then be extracted from the raw sensor data prior to transmission, which would drastically reduce the amount of data that must be transported to the ground. The Information Adaptive System (IAS) program represents a first step toward realizing this capability by addressing the challenging task of processing high-speed data onboard the spacecraft.

A laboratory version of the IAS was developed for NASA Langley by Martin Marietta Aerospace Corp. to evaluate and demonstrate the suitability of the system design to spaceborne, multispectral-image data processing. It was installed at Langley in February 1983. The IAS experimental electronics accepts and processes data from a simulated multispectral linear array at a rate of 76.8 megabits per second. Functions performed by the IAS include radiometric correction, cloud detection and editing, data packetization, geometric-coefficient processing, and adaptive system control.

Test support software was developed at Research Triangle Institute for the IAS evaluation activity and was successfully integrated into the system. Results of initial evaluations indicate that the high system throughput rate was achieved without sacrificing processing accuracy. Demonstrations of the IAS began in June 1983 and have been viewed by personnel



Development of an onboard data-processing system.

from NASA Headquarters, Goddard Space Flight Center, Honeywell Corp., Charles Stark Draper Laboratory, and Cornell University. Anyone who is interested in attending a demonstration is encouraged to call the contact for this item.

Barry D. Meredith, 3535

Image Plane Processing of Visual Information

Like human vision, most current approaches to computer, or robotic, vision include edge enhancement as an initial image-processing step. However, unlike the mechanism of human vision, which performs edge enhancement during image formation, the current practice in computer vision is to perform edge enhancement by digitally processing image data after they have been acquired with conventional imaging systems (usually television cameras for sensor array devices).

Research at NASA Langley has demonstrated that the use of Shannon's theory of information for communication channels to optimize the design of imaging systems that use neighborhood image plane processing for edge enhancement leads to a spatial response similar to that of human vision. This response has been shaped by evolution to efficiently acquire and process essential visual information for subsequent pattern recognition. Processing images during their formation (i.e., in the image plane), as in human vision, improves edge enhancement and minimizes the amount of data transmission and processing required for scene analysis and pattern recognition. Image plane processing also permits the neighborhood weighting parameter to control the spatial response of the imaging system, in order to trade edge enhancement for sensitivity at very low light levels.

Friedrich O. Huck, 3535

Multiple-Beam Feeds in Large Space Antenna Systems

An initial concept for a multiple-beam multiple-aperture antenna system configuration is being designed which would provide communication coverage for the continental USA. A feed cluster design and development is under way which would be compatible with the multiple-beam multiple-aperture reflector antennas system concept, with the potential for application to the Land Mobile Satellite Service (LMSS).

The design and analysis of the feed cluster has been completed and the development of a prototype model has been initiated. This prototype model will be evaluated and used as a feed for testing the 15-m model of the hoop-column antenna in the near-field facility at Martin-Marietta Denver.

Scale model testing is continuing to aid the development of analytical techniques for large mesh reflector antennas. The electromagnetic characteristics of surface distortions, circular versus pie aperture shapes, feed spillover onto adjacent apertures, and illumination taper are being studied and the effects on the antenna system performance are being evaluated. These scale model tests will be used to further refine the analytical models for the design of large space antennas for future applications.

Thomas G. Campbell, 3631

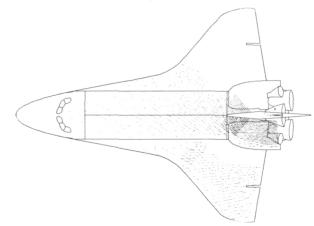
Computer Analysis of Shuttle Infrared Lee-Side Thermal Sensing Experimental Data

The SILTS (Shuttle Infrared Lee-Side Thermal Sensing) experiment will use an infrared imaging radiometer to measure the radiation emitted from the Space Shuttle's lee side (one wing and the fuselage) during reentry. Temperature of the specific locations on the surface will be inferred from radiation levels and from knowledge of surface emittance. In order to couple the radiometer scan to the Shuttle surface geometry, an algorithm was developed which incorporated Space Shuttle shape, location of specific Shuttle surface materials, and the measurement geometry between the camera and the surface. Chord data from the Shuttle were used to develop a bivariate grid which fixed the lee-side Shuttle geometry. Nodal points were then defined to adequately resolve all the chords in a group. Boundary information was generated to differentiate between groups of chord information. By bivariate interpolation the groups were merged to cover the entire lee side of the vehicle.

An algorithm similar to an optical ray trace approximated the actual point of intersection of the radiometric measurement with the leeward surface of the vehicle. Shadow areas were automatically determined by this process. A data base containing surface information was generated which provided the emittance correction required for temperature determination. Thus, with the knowledge of point of intersection of a measurement with the vehicle and the use of the surface information, emittance corrections were made point to point.

The specific scan pattern of the SILTS camera as projected onto the Shuttle surface is shown in the figure. The flight camera system will supply 400 lines of scan per field, which is roughly 10 times greater than the number of lines shown. This process reduces infrared imaging data generated from a complex shape target to a surface temperature map even when the camera is not normal to the surface.

Andronicos G. Kantsios, 2466



Scan pattern of SILTS camera.

Computational Approach Resolves Questions on Chemistry of Fluorine Oxide Radical

Molecular radicals such as fluorine oxide (FO) are frequently difficult to work with in the laboratory because they are difficult to form and they disappear rapidly due to reactions with other molecules and the walls of the reaction chamber. The FO radical, which may be generated by the breakdown of fluorocarbon aerosol propellants in the stratosphere, is doubly difficult because so far it has not been detected by either optical (UV/visible) or electron spin resonance spectroscopy. Although the presence of the radical was inferred from several different experiments, its elusive nature led to uncertainties with respect to its stability and photochemistry.

The molecule was finally investigated computationally at NASA Langley using the fundamental equations of quantum mechanics. The results explained the failure of the previous experiments and yielded additional new information as well. The potential-energy curves for the excited states indicated that instead of absorbing ultraviolet energy in narrow bands leading to detectable spectroscopic lines, this radical would absorb a broad range of energies leading only to a diffuse (undetectable) continuum.

Chemically, the radical would break down into its constituent atoms under the action of ultraviolet light. The dipole moment function was found to go through zero near the equilibrium bond length, which would make the electron spin resonance signal vanishingly small. The results also yielded line strength information for the vibrational transitions which can be used to detect the molecule, and they confirmed that the radical is more stable than indicated in the thermochemical tables.

Donald H. Phillips, 2466

Efficient Sparse Matrix Multiplication Scheme for CYBER 203

An efficient storage-computational algorithm has been developed to perform the matrix-vector product b = Ax on the Control Data CYBER 203 where the matrix A is assumed sparse and symmetric. The desire to provide software that gives the user a choice between the often-conflicting goals of minimizing central processing unit (CPU) time and minimizing storage requirements has lead to a diagonal-based algorithm in which one of three types of storage is selected for each diagonal. For each storage type, an initialization subroutine estimates the CPU and storage requirements based on results from previously performed numerical experimentation. These requirements are adjusted by weights provided by the user which reflect the relative importance the user places on the two resources.

The three storage types (denoted type I, type II, and type III in the table) were chosen to be efficient on the CYBER 203 for diagonals that are dense, moderately sparse, or very sparse, respectively. However, for many densities no diagonal type is most efficient with respect to both resource requirements. The user-supplied weights dictate the choice.

The table shows results for a finite-element problem with 1086 equations and a bandwidth of 81.

Storage-Computational Algorithm Results for a Typical Finite-Element Problem

$C_{\mathbf{W}}$	$s_{\mathbf{W}}$		Storage (words)	Dia I	agonal ty II	pes III
1	0	7.2	13,883	8	0	73
0	1	16.7	8,032	1	72	8
0.5	0.5	7.8	9,517	3	10	68
.7	.3	7.5	9,749	3	4	74
.3	.7	8.8	9,092	3	20	58

For each combination of user-provided weights, denoted C_W for CPU and S_W for storage, a significant change can be seen in the number of diagonals that the initialization subroutine assigns to each storage type. The resulting storage and CPU requirements can be seen to be consistent with the user's choice of C_W and S_W .

Jules J. Lambiotte, Jr., 4612

Integrated Verification and Testing System for HAL/S Programs

Major elements of the Integrated Verification and Testing System (IVTS) are installed and operational on the Control Data CYBER-NOS computers at NASA Langley. The system is currently undergoing testing and evaluation by Langley personnel. One major component (the Symbolic Execution Tool) is still under development to enhance its capabilities.

The IVTS uses the Langley Level 23 HAL/S compiler and the production versions of the execution tools for HAL/S programs being used by programmers working for the Advanced Transport Operating Systems Program Office. An IVTS Mini-Manual for users has been developed and the system maintenance documentation is currently being revised and enhanced under the development contract extension with Boeing Computer Services.

The major IVTS analysis tools may be considered and used as a series of error filters ranging from compile-time lexical and syntactic analysis to static analysis, symbolic execution, and dynamic (executetime) analysis. All of the IVTS analysis tools up to dynamic analysis are static in nature (i.e., do not require execution of the HAL/S program under analysis) and require only a compilable unit of HAL/S code. The static tools work on an internal form of the HAL/S program produced by the compiler and do not duplicate any of the compiletime activities. The dynamic analysis component requires an executable unit of HAL/S code and will enable selective instrumentation (via asserts/keeps) of the program code by the user prior to initiation of each test execution. Instruments can be invoked by the user as in-line executable code or as marked code packets that will permit noninterference testing in a simulator/emulator environment.

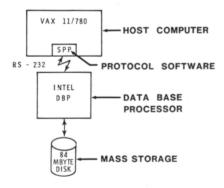
Edmond H. Senn, 2558

Database Processor

A database processor is (1) software that provides a host computer, via a communication link, with a set of semantically large instructions for data management: (2) a dedicated computer to mount the software upon; and (3) a mass storage device (disk) to hold data. A conventional computer has instructions such as add, subtract, test, and jump. The database processor has instructions such as define a data dictionary/directory; search, identify, and return sets of information which meet specific criteria; and locate data by navigating through logically connected information sets. An Intel database processor has been contributed to ICASE (Institute for Computer Applications in Science and Engineering), and experience is being gained by linking it to the VAX 11/780 in the IPAD (Integrated Program for Aerospace Vehicle Design) Project Office.

A simple, functionally limited prototype data management system for the database processor has been designed, tested, and documented. This required the development of (1) service port protocol software (SPP) to perform the low-level communication between the VAX 11/780 and the database processor (DBP); (2) software to construct blocks of DBP instructions and decode the blocks of DBP responses; and (3) software to provide the human interface to the DBP instruction blocks. The human interface software currently is functionally limited but can be expanded to a system for engineering and scientific data management.

Floyd S. Shipman, 3375



The physical DBP environment.

Design Methodology for Concurrent Systems

In most parallel machine design, the basic hardware decisions are fixed at an early stage, long before the software organization and external environment have been considered in detail. This traditional approach often leads to major problems at later stages, since it may be necessary to distort the software and external supporting environment to match the fixed hardware organization. This distortion frequently leads to significant degradation of system performance.

A new design methodology has been defined recently at ICASE (Institute for Computer Applications in Science and Engineering). This method considers the system to be composed of four layers of virtual machine: (1) the applications user's machine (e.g., command language); (2) the application programmer/numerical analyst's machine (e.g., applications language); (3) the systems programmer's machine (e.g., operating system structure); and (4) the hardware itself. Each layer of virtual machine is defined formally during the design process. Advantages of this design approach are expected to be the ability to consider system structure (e.g., inputoutput devices, global control strategies, outside interfaces), perform detailed studies of various levels of parallelism, and iterate the design until a proper match of hardware and software organizations is found. Simulation of the total system design will permit performance evaluations. To date, basic concepts of this design methodology have been formulated and are being evaluated by studying a concurrent system motivated by applications in structural analysis.

Susan J. Voigt, 2083

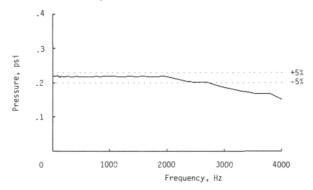
Dynamic Pressure Standard Sets Accuracy of Wind Tunnel Data

Research at NASA Langley to improve a dynamicpressure calibration standard based on earlier work done by the National Bureau of Standards using a vibrating liquid column has resulted in a significant increase in the capability of this standard. The standard consists of a liquid-filled cylindrical vessel driven by an accurate vibration exciter to produce a sinusoidally varying pressure which is accurately described by measurements of the acceleration force and the fluid column's height, density, and temperature. Previous developments using this technique have had an upper frequency limit of 1 kHz. The new development uses a thick-walled lightweight aluminum cylinder to increase the mechanical stiffness, a cylinder with a conically shaped exterior to lower the center of gravity of the system, a specially designed clamping mechanism to rigidly mount small ball

bearings used to control fluid damping characteristics, and a vacuum bell jar system to eliminate absorbed air in the fluid. Experiments have shown that this improved design provides the capability to produce dynamic pressures accurate to within 5 percent over a frequency range of 40 to 2500 Hz.

The primary application of this device will be the accurate calibration of dynamic-pressure transducers used for the measurement of unsteady aerodynamic effects on wind tunnel models.

Paul C. Schutte, 3234



Typical pressure transducer calibration using improved technique.

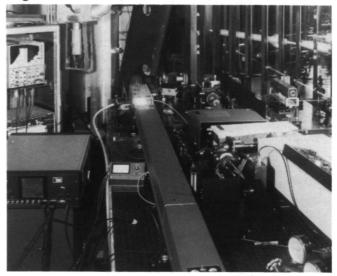
Raman Doppler Velocimeter Tests at Supersonic Speeds

Recent developments in the application, measurement, and analysis of stimulated Raman spectroscopy have shown that the velocity of test medium molecules can now be determined from Doppler shift principles without particle seeding. The method employs two lasers to stimulate specific Raman spectrum signals to measurable levels. By combining this velocity-measuring capability with standard Raman techniques for temperature and density measurement, a totally nonintrusive device is available for flow field surveys. The capabilities of a Raman Doppler Velocimeter (RDV) are ideally suited for high-speed flows, particularly where shock waves, rapid expansions, strong vortices, and separated-flow regions occur.

Initial tests were conducted in the Langley Unitary Plan Wind Tunnel (UPWT) at Mach numbers from 3.0 to 4.5 to develop and evaluate the RDV system for measuring supersonic flow fields. A continuous and a pulsed laser beam each enter the test section windows at a 65° horizontal inclination to the tunnel centerline. Comparisons of the RDV-measured free-stream Mach number with tunnel calibration

values differed by 6 to 8 percent; the differences were due primarily to inaccuracy in the temperature measurement. Differences of only 1 to 6 percent occur when the tunnel calibration value of static temperature is used. These first attempts to use the RDV in a research wind tunnel have produced encouraging results. Future tests are planned to enhance the signal quality through improvements in laser resolution, signal acquisition, and data processing.

Reginald J. Exton, 2791



RDV system in Unitary Plan Wind Tunnel.

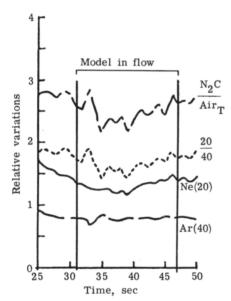
Method of Measuring Mixing Ratio of Film Cooling Nitrogen to Tunnel Gas

A method for determining cooling gas-air mixing ratios in high-enthalpy flows using cooling nitrogen (N_2) seeded with inert neon (Ne) gas as the tracer and naturally occurring inert argon (Ar) gas in the air as an internal reference for mass spectrometric measurements was developed and demonstrated in the Langley 8-Foot High-Temperature Tunnel. The method involved sampling of the boundary layer flow over the model through either a flush orifice or a surface pitot inlet connected through small-diameter tubing to a quadrupole mass spectrometer, where Ne and Ar at mass units 20 and 40 respectively were measured and recorded continuously during a tunnel run. The figure shows typical mass spectral data for Ne and Ar plotted over the time the model was in the tunnel flow and Ne-seeded N2 cooling gas was being ejected from its tip. The ratio of the 20/40 masses was proportional to the mixing ratio according to the mass spectral sensitivity calibrations for Ne (20) and

Ar (40) and the concentration of Ne and Ar determined on separate calibration mixtures. The Ne was a specific quantitative indicator of the cooling N_2 ; since it did not occur in the tunnel air, it occurred in the boundary layer only by mixing of the cooling N_2 with the tunnel air. Similarly, the Ar was a specific quantitative indicator of the tunnel air since it was not present in the coolant gas and was diluted in the boundary layer by the addition of N_2 .

The experimental results were of limited quantitative significance because samples were obtained from only a single point and there were instrument problems affecting the Ne sensitivity. However, these results nevertheless demonstrate the feasibility of the technique, since the measured Ne and Ar displayed the proper change trends with changing conditions in the tunnel tests. The method, when incorporated in future film cooling experiments, will be of much use in directly measuring, analyzing, and interpreting the data.

Beverly W. Lewis, 2466



Measurements of mixing ratio of film cooling nitrogen to tunnel gas.

Acoustic Radiation Stress in Solids

Assessment of the stress state of materials, including external loads and residual stresses, is a problem of great complexity in the nondestructive evaluation of materials. One of the most successful techniques for measuring bulk stresses has been NASA Langley's IR-100 award-winning bolt monitor, which tracks changes in the stress state by measuring accompanying changes in the velocity of

high-frequency acoustic waves (ultrasound) propagating through the material. A comprehensive theoretical investigation performed at Langley of the nonlinear interaction between the ultrasonic wave and the stress state of the material has lead to a significant breakthrough in the understanding of acoustic radiation stress in solids.

The concept of acoustic radiation stress has been one of the most controversial and persistent problems in the field of acoustics. The new theory, generalized to anisotropic solids, is based on the application of the Boltzmann-Ehrenfest Principle of Adiabatic Invariance to a self-constrained system, represented by the nonlinear acoustic-wave equation. The results show that the acoustic radiation stress is a purely nonlinear phenomenon characterized by the product of a structurally dependent nonlinearity parameter and the acoustic wave energy density. For acoustically isotropic materials, the structurally dependent nonlinearity parameter is found to be identical to the calibration constant used in the bolt monitor, and also appears as a fundamental constant in the Gruneisen equation of state of solids. The results provide a significant contribution to the fundamental understanding of acoustic interactions with solids which is necessary for developing technology leading to absolute measurements of stresses in materials.

John H. Cantrell, Jr., 3036

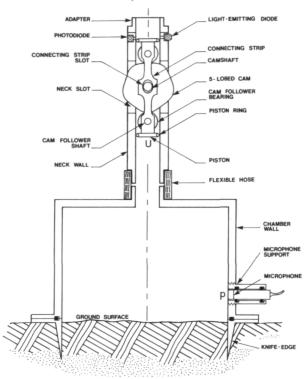
Acoustic Ground Impedance Meter

A Helmholtz resonator is used in a compact, portable meter developed at NASA Langley to measure the acoustic impedance of the ground or other surfaces. The Earth's surface is the subject of increasing acoustical investigations because of its importance in aircraft noise prediction and measurement. The resonator, which is constructed of heavy-walled stainless steel but open at the bottom, is positioned over a surface having unknown impedance. The sound source, a cam-driven piston of known stroke and thus known volume velocity, is located in the resonator neck. The cam speed is variable up to a maximum of 3600 RPM.

The sound pressure at the test surface is measured by a microphone mounted flush with the wall of the chamber. An optical monitor of the piston displacement permits measurement of the phase angle between the volume velocity and the sound pressure, from which the real and imaginary parts of the impedance are evaluated. Measurements using a five-lobed cam can be made up to 300 Hz with the acoustic ground-impedance meter. Its advantages are that it is

compact and portable and can be set up at any test site, irrespective of landscape features, weather, or other environmental conditions. Its speed of operation makes it well suited for use in conjunction with other acoustic measurements, such as aircraft noise measurements, and its operation is simple.

Allan J. Zuckerwar, 3446



Acoustic ground impedance meter.

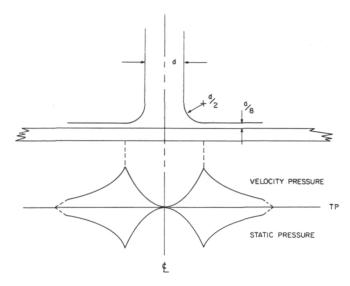
Noncontacting Suction Force Generator

A nonintrusive, nondestructive testing device has been developed at NASA Langley to meet the need for a device or technique to determine the integrity of the Shuttle tile-to-substrate bond. The device operates on the Bernoulli principle, which states that in a given region with no significant loss mechanisms and constant total pressure, a high-velocity pressure creates a negative static pressure, which causes a net suction force.

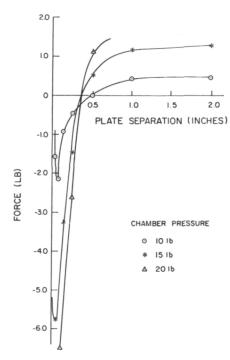
The device consists of a tubular accumulator connected to a large pneumatic valve, the output of which is close-coupled to a radial diffuser. By bringing the diffuser in close proximity to a flat or suitably shaped surface and discharging the accumulator quickly through the valve, an impulsive suction force is generated. Controlling the accumulator volume and pressure, diffused diameter, and surface separation allows a variety of forces to be generated. The

figure shows the results obtained from one device configuration. This device received the prestigious IR-100 award as one of the most significant technical products of 1983.

Harlan K. Holmes, 3446



Force versus plate separation for 3.5-in. flange.



Schematic of noncontacting suction force generator.

Space Directorate

The Space Directorate conducts research in atmospheric and Earth sciences, identifies and develops technology for advanced transportation systems, conducts research in energy conversion techniques for space applications, and provides the focal point for development activities for both large antenna systems technology and Space Station activities.

The Space Directorate is a leader in the area of atmospheric sciences. Its scientists are involved in seeking a more detailed understanding of the origins, distributions, chemistry, and transport mechanisms governing the regional and global distributions of tropospheric and stratospheric gases and aerosols, and in the study of the Earth radiation budget and its effect on climate processes. The research seeks to better understand both natural and anthropogenic processes. The research conducted in the Atmospheric Sciences Division covers a wide spectrum of activities, including the development of theoretical and empirical models; collection of experimental data from in situ and remote sensing instruments designed, developed, and fabricated at NASA Langley; organization of extended field experiments; and development of data management systems for the efficient processing and interpretation of data derived from airborne and satellite instruments.

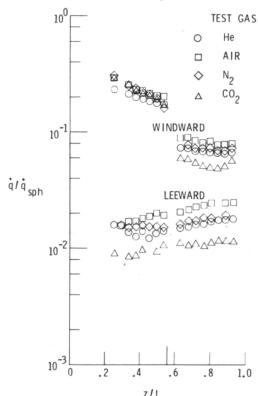
The Space Systems Division conducts research and systems analysis of advanced transportation systems, large antenna systems, and space station concepts as well as basic research into energy conversion techniques for potential space application. The Space Systems Division is a leader in the development of highly interactive and user-friendly computeraided design (CAD) tools that enable the rapid evaluation of system concepts and the identification of high-leverage technology necessary for the development of space transportation systems, large antenna systems, and the orbiting Space Station. The evaluation of advanced space transportation systems covers a wide range of capability, including Earth-to-orbit vehicles, orbit-on-demand launches, service vehicles, and orbital transfer vehicles.

Involvement in Space Shuttle flight data and trajectory analysis is an ongoing activity that seeks improvements to increase the efficiency and cost effectiveness of the Space Shuttle. Development of orbiter experiments that utilize the Shuttle as a reentry research vehicle to study radiative heat transfer and flow field chemical kinetics and to determine the aerothermodynamic and aerodynamic characteristics of the Shuttle has been a key activity and one which will lead to the development of advanced vehicle systems.

Heat Transfer Distributions for Biconics at Incidence in Hypersonic-Hypervelocity Real-Gas Flows

Laminar heat transfer distributions were measured on spherically blunted, $13^{\circ}/7^{\circ}$ straight and bent biconics at hypersonic-hypervelocity flow conditions in the Langley Expansion Tube. Free-stream velocities from 4.5 to 6.9 km/sec and Mach numbers from 6 to 9 were generated using helium, nitrogen, air, and carbon dioxide test gases. Angle of attack, referenced to the axis of the aft cone, was varied from 0° to 20° . The penalty in windward heating to the fore cone due to the 7° nose bend diminished rapidly with increasing angle of attack and was only 10 to 20 percent at the design trim angle of attack of 20° ; this nose bend caused a decrease in windward heating to the aft cone.

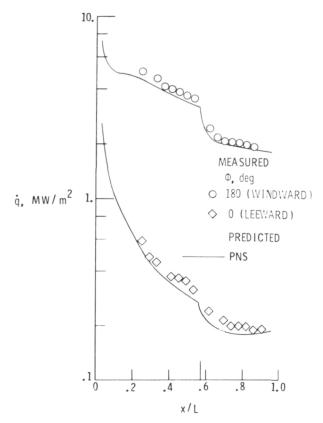
Leeward heating initially decreased, then increased, with increasing angle of attack. This trend is attributed to flow separation and the formation of vortices on the leeward side when the fore-cone angle of attack exceeds the fore-cone half angle. Windward heating rates predicted with a computer code that solves the parabolized Navier-Stokes equations were in good agreement with measurement for helium, which behaved as an ideal gas, and air, which was



Heating distribution for bent biconic in various test gases. $\alpha = 12^{\circ}$.

highly dissociated. This agreement deteriorated on the leeward side with increasing angle of attack.

Charles G. Miller, III, 4328



Comparison of measured heating to parabolized Navier-Stokes (PNS) prediction for straight biconic in helium. $\alpha = 12^{\circ}$.

Calculation of Radiation Effects Produced by Cosmic Rays Interacting With Matter

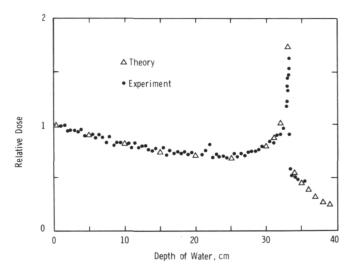
With the advent of the Space Transportation System and the anticipated development of a permanent manned presence in space, exposure to large fluences of high-energy galactic cosmic rays (HZE particles) is anticipated. In order to describe the radiation fields caused by these particles and to assess their effects on spacecraft inhabitants and materials, an accurate method for predicting nuclear fragmentation and propagation in an arbitrary material is required. To meet this need, an HZE transport theory, based upon an approximate analytical solution to the one-dimensional Boltzmann equation, has been developed at NASA Langley.

The theory allows for the calculation of radiation fluence, isotopic composition, and energy deposition

(absorbed dose) due to the incident beam and the secondary and tertiary nuclear reaction products as a function of depth in the absorbing material. The theory is valid over a wide energy range, can be applied to any arbitrary sequence of absorbing layers of uniform composition, and is easily extended to include additional interaction generations. The figure shows the excellent agreement between predicted and measured dose from 13.4 GeV neon ions in water as a function of depth.

The theory gives results that will be useful in a broad range of studies, including spacecraft environmental modelling, radiation damage in materials, spacecraft shield design and weight optimization, evaluation of astronaut and equipment self-shielding factors, and dosimetry and biological effects studies.

John W. Wilson, 3781



Theory and experiment for neon ion radiation dose.

Infrared Spectroscopic Measurements of Atmospheric Composition

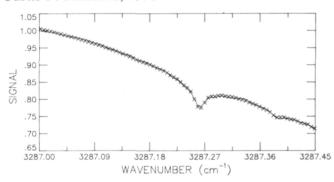
High-resolution infrared solar absorption spectra recorded with ground-based and balloon-borne interferometers can yield a wealth of information on the composition of the Earth's atmosphere. Over the past year, such spectra have been analyzed to derive vertical profiles of several molecular species of current atmospheric interest.

A number of lines of hydrogen cyanide (HCN) were detected in spectra recorded near sunrise and sunset at Kitt Peak National Observatory (latitude 31°57'N, altitude 2095 m). The figure compares a measured spectrum (solid line) and a calculated spectrum (crosses) in the region of the HCN line at

3287.248 cm⁻¹. Although HCN had been measured in the stratosphere, its concentration in the nonurban troposphere had not been determined previously. An áverage value of 166 parts per trillion by volume was derived for the 2- to 12-km-altitude range from the data.

Retrievals of the stratospheric gas concentration profiles of nitric oxide (NO) from spectra recorded at sunrise and sunset are complicated by rapid changes at twilight which cause the NO concentration to be a function of solar zenith angle as well as altitude. An iterative retrieval/model calculation approach has been developed at NASA Langley which incorporates diurnal photochemical considerations into the analysis. In collaboration with the University of Denver, a vertical profile of NO at sunset has been derived from balloon-borne solar absorption spectra. The same set of stratospheric spectra have also been analyzed to derive vertical HDO, H₂O, and CH₄ profiles. The changes in the observed concentrations of these three gases are close to those expected if stratospheric water vapor results from both CH₄ oxidation and water vapor transported across the tropopause.

Curtis P. Rinsland, 2576

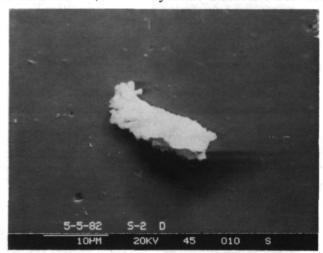


Measured and calculated spectrum near HCN line.

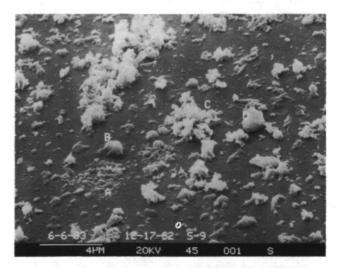
Aerosols in the El Chichon Stratospheric Cloud

Measurements were made in the El Chichon eruption cloud during the period from mid-April to mid-December 1982. Aerosol size distributions (mass loading versus particle aerodynamic diameter) were measured in situ using a quartz crystal microbalance (QCM) cascade impactor flown aboard a U-2 research aircraft up to about 21 km altitude. Data on the chemical composition and morphology of the size-segregated aerosol particles were obtained from postflight analyses with scanning electron microscopy, energy-dispersive X-ray analysis, and Auger spectroscopy.

The particles ranged in size from smaller than 0.05 µm to larger than 20 µm in diameter and were quite complex in composition and size. Certain distinct types of material tended to be separated into three size bands. Lithic and magmatic particles larger than about 3 µm in diameter accounted for about 60 to 80 percent of the aerosol mass between April and July 1982. These large particles consist of varying combinations of A1, C1, Ti, K, S, Si, Mg, Ca, and Fe (see figure). The size band between about 1 and 3.0 um consisted mainly of smaller fragments of the larger ash particles, usually coated with sulfuric acid. The liquid acid droplets (H_2SO_4), which are usually associated with volcanic eruptions, covered a relatively narrow size band ranging from about 0.08 µm to about 0.45 um aerodynamic diameter. Between



SEM imagery of a typical large volcanic ash particle collected by the QCM in the El Chichon eruption cloud on 5/5/82.



SEM imagery of material collected by the QCM in impactor stage 9 (50 percent impaction efficiency at 0.04 µm aerodynamic size) on 12/17/82.

July and December, the amount of material in the large size band (greater than 3.0 µm) decreased substantially, suggesting that the large particles were sedimenting out. During the same time period, large amounts of carbon-rich particles appeared in the small size band (0.1 µm), as shown in the figure. This could have been caused by an intrusion of nonmagmatic material of undetermined origin. X-ray energy spectra show weak traces of Mg and A1 in particles A and D, and traces of Zn and Cu in particle B. These results should be useful in determining the radiative properties of the aerosols and in assessing the climatic effects of volcanic eruptions.

David C. Woods, 2065

Calculations of Atmospheric Refraction for Spacecraft Remote-Sensing Applications

In the remote sensing of the atmosphere using a spaceborne occultation technique, a detailed understanding of ray trajectories along slant paths through the atmosphere is required to determine accurately the experimental geometry, the optical thickness of the curved atmosphere, and the associated airmass. Conventional computational techniques such as the ray trace method or the numerical integration scheme are either too time consuming or difficult to implement. A rapid and accurate method for the calculation of atmospheric refraction parameters is needed to process the large body of satellite data.

Analytical solutions to the refraction integrals appropriate for ray trajectories along slant paths through the atmosphere have been derived at NASA Langley. The solutions are obtained by evaluating higher-order terms from the expansion of the refraction integral and are dependent on the vertical temperature distributions. Refraction parameters such as total refraction angles, air masses, and path lengths can be accurately computed. It has also been shown that this method can be used for computing refraction parameters in astronomical refraction geometry for large zenith angles.

This method has been implemented in the computer algorithm for the processing of SAM II and SAGE satellite measurements. Four years of SAM II and 3 years of SAGE data have been processed and archived, providing near-global distribution of aerosol, ozone, and NO₂ data.

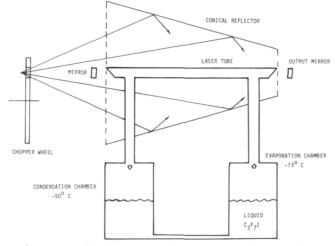
William P. Chu, 2065

Solar-Pumped Continuously Pulsed Laser

Lasers that are directly powered by sunlight offer several advantages over other types of lasers (electrically pumped, nuclear pumped, and chemically pumped) especially for space-based applications where the abundant energy of the Sun is not filtered by the atmosphere. These lasers convert solar energy directly to laser energy without intermediate conversion steps such as converting the solar energy to electricity. Solar-pumped lasers would be cleaner, lighter, and cheaper to build than other lasers. Their potential uses include power beaming in space, laser propulsion for spacecraft, and deep-space communications.

An iodine laser being investigated for space power applications uses a conical reflector to concentrate the light from a solar simulator onto a glass tube through which an iodide gas is flowing. Flow is maintained by an evaporation-condensation cycle in which liquid C₃F₇I at -15°C evaporates, flows through the laser tube, condenses in a glass chamber cooled to -50°C, then flows back to the initial chamber to be recycled. While flowing through the laser tube, the gas is dissociated and its iodine component is excited by the light. Lasing occurs at a wavelength of 1.3 µm. A chopper wheel between the solar simulator and the laser regulates the frequency and duration of the light pulses that illuminate the laser tube. This solar-simulator pumped iodine laser has recently been operated in the continuously pulsed mode for periods exceeding 5 minutes. Between pulses, new gas enters the laser tube. The used gas undergoes recombination to reconstitute itself while being recycled. Pulse rates of 5, 10, and 20 Hz have been used with a duty cycle of 17 percent.

Donald H. Humes, 3781



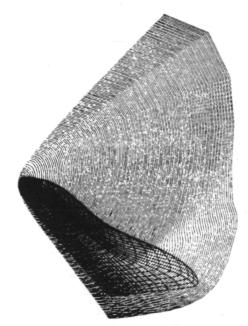
Schematic of solar-pumped continuously pulsed laser.

High-Angle-of-Attack Inviscid Flow Calculations Over a Shuttle-Like Vehicle With Comparisons to Flight Data

A three-dimensional inviscid flow field code (HALIS) developed at NASA Langley has been run for a nearly complete Shuttle vehicle for Mach numbers between 6.0 and 21.6 and angles of attack between 26.6° and 40°. Both perfect-gas gamma (γ) and effective gamma (γ) HALIS solutions have been compared with four points along the STS-3 reentry trajectory and two points on the STS-5 reentry trajectory. In general, the HALIS results have agreed very well with the flight data. At high Mach numbers, the excellent agreement of flight data and effective gamma flow field solutions shows that gamma effects have a significant effect on the windward surface pressure distributions on the Shuttle wing.

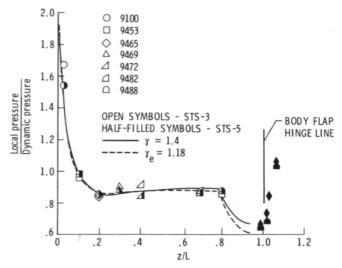
HALIS solutions also indicate that centerline pressure distributions at the aft end of the Shuttle vehicle are altered by gamma effects. A comparison of flight data and computed solutions in this region was inconclusive due to a lack of flight data density and flight-to-flight data scatter. In addition, HALIS results have been used to illustrate the effect of Mach number and angle of attack on the large-scale shock structure about the Shuttle vehicle as well as to provide a detailed view of the interaction region between the bow shock and the wing shock.

K. James Weilmuenster, 3271



LOWER SURFACE

HALIS external shock structure for $M_{\infty} = 6.0$, $|\alpha| = 26.6$, $|\gamma| = 1.4$.



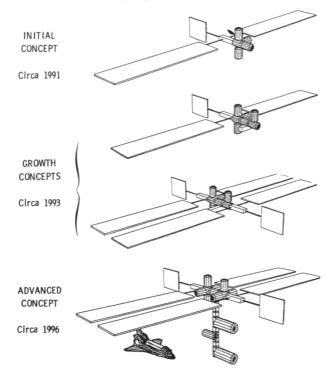
Comparison of HALIS and flight centerline pressures; $M_{\infty} = 21.6$, $\alpha = 40^{\circ}$ for $\gamma = 1.4$ and $\gamma_e = 1.18$.

Space Station System Synthesis

During the conceptual development of a space station system, many compromises must be considered to balance economy, performance, and levels of technology of the total system. Subsystem tradeoffs need to be made in order to satisfy system sensitive multidisciplinary attributes. Due to the complex nature of potential space station systems, these trade studies have become more difficult and time consuming to complete, and they involve interactions of ever-larger numbers of subsystems, components, and performance parameters. The current advances of computer-aided synthesis, modeling, and analysis have greatly helped in the evaluation of competing design concepts.

The IDEAS and AVID computer-aided design systems for advanced aerospace systems were described in the NASA Langley 1982 Research and Technology Annual Report. The IDEAS system is being augmented with a space station system analysis capability. The methodology behind this analysis capability consists of identifying and mathematically modeling both state-of-the-art and technologically advanced subsystem configurations, integrating these subsystems into a total system configuration, performing rapid systems analyses, and integrating the above steps into a computer-aided design system. Through the use of new techniques of solid modeling, finite-element analyses, subsystem synthesis, and data base management, generic space station configuration system concepts are being synthesized and analyzed to assess subsystem and systems performance improvements that result from the incorporation of advanced disciplinary technology improvements. Evolutionary station concepts are presently being synthesized to model time-phased capabilities to determine subsystem performance levels and resource requirement sensitivities to build up sequences for each configuration.

Melvin J. Ferebee, Jr., 3666



Concept build-up sequence.

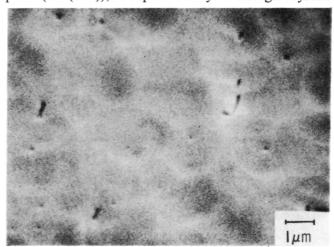
High-Quality Thin-Film Germanium Single Crystals

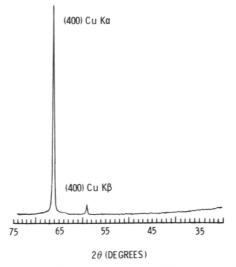
The demand for the development of large solar cell arrays for space applications has stimulated a great interest in thin-film photovoltaics, primarily because of their projected high power-to-weight ratio. A promising approach to developing this type of solar cell is to grow high-efficiency photovoltaic thin cells by vapor deposition techniques onto appropriate thin-film substrate crystals. Since gallium arsenide (GaAs) solar cells have exhibited the highest power conversion efficiencies and superior radiation resistance, especially under continuous annealing conditions, such cells in thin film form offered attractive advantages.

Germanium (Ge) has very similar crystallographic characteristics (e.g., approximately the same lattice constant and a similar crystal structure) to GaAs. It tends to be a very compatible substrate for

growth of GaAs films. Further, since efficient cells had been grown on thick Ge single crystals, Ge appeared to be an excellent substrate candidate for the thin-film cells. What was required was a single-crystal Ge thin film. Working with United Technology Research Center, NASA Langley researchers have developed a method for growing high-quality 10-µm Ge films on NaC1 substrates by a specialized vapor deposition technique and then separating these Ge films from the salt. The free-standing films then can be used for the growth of GaAs cells by well-known methods.

Previous experiments have shown that the efficiency of the resulting cells is highly sensitive to the surface topography and crystalline perfection of the Ge films. The figure shows an electron micrograph of a typical growth surface topography for a $10-\mu$ m Ge film. Visually, these films are mirror smooth. As shown in the graph, the major X-ray diffraction peak from the Ge film is from a single crystallographic plane (the (400)), as expected only for a single crystal.





Surface topography for 10- μ m Ge film. X-ray diffraction peak from Ge film.

The source of characteristic X radiation (Cu $K\alpha$ and Cu $K\beta$) is a copper target. The intensity of this diffracted peak indicated a high degree of crystalline perfection. Electron and X-ray spectroscopy yielded pure Ge spectra with no detectable bulk contamination. Thus the techniques necessary for the high-quality Ge thin-film crystals required for growth of efficient thin-film GaAs solar cells or other applications are now available.

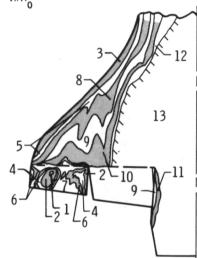
R. A. Outlaw, 3781

Heat Transfer on Space Shuttle Orbiter Models With Differentially Deflected Elevons

The phase-change paint technique was used to make heat transfer measurements on Space Shuttle orbiter models with differentially deflected elevons. The outboard elevons were deflected windward through an angle δ when the inboard elevons were deflected through an angle -2δ , where $\delta=0^{\circ},5^{\circ},10^{\circ},15^{\circ}$, and 20° . The models were tested in air at Mach 6 and Mach 10 with two different flow conditions at each Mach number. Each test was run at three angles of attack: $20^{\circ},28^{\circ}$, and 35° . This study was restricted to the windward side of the wingelevons area.

The highest heating always occurs on the wing leading edge and at the inboard edge of the outboard windward-deflected elevon. Geometric patterns of heating on the wing and windward-deflected elevons are often complex, particularly at 20° and 28° angles of attack. Multiple chordwise streaks of higher heating often occur across the wing and sometimes extend to spots of highly localized heating on the windward-deflected elevon. In general, deflection of the elevons does not strongly alter these heating patterns on the wing. High heating near the leading edge of the wing is extended farther aft on the wing by the "streak" phenomenon. In most cases, deflection of the elevons does not change the maximum heat transfer coefficient anywhere on the wing by more than 40 percent of the values obtained when the elevons are undeflected at the same test condition and angle of attack. However, the maximum heat transfer coefficient on the windward-deflected elevon is a strong function of the deflection angle. For example, when data obtained in these tests were averaged over both test conditions and all angles of attack at each Mach number, the maximum heat transfer coefficient on the 15° deflected elevon was approximately 3 times the value obtained on the undeflected elevon. Furthermore, multiplying factors for the coefficient between the undeflected and 20° deflected elevon were 4 at Mach 10 and 22 at Mach 6.

William L. Wells, 3031



Heat transfer coefficient patterns on the orbiter wing and elevons at M = 10, $\delta = 15^{\circ}$, and $\alpha = 28^{\circ}$.

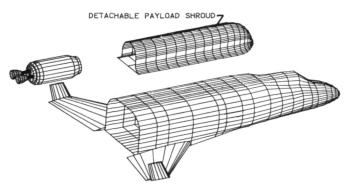
Future Space Transportation Systems Study

To aid in the establishment of a technology base for the next generation of space transportation systems (2005), the Future Space Transportation Systems Study (FSTS) has been conducted to identify benefits from technology improvements in terms of performance and cost. The FSTS study, begun in October 1981, is intended to define a launch vehicle concept that improves space transportation capabilities and economics and to project technology requirements beyond previous studies, especially in the areas of structures, propellant tankage, thermal protection, aerothermodynamics, and operations.

The FSTS study centered on development of a configuration that could be used to assess staging and operations and to analyze thermostructure design concepts. By applying advanced technology in structures, materials, and propulsion, a fully reusable two-stage system has been analyzed. This system has the estimated capability to deliver 150,000 pounds of payload, more than twice the payload of the Space Shuttle, for only a slight increase in vehicle size and weight.

The orbiter design chosen uses a "flatbed truck" approach with replaceable shrouds either covering the payload or integral to it to permit the carrying of various payload shapes. A novel "aeroshell design" allows access to all structural components and cryogenic tankage for repair and replacement. Advanced carbon-carbon "hot" structures, manufactured as large panels, reduce servicing costs. Built-in test equipment, fault isolation, and fully accessible components were incorporated in the design to provide an exceptionally flexible system concept.

Delma C. Freeman, Jr., 3911



Future Space Transportation System.

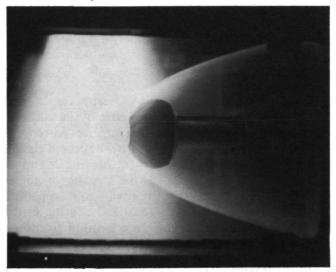
Hypersonic Flow Characteristics of Aero-Assisted Orbital Transfer Vehicles

Past experimental studies at Mach 20 of an aerobraking orbital transfer vehicle using an inflatable ballute to produce high drag indicated that the predicted flow fields necessary for the vehicle to perform properly could be produced. Sufficient cooling to protect the ballute from entry heating is produced by mass addition provided either by firing the main engine forward or allowing cryogenic fuel to escape through the engine and mix with the natural boundary layer of the vehicle. Varying stagnation point mass addition in this manner produces unusual shock wave structures, including normal blunt body shock shapes, highly unstable shock fronts, and stable double shock structures. These past studies

used solid-body representations of the expected shape of the inflated ballute to verify predicted flow fields and drag levels. The problem of how to study flexible body response to these unusual and sometimes unsteady shock jet flow field interactions remained a concern.

Goodyear Aerospace and the Boeing Company fabricated a wind tunnel model from cotton cord and neoprene rubber for testing at Mach 20 in the Langley Hypersonic Helium Tunnel to determine how such a structure would respond at wind tunnel conditions. The photograph shows the shock structure on the flexible model illuminated by an electron beam flow visualization device. Shock structure and drag levels were quite similar to those experienced by the solid model. For no mass addition and low levels of mass addition, ballute deformation occurred, but a fixed shape rather than a divergent oscillation resulted. The flexible forebody did not appear to adversely effect the stability of the flow field, and vice versa. This was not a dynamic simulation of a flight article but a test to produce the necessary database to analyze and develop flight articles.

W. C. Woods, 2483



Shock structure on flexible model.

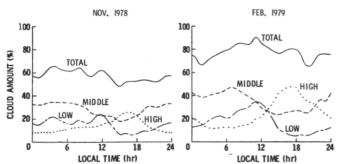
Diurnal Cloud Variations

The diurnal cycles of cloud cover and radiation are not parameterized in many operational numerical weather and climate prediction schemes, even though the daily solar cycle dictates that 24 hours is an important meteorological time scale. At present, the diurnal cycles of clouds and radiative energetics within the atmosphere are poorly understood. To learn more about clouds and radiation at this time

scale, an hourly high-resolution visible and infrared data set from the Geostationary Operational Environmental Satellite (GOES) is being analyzed to quantify both the regional-scale diurnal variations in total cloudiness and low, middle, and high clouds and the cloud and clear-sky radiative properties for part of the Western Hemisphere over several seasons.

A plot of the mean cloud cover for November 1978 and February 1979 for a region in the Amazon River Basin demonstrates the type of results found with this analysis. Here, a quite regular, deep, convective diurnal cycle is apparent during both months, although the total cloudiness is 20 percent less in November. The buildup of low-level cumulus clouds in the morning is followed by towering thunderstorms (high clouds) in the afternoon. During the night, thin cirrus and altocumulus are the predominant cloud types. These diurnal cloud variations are typical of tropical South America. Other large areas with significant monthly mean diurnal cloud changes include the zone of intertropical convergence and the southeastern Pacific. Occasional warming of the sea surface in the latter region (known as the El Niño) has been associated with certain extreme weather events over many parts of the Earth. Coherent variations in cloudiness over these areas suggest diurnally dependent features of the largescale circulation. Results of this continuing study will aid the formulation and verification of diurnal cycles in predictive models.

Patrick Minnis, 2977



Regional (250 × 250 km²) cloudiness at 5.6° S, 60° W.

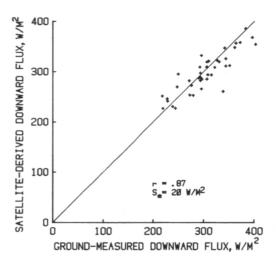
Earth Surface Radiation Studies

Earth surface radiation is important to the understanding of weather and climate. Regional surface radiation balance greatly affects surface temperature, energy exchanges between the atmosphere and land-sea surfaces, and consequently the atmospheric and oceanic circulations. Researchers at NASA Langley have now developed remote tech-

niques for determining the amounts of solar and longwave radiation received at the surface using meteorological data available from satellites. Satellite methods for deriving the Earth's radiation budget have been studied for some time, but these determinations generally have been carried out with top-of-the-atmosphere measurements, which include atmospheric effects. Recently, a strong interest has developed for remote determination of radiation budget information at the Earth's surface. The new longwave technique is a significant first for deriving downward longwave flux from global satellite data.

The solar radiation technique is also unique because it relies mainly on meteorological data from operational satellites instead of surface observations or just climatology. These techniques have been validated by comparing their results with groundbased radiometer measurements at several sites for periods of 4 to 5 weeks. A scatter diagram of groundmeasured and satellite-derived downward longwave fluxes yielded a correlation coefficient of 0.87 and a standard error of 20 W/m². These results adequately meet the basic accuracy requirements for surface radiation data and compare well with accuracies achieved by other investigators. Studies for further validation of these techniques at more sites and longer time periods and extensions to regional and global scales are continuing.

Wayne L. Darnell, 2977



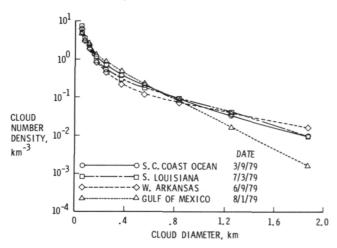
Comparison of ground-measured and satellitederived downward fluxes.

Landsat-Derived Cloud Populations

Intensified research into the climatic effects of the Earth's cloudiness has driven an increased need for detailed information on cloud properties. New information is especially needed for cumulus and cirrus clouds. In order to provide improved data on cumulus cloud fields, Landsat Multispectral Scanner (MSS) data have been analyzed to provide cloud number densities, cloud cover, and horizontal cloud aspect ratios as a function of cloud size. Cloud properties are determined for clouds ranging in size from 150 m to 100 km in diameter. This range represents an order-of-magnitude improvement over the cloud sizes resolvable from meteorological satellites.

Results for cloud number density (number of clouds per 100-km square area per 1-km cloud size interval) as a function of cloud diameter are shown in the figure for four Landsat scenes of fair-weather cumulus. Approximately 20,000 clouds were analyzed in each scene. The cloud number density distributions support earlier indications that cloud number decreases exponentially with increasing size. In addition, the slope of the decrease is found to be proportional to total cloud fraction in the scene. Although the Landsat satellite sensors were designed to study features of the Earth's surface, they have been shown to provide important information about the Earth's cloud cover as well.

Bruce A. Wielicki, 2977



Cloud number density as a function of effective cloud diameter from four Landsat scenes.

Analysis Method for Fourier Transform Spectroscopy

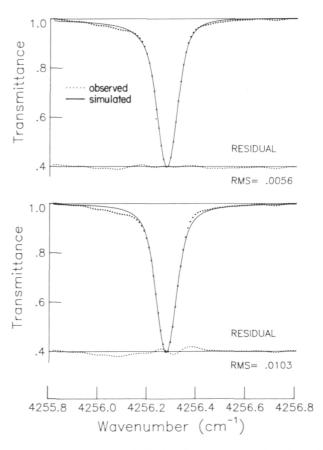
In the analysis of an interferometric spectrum, an accurate knowledge of instrument line shape is required. The instrument line shape of the interferometric spectrum can be distorted due to errors in the measured interferogram. A fast Fourier transform

technique for simulating the distortion effects has been developed, and the technique has been applied to the analysis of atmospheric absorption and laboratory spectra. It has been shown that correct information can be retrieved from the distorted spectra using the nonlinear least-squares method.

Shown in the figure are a measured absorption spectrum (dotted line) of the hydrogen fluoride (HF) R8 line obtained by an interferometer and the simulated spectrum (solid line) using the current technique. The differences between the measured and simulated spectra are shown at the 0.4 transmittance level. The simulated spectrum without this technique is also shown. In this case the retrieved HF gas mixing ratio was found to be 30 percent off from the average value of 2 years data. Note the large distortion in the residual spectrum.

It has been shown that this technique can retrieve gas mixing ratios from interferometric spectra with an accuracy of 3 percent error for laboratory spectra (e.g., HALOE (Halogen Occultation Experiment) gas cells), and of 7 percent error for more noisy balloon-borne spectra.

Jae H. Park, 2576

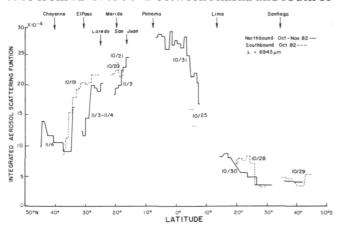


Absorption spectra of HF R8 line with (top) and without (bottom) current analysis technique.

Satellite and Lidar Measurements of El Chichon Stratospheric Cloud

The stratospheric aerosol background of 1978-1979 has been disturbed by a number of recent volcanic eruptions that have produced a cumulative effect on the stratosphere. The largest was produced by the March-April 1982 eruptions of El Chichon (17.3°N, 93.2°W) and was probably the largest perturbation to the stratosphere in at least the last 70 years. Since this background period, peak aerosol ruby laser scattering ratios at NASA Langley (37°N, 76° W) have increased by as much as a factor of 300, and integrated scattering by as much as a factor of 70. Likewise, the SAM II satellite sensor aboard Nimbus 7, which measures vertical profiles of stratospheric aerosol extinction in the polar regions, has observed similar enhancements. In December 1982, 8 months after the eruption, SAM II measured Arctic extinction values almost 2 orders of magnitude greater than the 1978 values and optical depths of up to 0.10 at λ = $1 \mu m$.

In order to better understand the latitudinal distribution of stratospheric material with time, a number of aircraft expeditions were carried out in coordination with balloon and satellite measurements. These expeditions utilized the Langley uplooking aerosol lidar system aboard various aircraft and, in most cases, sun photometers and diffuse-flux measuring instruments. Expeditions were carried out in July 1982 from 42°N to 12°N between New York and the northern coast of Venezuela, in October-November 1982 between 46°N and 46°S from Virginia to Chile and returning through Wyoming and North Dakota, in January-February 1983 from 27°N to 76°N between Miami and Greenland, and in May 1983 from 72°N to 56°S between Alaska and south of



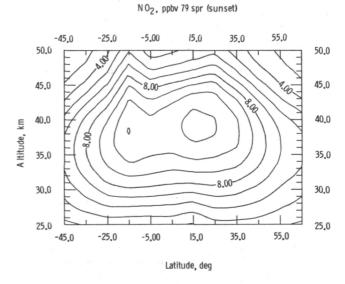
Integrated aerosol scattering function versus latitude derived from airborne lidar data taken in October-November 1982 between the northern United States and southern Chile.

New Zealand. These experiments showed that subtle atmospheric dynamics limited the northern edge of the most optically thick material to be at approximately 30°N in July 1982, 35°N in October 1982, and 55°N in January and May 1983. Material below 20 km arrived in the Arctic by the end of April 1982 and in the Antarctic by at least December 1982. The southern edge in October 1982 was between 6°S and 10°S. An example of the latitudinal distribution of this material in October-November 1982 is shown in the figure. These newly acquired data from such a strong atmospheric perturbation as was caused by El Chichon present a unique opportunity for studying and improving climate and transport models.

M. P. McCormick, 2065

Satellite Observations of Stratospheric NO₂ by SAGE

Observations of attenuated solar radiation in the visible spectral region (0.385 to 0.45 μ m) from the orbiting satellite instrument SAGE for the period February 1979 to February 1980 have been used to determine the near-global distribution of nitrogen dioxide in the middle to upper stratosphere. The SAGE instrument is a four-channel sunphotometer aboard the Application Explorer Mission II satellite (AEM II) to perform solar occulation measurements of stratospheric aerosol and gases. The four spectral channels are located at wavelengths of 1.0, 0.6, 0.45, and 0.385 μ m. The 1.0- μ m channel is for aerosol extinction measurements, the 0.6- μ m channel is located at the peak of ozone Chappius absorption band



SAGE NO2 measurements, March-May 1979.

for ozone measurements, and the 0.45- μm and 0.385- μm channels are for NO_2 and aerosol shortwavelength extinction measurements.

The SAGE-observed NO₂ vertical profiles have been compared to previous balloon-borne measurements, showing good agreement. The SAGE sunrise and sunset observations of NO₂ vertical distribution have shown variations as predicted from photochemical calculations. Zonal mean latitude versus height distribution of NO₂ mixing ratio for the spring of 1979 is shown in the figure. Seasonal variations of the zonal mean distribution of NO₂ have been observed with strong latitudinal and longitudinal variations in NO₂ column density during the winter season at high latitudes.

William P. Chu, 2065

Stratospheric Aerosol Climatology in Polar Regions As Observed by SAM II

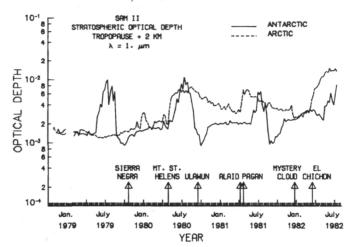
The SAM II experiment was launched aboard the Nimbus 7 spacecraft in October 1978, and since then it has been making vertical profile measurements of stratospheric aerosols during each spacecraft sunrise and sunset. The Nimbus 7 orbit constrains these measurements to the polar regions between 64° and 82° latitude; spacecraft sunrises are in the Antarctic and sunsets in the Arctic. These measurements are providing, for the first time, a polar aerosol climatology that is showing the spatial and temporal variability of this stratospheric species. The period 1978-1979 appeared to be a period of background aerosol with values of stratospheric optical depths of about 0.0015 at 1 **. The longitudinal and seasonal structure is correlated well with temperature and synoptic meteorology. SAM II data have revealed that during both polar winters, polar stratospheric clouds (PSC's) are formed in regions of cold temperatures, with a 50-percent probability of occurrence for temperatures of 194 K. The PSC's increase the weekly averaged stratospheric optical depths by an order of magnitude. A cleansing of the Antarctic stratospheric aerosol is obvious after each wintertime PSC season.

Since 1979, a series of volcanic eruptions have perturbed the stratospheric aerosol in an additive manner. The time of arrival of the volcanic material in high latitudes has depended upon the location of the particular volcano and the season in which it erupted. Material from Mount St. Helens (46.2° N, 122.2° W) and Alaid (50.8° N, 155.5° E), for example, arrived in quantity within a month. Material from the equatorial Sierra Negra (0.8° S, 91.2° W) gradually

arrived over a period of 6 months. After the April 1982 eruption of El Chichon (17.33°N, 93.2°W), SAM II has observed extinction coefficients at 1 μ m as high as 3×10^{-2} km⁻¹ in the Arctic and 10^{-2} km⁻¹ in the Antarctic, with optical depths in the Arctic as high as 0.12. Weekly averaged optical depths from launch through July 1982 are shown in the figure.

The 4-year aerosol climatology being developed by the SAM II experiment clearly shows that the major perturbation to stratospheric aerosols (excluding PSC's) is of volcanic origin. Further, the eruption of El Chichon has caused a perturbation large enough to produce significant temperature changes.

M. P. McCormick, 2065



SAM II derived stratosphere optical depths versus time for the Arctic and Antarctic.

Remote and In Situ Aerosol Measurements Over the Atlantic

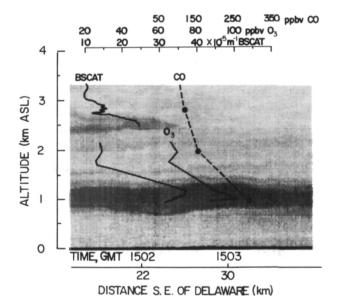
The contribution of long-range transport of continental pollutants in altering the global environment is one of the most important current issues in environmental science. To determine the characteristics of a continental air mass as it is transported over the Atlantic, a series of flight experiments were conducted between the U.S. east coast and Bermuda during the summer of 1982 as part of the NASA Global Tropospheric Instrument Test Flight (GTE-ITF) program. A nadir-viewing multiple-wavelength lidar system operating from the NASA Wallops Electra aircraft was used to provide real-time vertical distribution and backscatter information on the aerosols below the aircraft and along the flight tracks. In situ measurements of aerosol characteristics and gas concentrations were then made from the aircraft

at lower altitudes in specific layers chosen for further investigation.

On August 5, 1982, the Electra flew from Wallops Island, Virginia, to Bermuda with remote and in situ aerosol measurements made along 145 km flight tracks centered 80 km east of Lewes, Delaware. The figure shows a display of the aerosol distribution obtained by the lidar system near the coast of Delaware. Each vertical line represents a laser firing. and the display is darker in regions of increased atmospheric scattering. The top of the continental air mass is seen to extend to 2800 m above sea level (ASL). The most aerosol-laden part of the continental air mass is near 1000 m ASL. The remote and in situ measurements showed direct correlation in the vertical profiles of aerosol scattering coefficients (BSCAT): ozone (O₃) and carbon monoxide (CO); and lidar measurements of aerosol scattering. Under the proper atmospheric conditions, these types of continental air masses can be transported over long distances before deposition into the marine boundary layer.

Data from these flight experiments illustrate a new, direct approach to studies of long-range transport and fate of pollutants in the troposphere.

Edward V. Browell, 2576



Measurements of air mass over the Atlantic, Aug. 5, 1982.

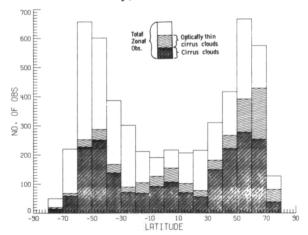
Global Distributions of Cirrus Clouds Determined From SAGE Data

An analysis using SAGE data for the period February 1979 to April 1980 was performed to

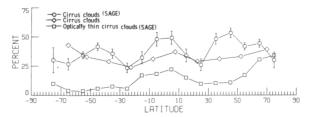
determine the spatial extent and frequency of cirrus clouds over a large portion of the Earth's surface. These results should be of interest to, among others, researchers concerned with global monitoring and modeling of the Earth's radiation budget and climate and to reentry vehicle designers concerned about anomalous aerodynamic effects or damage due to the ice particles found in cirrus clouds. A byproduct of the study reveals the statistics of tropospheric observational opportunities for a limb-sounding satellite sensor by determining the percentage of times of successful penetration to 7 km.

The figures illustrate the results of the analysis and show that cirrus clouds form most often in the midlatitudes and over the Equator, with peaks reaching the 50-percent level. Two troughs or minima at about the 25-percent level occur near the north and south 20° to 30° latitude bands, and their presence tends to corroborate theories of stratospherictropospheric exchange processes. Thin cirrus clouds occur much less frequently. A comparison of the SAGE cirrus cloud results made zonally with those obtained from ocean-surface-based observations showed general agreement. Both curves had an equatorial rise and minima near the 20° to 30° north and south latitude bands, but SAGE results show a significantly larger variation of cloud frequency with latitude. In addition, SAGE shows a midlatitude maximum (40° to 50° N and S) not evident in the ocean-surface-based data. Tropospheric observational opportunities for a limb-sounding satellite sensor, as evidenced by successful penetrations to 7 km, occurred approximately 60 percent of the time in the higher latitudes and fell to a low of 30 percent over the tropics. Because of the higher tropopause in the tropics, actual penetration in terms of depth below the tropopause may be constant with latitude.

Gerard E. Woodbury, 2065



Numerical cirrus cloud results (Feb. 1979 to Apr. 1980).



Cirrus cloud results in percent of observations (Feb. 1979 to Apr. 1980).



Tropospheric penetrations in percent of observations (Feb. 1979 to Apr. 1980).

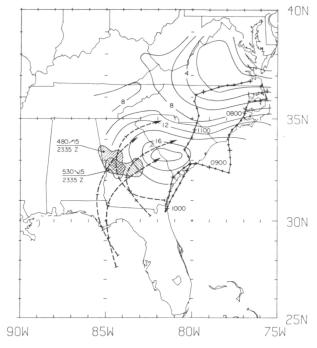
Airborne Lidar Observations of Long-Range Transport in the Free Troposphere

When used in combination with appropriate meteorological and chemical instrumentation, an airborne lidar can be used to resolve the state and dynamics of the mixed layer under complex meteorological conditions. Lidar techniques can provide the altitude distribution of aerosol and trace gas concentrations in the troposphere, and can therefore provide key information on the long-range transport of atmospheric pollutants. UV DIAL (differential absorption lidar) measurements obtained over the lower Chesapeake Bay area on July 31, 1981, show an ozone-rich aerosol layer extending from 800 m to 1600 m above sea level. An isobaric back trajectory analysis indicates that this polluted air mass was transported to the Norfolk, Virginia, area from New England over the Atlantic Ocean in less than 24 hours. Four successive overflights recorded the growth of the southeastern Virginia mixed layer as it rose up to and into this elevated haze layer. These measurements indicate that approximately 30 percent of the ozone maximum measured at the surface on July 31, 1981, in southeastern Virginia was imported from external sources greater than 500 km upstream.

The NASA UV DIAL lidar system provided information on the altitude distribution of haze observed in satellite images over the southeastern United States on August 2, 1980. An isentropic trajectory analysis indicates that this elevated layer was involved with thunderstorm activity over western

Georgia on August 1, 1980. Our calculations indicate that subsequent long-range transport (greater than 200 km) occurred over a lower level of fair-weather cumulus convective debris. Long-range transport in such elevated "reservoir" layers will go undetected by sensors that are confined to the surface. This transport process can provide long residence times without significant interaction with surface source or sink mechanisms. Since thunderstorm washout can involve all levels of the troposphere, such elevated layers may be a significant factor in acid deposition.

Scott T. Shipley, 2576



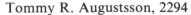
Forty-eight-hour isentropic back trajectories at 312 K for four locations within the haze area, ending at 1200 UT on August 2, 1980.

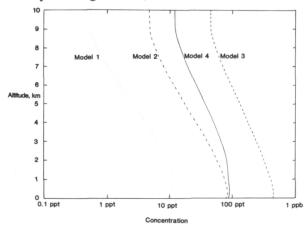
Sulfur Budget of the Troposphere

The troposphere is a region of great complexity in terms of its chemical, physical, and biological processes. In order to try to understand how these processes could potentially affect the structure and composition of the troposphere, computer simulations using numerical techniques are useful tools. A one-dimensional photochemical model of the global troposphere has been used to examine the role of sulfur species. Particular attention has been focused on the problem of how to prescribe the gridspacing and how to parameterize the eddy diffusion coefficient K_Z . Traditionally, most photochemical models of the

troposphere use a gridspacing of 1 km, and K_z is held constant at 10⁵ cm² sec⁻¹. This is called Model 1 in the present study and is represented by the dotted line in the figure. Model 2 is the case with gridspacing of 250 m in the boundary layer (the lowest 1.5 km) and gridpoints at each subsequent kilometer up to and including 10 km (the tropopause). In Model 2, the eddy diffusion coefficient is held constant at 1×10⁵ cm² sec⁻¹. Model 3 also has a constant eddy diffusion coefficient of 1×10^5 cm² sec⁻¹, but in this version the gridspacing varies logarithmically in the lowest kilometer. Above 1 km, gridpoints are located at each kilometer up to the tropopause. Model 4 has an identical gridspacing to Model 3, but in Model 4 the eddy diffusion coefficient varies as a function of altitude, with low values near the surface to simulate the surface friction.

Calculated vertical profiles are presented in the figure using sulfur dioxide (SO₂) as an example. In this example, a downward flux of 5 × 10⁷ molecules cm⁻² sec⁻¹ was used, and this resulted in surface mixing ratios of 9.5 parts per trillion by volume (pptv) for Model 1, 78 pptv (Model 2), 443 pptv (Model 3), and 86 pptv (Model 4.) It should be kept in mind that this wide range of surface concentrations results strictly as a function of how the gridpoints are prescribed and how the eddy diffusion coefficient is parameterized. These modeling results have important implications for other species that are calculated with the use of the species continuity equation.





Calculated vertical profiles of SO₂.

Sources of NO_X to the Global Troposphere

The oxides of nitrogen, NO_X (nitric oxide, NO+ nitrogen dioxide, and NO₂) are key species in the

photochemistry of the troposphere. A major uncertainty in our understanding of the composition and photochemistry of the troposphere concerns the global sources of NO_X . Researchers at NASA Langley have studied and better quantified three important sources of NO_X : atmospheric lightning, the production of NO_X from oxidation of ammonia (NH₃), and the biogenic production of NO_X .

Experiments in the Langley Lightning Facility have resulted in a new determination for the yield of NO_x by lightning of $5 \pm 2 \times 10^{16}$ molecules per joule of lightning energy. The major uncertainty in assessing the total global production of NO_X by lightning concerns our poor knowledge of the total energy deposited by lightning, which ranges from 10⁻⁸ to 10⁻⁷ J cm⁻² sec⁻¹. The lower estimate results in a global production of NO_X of about 2 million tons of nitrogen per year, and the upper value results in a value of about 20 million tons of nitrogen per year, which is comparable to the combustion source of NO_x (believed to be the dominant one in the global NO_x budget). In a related study, samples of air exposed to thunderstorm lightning obtained with the Langley Storm Hazards Project F-106B Delta Dart exhibited enhanced levels of nitrous oxide, another oxide of nitrogen formed by lightning. These measurements confirm earlier experimental results obtained at Langley and verify the validity of laboratory experiments in simulating photochemical and chemical processes initiated by lightning.

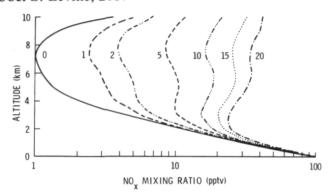
By coupling IHR (infrared heterodyne radiometer) measurements of the vertical distribution of NH3 in the troposphere with photochemical calculations, we have been able to estimate the production of NO $_{\rm X}$ due to the oxidation of NH3 by the hydroxyl radical (OH). Our calculations indicate the NH3 oxidation may supply as much as 10 million tons of NO $_{\rm X}$ per year.

Laboratory experiments indicate that nitrifying bacteria (Nitrosomonas europaea) commonly found in soil are significant biogenic sources of both NO and N₂O. Our experiments indicate that these bacteria produce NO to N₂O in a ratio of about 2 to 1. Extrapolating these laboratory results to the global scale indicates that nitrifying bacteria may produce as much as 10 to 20 million tons of NO per year.

The production of NO_X by lightning and by the oxidation of NH_3 are altitude-distributed sources. To assess the effect of these altitude-distributed sources of NO_X on the vertical distribution of NO_X in the troposphere, we have performed theoretical calculations using a one-dimensional photochemical model of the global troposphere. The vertical distributions of NO_X for six different values of the altitude-distributed source of NO_X equal to 1, 2, 5, 10, 15, and

20 million tons of nitrogen per year, as well as for no altitude-distributed source, are shown in the figure. Clearly, the addition of altitude-distributed sources of NO_X makes a significant difference in the calculated profile of NO_X .

Joel S. Levine, 2187



Effect of varying altitude-distributed source of NO_{χ} on tropospheric distribution of NO_{χ} .

Development of Interactive Aeroheating-Thermostructural Analysis Capability for AVID

One of the critical design areas for any vehicle that must pass through the hypersonic speed regime is that of the thermal protection system (TPS). Design of the TPS requires accurate analysis of the heating rate and temperature histories encountered along the trajectory, as well as the temperature response through the TPS. For preliminary design calculations, however, the requirement for accuracy must be tempered by the need for speed and versatility in the computational tools used to determine the thermal environments. Over the last decade, the MINIVER program developed at NASA Langley has been found to provide the proper balance of versatility, speed, and accuracy in an aerothermal prediction tool.

The MINIVER program has been modified for use interactively in conjunction with the AVID (Aerospace Vehicle Interactive Design) System. AVID is an integrated preliminary design system developed at NASA Langley in order to allow a designer to interact with a variety of analysis programs (including aerodynamics, propulsion, flight performance, weight, sizing, cost, etc.) and to provide a means of transferring design information from one program to another. A new Explicit Interactive Thermal Structures (EXITS) code has also been developed at Langley. This code allows the user to build his own TPS model out of the materials presently included

(including several recently developed materials) or to describe new materials. TPS options now include honeycomb, radiation gap, Z standoffs, corrugated skin, and ablators in addition to the thin skin and thick slab present in the older version. EXITS yields the temperature response through the TPS throughout the time of the trajectory as well as the unit mass of the TPS.

Thus, the user is able to design a vehicle and develop a trajectory using the AVID system, take that information and determine the heating history under those conditions, examine the response of a variety of TPS, and finally determine the corresponding mass of those systems. Ultimately, this information can be fed back into the initial design of the vehicle and its trajectory in order to further optimize the total system.

Kathryn E. Wurster, 3911

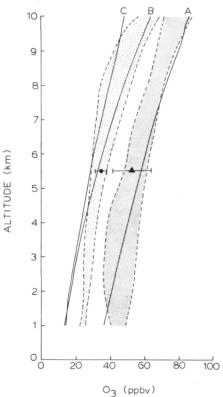
Hemispheric Differences in Ozone May Be a Result of Large-Scale Pollution

The light- and dark-stippled areas in the figure clearly illustrate the fact that the background ozone concentrations in the troposphere (i.e., the lowest 10 km of the atmosphere) are considerably higher in the Northern Hemisphere than in the Southern Hemisphere. The darker area is the range of observations from climatological data taken between 30°N and 50°N, whereas the lighter area represents a comparable data base for 30°S to 50°S. A subsequent set of aircraft measurements taken at a nearly constant flight altitude of 5.5 km has reconfirmed this asymmetry, and the 30° to 50° averages for the Northern and Southern Hemispheres are depicted by the error bars around the triangle and circle, respectively.

As part of an ongoing research program at NASA Langley, a numerical model of tropospheric photochemistry has been developed to try to explain why these hemispheric differences in the distribution of tropospheric ozone exist. It is possible that average meteorological conditions in the two hemispheres may be considerably different and that the differences in the observed distributions of tropospheric ozone may reflect these meteorological differences. The vertical profiles depicted by curves B and C in the figure represent two calculations in pristine air (typical of the Southern Hemisphere). The differences in these two curves are a result of using prescribed meteorological parameters that are representative of the observed meteorological processes in the two hemispheres. As can be seen from this figure, neither profile seems to be a reasonable simulation of the

observed ozone distribution in the Northern Hemisphere troposphere. If, however, pollutant trace gases (in particular, carbon monoxide, nitric oxide, and nonmethane hydrocarbons) are included in the calculations, the photochemical production of tropospheric ozone is substantial. As a result, the computed vertical profile with elevated levels of these emitted pollutants (curve A) agrees reasonably with the observed distribution in the Northern Hemisphere. Since nearly 95 percent of the industrialized emissions of these pollutants are located in the Northern Hemisphere, the results of this modeling study suggest that the hemispheric asymmetry of tropospheric ozone is caused by man-made pollution.

Jack Fishman, 3109



Model-derived and observed tropospheric ozone distributions.

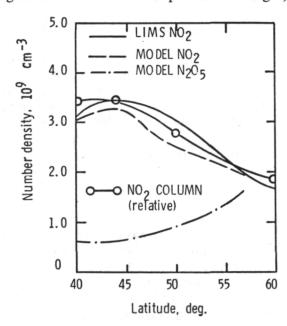
Effects of Transport and Photochemistry on Stratospheric NO₂ Distributions

In 1975, wintertime measurements of the latitudinal column distribution of atmospheric NO₂ revealed a remarkably sharp decline near 45°N to 50°N latitude. Observations showed NO₂ column reductions of 80 percent within 3° to 5° latitude near 270°E. Subsequent ground-based measurements con-

firmed the earlier ones and suggested that the gradients were associated with a strong zonal flow and declining temperatures toward the pole. The primary effect occurs in the 30- to 10-mb region of the atmosphere and near the edge of the polar vortex. Past theoretical modeling studies have not been able to reproduce the presence of such gradients, and developing the ability to explain the phenomenon was assigned a high priority by the National Academy of Sciences.

Satellite measurements of temperature and stratospheric constituents taken in January 1979 have been used with a contemporary photochemical model to explain the observed sharp NO₂ gradients. The LIMS satellite measurements of temperature were used to infer wind fields and construct trajectories followed by air parcels in the Northern Hemisphere winter. The measurements of temperature, O₃, NO₂, HNO₃, and H₂O were used to initialize photochemical calculations, which were then carried out along the trajectories of interest.

Results of the study indicate that the sharp declines in stratospheric NO₂ with increasing latitude can be explained by the conversion during transport at high latitudes of NO₂ to N₂O₅. The high levels of N₂O₅ and reduced levels of NO₂ persist at the lower latitudes due to the short winter days and the comparatively long N₂O₅ lifetime against photodestruction. Calculations indicate that the major effect has been determined to be associated with a temperature field conducive to parcel motion, which allows conversion of NO₂ to N₂O₅ (i.e., motion to higher latitudes with less exposure to sunlight). The



LIMS satellite measurements of NO2, Jan. 1979.

figure illustrates the sharp decline in NO₂ column sum and in NO₂ at 10 mb as observed by LIMS satellite measurements in early January 1979. Also shown for comparison are NO₂ distributions at 10 mb, which are the result of photochemical calculations applied along selected trajectories. The good agreement between the calculated and observed distributions of NO₂ confirms the above explanation of the presence of the surprisingly sharp latitudinal NO₂ gradients.

Linwood B. Callis, 2985

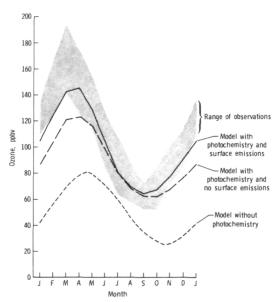
Modeling Seasonal Cycles of Tropospheric Trace Gases

During the past decade, a considerable database has evolved for several important trace gases in the troposphere. From this wealth of measurements, it has become evident that some trace species have increased in concentration since the 1970's. For some species, such as the chlorofluoromethanes, it is clear that anthropogenic activity is responsible for the observed increase, since these species have no natural sources. For other trace gases, such as nitrous oxide (N₂O) and methane (CH₄), the observed increase has forced scientists to reassess the impact of man's activities on their atmospheric cycles. At one time it had been believed that the biological sources and sinks of these trace gases should overwhelm any perturbation created by industrialized activity. The observed increase in the concentration of these particular trace gases has caused us to reexamine the natural sources and sinks of these particular trace species.

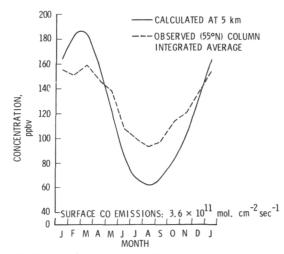
Another finding that has evolved from all these recent measurements is that certain trace gases exhibit specific seasonal behaviors. In particular, seasonal cycles are now well established for tropospheric ozone (O3) and carbon monoxide (CO). In order to understand what processes dominate the seasonal aspects of these tropospheric species, a theoretical study using a one-dimensional photochemical model of the troposphere has been developed. As can be seen from the figures, the model calculates reasonable seasonal cycles for O3 and CO, two species whose databases are sufficient to have well-defined seasonality. Another finding that emerges from this study is that a very large seasonal cycle should also be present for the reactive oxides of nitrogen: nitric oxide (NO) and nitrogen dioxide (NO₂). The model calculations indicate that the concentration of the sum of these two trace gases ranges from 0.014 ppbv in the summer to 0.117 ppbv in the winter at an altitude of 5 km.

Because these concentrations are so small, these species are very difficult to measure and only a few measurements are currently available in the remote, unpolluted troposphere. However, if we are to obtain a clear understanding of the geochemical cycles of atmospheric trace gases, it is imperative that a substantial database be established for the oxides of nitrogen since they play a central role in the geochemical cycles of so many trace gases. This modeling study further indicates that an initial attempt to establish such a database may be more fruitful during the winter than during the summer. The attainment of a good database for the nitrogen oxides is one of the primary goals of NASA's Global Tropospheric Experiment, which will utilize aircraft instrumentation to measure tropospheric trace species.

Jack Fishman, 3109



Observed and model-derived ozone at 10 km.



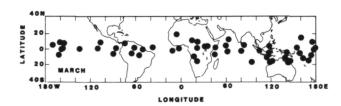
Model-derived CO seasonal cycle.

SAGE Observations of Cirrus Clouds in Lower Tropical Stratosphere

The mean upward transfer of air into the stratosphere is believed to be contained primarily within intense thunderstorms that penetrate through the tropopause and into the stratosphere at low latitudes. During the collapse of these overshooting convective towers, cirrus clouds may be formed above the tropopause as tropospheric air mixes with stratospheric air. Although the detailed mechanism for transferring tropospheric air into the stratosphere is unclear, geographical regions where air enters the stratosphere may be found by documenting locations of stratospheric cirrus.

Sightings of stratospheric cirrus in tropical regions have been determined from 1-µm aerosol extinction profiles obtained by the satellite-borne Stratospheric Aerosol and Gas Experiment (SAGE). A search was performed on the SAGE data set to identify events with large enhancements in the aerosol extinction profiles at altitudes above the tropopause. Since enhancements in the extinction profiles were infrequent and occurred during periods of near-background aerosol conditions, these events were identified as stratospheric cirrus. The locations of each cloud sighting were compiled for the spring seasons between February 1979 and June 1981.

The figure shows the accumulated cloud sightings for the month of March from 1979 to 1981. Most of the sightings of stratospheric cirrus are found near Micronesia, Indonesia, the African and Amazon tropical basin, and a small region near a longitude of 160° W. Entry areas, shown by the outlines in the figure, are inferred from regions where cloud sightings are more numerous. Comparisons of these entry areas with entry areas of tropospheric air determined from other studies were found to be in agreement. Cloud sightings observed from the SAGE data set did show additional entry areas over remote ocean regions not presented in previous studies. The accumulated sightings of stratospheric cirrus for the months of April, May, and June show that the number of cloud sightings gradually decreased and shifted northwards with the seasonal migration of the Intertropical



Accumulated sightings of stratospheric cirrus between 1979 and 1981.

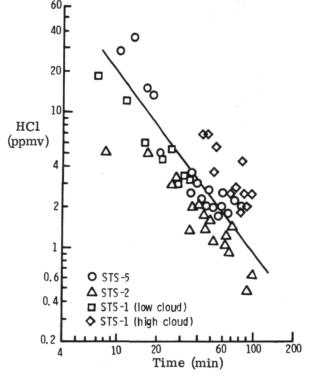
Convergence Zone. This suggests that the inferred entry areas also decrease in size and move northward.

M. P. McCormick, 2065

Airborne Measurements of Shuttle Exhaust Constituents

About 35,000 kg of hydrogen chloride (HCl) and 56,000 kg of aluminum oxide (Al₂O₃) are exhausted into the planetary boundary layer during Space Shuttle launches. These exhaust products could potentially lead to localized acidic deposition and short-term weather modifications. This research has focused primarily on characterizing the behavior of HCl and Al₂O₃ (particulates) in Shuttle exhaust clouds as they disperse and dilute with time. Airborne measurements of these constituents were made during penetrations into stabilized exhaust clouds from Space Shuttle launches STS-1, -2, and -5.

Although initial (within 12 min of launch) concentrations of HCl measured in the three exhaust clouds ranged from 5 to 30 ppmv, in-cloud HCl concentrations were found to decrease with time in a systematic and predictable fashion characterized by an empirical power law expression for dispersion (see figure). Most of the HCl was found to be in aqueous



Peak HCl concentrations measured from aircraft penetrations of Shuttle exhaust clouds.

cloud droplets initially, but the ratio of aqueous to gaseous HCl decreased rapidly as the exhaust clouds aged. After about an hour, most of the HCl was in the gaseous phase. Although some part of the decrease in aqueous hydrochloric acid undoubtably resulted from droplet evaporation during dispersion, of more concern were indications that aqueous aerosol fallout was occurring.

Significant concentrations of small (0.1 to 1.0 μ m) and large (1.0 to 400 μ m) particulates were measured in the exhaust clouds. These small particulates would potentially be capable of residing in the lower troposphere for days, and could serve as cloud condensation nuclei and substantially impact natural warm-cloud processes. Several aircraft traverses beneath Shuttle exhaust clouds indicated extensive aerosol fallout of large acidic particles.

Wesley R. Cofer III, 4372

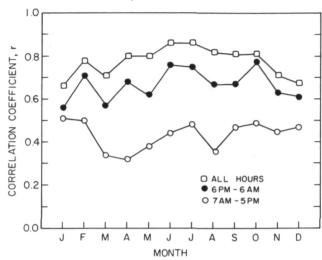
Stability of the Surface Layer and Its Relation to Dispersion of Primary Pollutants in St. Louis

The role of atmospheric stability in the lowest 30 m of the atmosphere in characterizing the dispersion of the primary pollutants CO, NO, and hydrocarbons was investigated using the 1976 air quality data set for St. Louis. Stability was determined in three separate ways: from tower measurements of the vertical temperature gradient ΔT , tower measurements of wind speed u, and an approximation to the bulk Richardson number B based only on ΔT and u in the surface layer.

High positive correlation coefficients were obtained between area averages of ΔT and each of the species for the inner urban area of St. Louis, as shown in the figure for carbon monoxide. Because the species concentrations were derived from a nonuniform area source, similar correlations at individual stations were somewhat poorer. At night, for low wind speed, the area-averaged species correlation coefficients for ΔT and B are positive and significant. but they are poor for wind speed alone. For all other situations, correlation diagrams for wind speed versus species show appreciable scatter, and B, as it has been used in this study, is not a sensitive parameter for estimating surface pollutant concentrations. Use of a stability parameter that includes the mixed layer height, in addition to ΔT and u, will result in a quantity that exhibits a greater range for correlation studies. These findings should be considered when urban air quality models are parameterized and

evaluated in terms of their ability to disperse primary pollutant distributions.

Gerard E. Woodbury, 2065



Monthly correlation coefficients between ΔT and the ratio of atmospheric to emitted CO.

Structures Directorate

The Structures Directorate conducts basic research and develops technology in the areas of advanced aerospace materials and composites, structural mechanics and dynamics, unsteady aerodynamic structural loading and aeroelasticity, and noise generation by aircraft propulsion systems and structures. This technology development is directed toward reducing both weight and cost of aircraft and space structures while increasing their reliability and service life. The technology developed also provides improved design capability through more accurate prediction of aerostructural loads, vibration, and noise.

The Materials Division conducts research on advanced materials and their application to aircraft and space structures. The Division also develops novel polymeric, metallic, and ceramic materials for these applications. The materials processing and fabrication sciences are developed, and the application of materials to specific flight and space structures is demonstrated. The Division conducts research on thermal protection materials and systems for application to supersonic aircraft and to the Space Shuttle. The fatigue and fracture behavior of materials is studied in specialized laboratories to provide practical methods for insuring structural integrity. Specialized facilities are also used to study the behavior of materials under extreme conditions of high and low temperature, pressure or vacuum, and electromagnetic radiation.

The Structures and Dynamics Division conducts research on structures for advanced aircraft, space vehicles, and space stations. Analytical methods are developed for the prediction of static and dynamic stresses and strains in complex structures. Research is conducted on transient response of structures to aircraft control systems and landing dynamics. Specialized facilities are used to study the dynamics and deformations of aircraft crashes. The division develops new structural systems for aircraft and space structures. It is also active in computer science research and software development for structural analysis and design.

The Loads and Aeroelasticity Division conducts research in aeroelasticity, aerothermal loads, unsteady aerodynamic loads, and multidisciplinary analysis and optimization of advanced aircraft and space structures. Analytical methods are developed for aeroelastic deformations and instabilities and for dynamic, vibratory, and thermal response of structures. Multidisciplinary analysis techniques are developed to design and optimize aerospace structures.

The Acoustics and Noise Reduction Division conducts research on the generation and propagation

of aircraft noise. It seeks to understand the relationships between unsteady aerodynamics, structural dynamics, and noise generation by the interaction of fluids with solid surfaces. This research is directed toward predicting and reducing the noise from helicopter rotors, conventional and advanced aircraft propellers, and turbofan engines. Research is conducted on the propagation of noise from its source through the atmosphere and through aircraft structures.

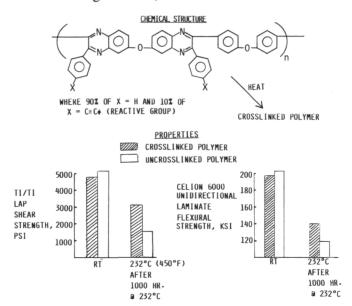
Lightly Crosslinked High-Temperature Structural Resins

Many high-temperature polymers are thermoplastics; deformation occurs when they are placed under a load at temperatures approaching the glass transition temperature (Tg). In an attempt to retain the attractive features of thermoplastics, such as toughness and thermoformability, while improving their high-temperature dimensional stability and solvent resistance, latent reactive groups were placed pendant along the polymer backbone. These groups can be thermally induced to crosslink the molecules, thereby increasing the Tg and altering other properties. By controlling the number of reactive groups and, accordingly, the crosslink density, cured materials can be obtained with good toughness, thermoformability, solvent resistance, and improved high-temperature mechanical properties.

To prove this concept, work was performed with a model system, a polyphenylquinoxaline (PPO), containing 10 mole percent pendant phenylethynyl groups (reactive) along the polymer chain structure shown in the figure. The mechanical properties of the PPQ with and without the pendant crosslinkable groups were determined. Thin-film properties of the PPQ with the pendant crosslinkable group at 232°C were significantly better than those of the PPO void of the pendant reactive group. The crosslinked PPO film displayed break elongation of 6 percent at room temperature and 14.5 percent at 232°C. Preliminary adhesive and composite performance of the crosslinked PPO compared to that of the linear PPO is shown in the figure. The room temperature adhesive and composite properties of the two types are very similar, whereas at 232°C, after 1000 hours in air, the crosslinked PPQ provided significantly higher retention of strength. This improvement at 232°C was accomplished without a major compromise in processability, toughness, or thermoformability. In addition, the crosslinked PPQ exhibited greatly improved solvent resistance.

More comprehensive work with PPQ containing pendant crosslinkable groups is under way. In addition, this general concept is being extended to improve the solvent resistance and elevated temperature properties of polysulfones and polyamides.

Paul M. Hergenrother, 3041



Lightly crosslinked polyphenylquinoxalines: high-temperature structural resins.

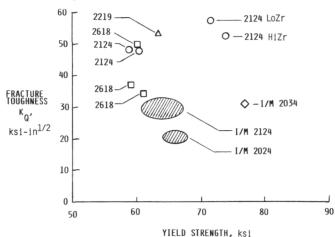
Advanced Powder Metallurgy Aluminum Alloys Develop High Strength-Toughness Combinations

Advanced aluminum alloys prepared using powder metallurgy processing of rapidly solidified powders continue to show strong promise for achieving stronger, tougher metallics for use in lightweight airframe structures. The rapid solidification rate (RSR) and powder metallurgy (PM) approaches have resulted in cleaner, more fine-grained, metallurgically stable structures which, in turn, have resulted in significantly better mechanical properties.

Under a NASA contract, Lockheed-California Company has been investigating several PM alloy compositions of the 2000 series (Al-Cu-Mg-X-X) which were prepared by the Aluminum Company of America. Compositions showing the most promising property improvements to date have been based on minor chemistry variations of 2124, 2219, and 2618 alloys. In each case, variation in chemistry from the conventional composition was based on expected behavior changes resulting from the RSR and PM processing. The figure shows the apparent combina-

tions of fracture toughness and yield strength achieved for eight powder metallurgy composition variations along with an ingot metallurgy (IM) 2034 heat of material and the locus of data on IM 2024 and 2124 extrusions. In general, the alloys prepared using PM techniques achieve considerably higher toughness values with little or no sacrifice in yield strength. This combination of properties is important because an improvement in strength or toughness cannot be exploited if it produces a decrease in the other property. The most promising composition investigated to date is based on 2124 alloy chemistry with zirconium added as a stabilizer. Zirconium additions in the 0.2- to 0.6-percent range resulted in toughness values of 50 to 60 ksi-in^{1/2} and corresponding strengths exceeding 70 ksi. If property combinations approaching these values could be realized in commercial production, significant improvements are possible in lightweight airframe structures designed according to durability and damage tolerance requirements.

W. B. Lisagor, 2036



Combinations of fracture toughness and yield strength for PM 2XXX Al alloy extrusions, -T8511 temper.

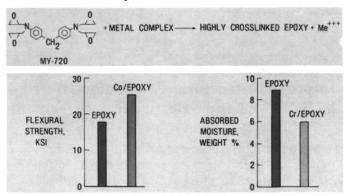
Metal-Ion-Containing Epoxies

Because of their excellent processability and low cost, epoxy resins have been widely used by the aerospace industry as composite matrix resins. However, these highly crosslinked polymers tend to be brittle and suffer from a lack of moisture resistance. Research has shown that the incorporation of certain metal ions into epoxies can produce property improvements, including increased mechanical strength and decreased moisture absorption.

The addition of 1 percent cobalt ions to an MY-720-based epoxy system has resulted in a 40-percent

increase in flexural strength. This increase was achieved with only a slight sacrifice in thermal stability and with no increase in the polymer density. The moisture resistance of MY-720 and Epon-828-based epoxies has been improved with the addition of as little as 0.2 percent chromium ions to the epoxy systems. This moisture resistance was achieved with no reduction in mechanical properties.

Diane M. Stoakley, 3041



Characteristics of metal-ion-containing epoxies.

A Fracture Mechanics Approach to Impact Delamination Damage

Thin composite plates are susceptible to damage from low-velocity impacts. The damage usually begins as local matrix shear failure. The impact area is softened and cracks grow outward from it. This soft area behaves as a membrane. Any viable analysis must therefore include membrane and flexural forces as well as incremental softening of the plate as delamination progresses. A fracture mechanics analysis has been developed which uses simple material properties to model the plate behavior under the assumption of matrix control.

The initial plate model consists of a purely flexural plate superimposed over a pure membrane. The displacements of each plate due to a quasi-static load are matched at the center and the sum of the restoring forces is set equivalent to the (static) load. Delamination progression is modeled by subdividing the flexural plate into an outer ring plate and an inner circular section. The inner circular section is divided into a stack of plates of equal thickness, representing axisymmetrically delaminated plies (see schematic of plate model). For a given plate configuration (plate radius, number of plies, and number of delaminations) membrane-coupled load displacement curves can be calculated for any delamination radius b. The energy released when delamination grows from radius b to b

+ Δb can be found from the energy integral between the two load displacement curves as shown in the figure. Delaminations are assumed to grow when the predicted releasable energy exceeds the characteristic value of the material. Repeating these calculations over a range of delamination radii produces a synthetic load displacement curve which includes the effects of delamination growth. Analytical curves for both a tough and a brittle matrix are shown compared

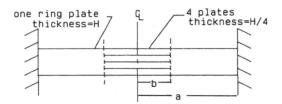
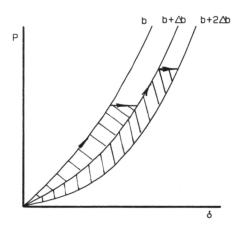
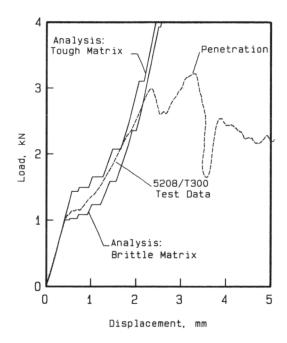


Plate model.



Fracture energy integration.



16-ply 2-in.-diameter plate.

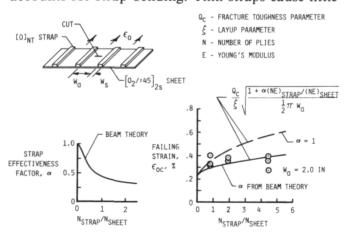
to test results for a 16-ply, 2-inch-diameter 5208/T300 specimen. The agreement is excellent up to a displacement of 2 mm. At greater displacements, the fracture process becomes fiber controlled rather than matrix controlled and the model is no longer applicable.

G. M. Bostaph, 2093

Damage Tolerance of Stringer-Stiffened Composite Panels

Stringers are known to improve the residual strength of damaged stringer-stiffened metal panels. Thus, 12-in.-wide composite panels with cocured, unidirectional strap-like stringers were tested for comparison. The sheets were cut between the middle two straps to simulate damage, and the panels were loaded in tension to failure. At the strain level at which plain sheets would fail, cracks initiated at the cuts, ran to the straps, and were arrested. Loading was continued until the crack ran again and completely failed the panel. In general, the failing strains were 40 to 60 percent greater than those for a sheet without stringers. Thus, stringers increase the strength of composite panels just as they do metal panels.

The figure shows some of the results for straps with a constant spacing W_a but with different thicknesses. Surprisingly, failing strains were not increased by increasing the strap thickness. A fracture mechanics analysis revealed that strap bending induced by load transfer near the crack tip ameliorates the benefit of increasing strap thickness. The graph shows measured and predicted failing strains that are applied to the sheet and straps. The solid and dashed lines were predicted with and without strap bending taken into account. The strap effectiveness factor α accounts for strap bending. Thin straps cause little



Predicting failing strains of stiffened sheets with damage.

bending and α = 1; as straps thicken, α decreases. For straps twice as thick as the sheet, $\alpha \approx 1/4$ and bending has its maximum effect. The difference between the dashed and solid lines suggests the amount that failing strains could be increased just by reducing strap bending. Strap bending can be reduced by locating the straps symmetrically on both sides of the sheet or distributing them through the thickness of the sheet, and by increasing Young's modulus of the strap material rather than thickness.

C. C. Poe, Jr., 2338

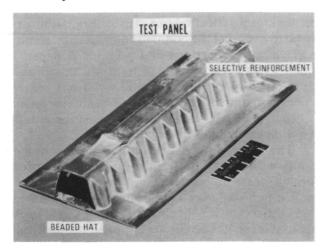
Improved Structural Efficiency Offered by SPF/WB and Selective Reinforcement

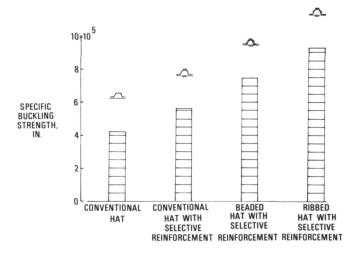
The structural efficiency of titanium compression panels has been increased significantly through the use of advanced forming and joining technology and by selective reinforcement using metal-matrix composites. Superplastic forming is a process in which titanium is capable of undergoing large plastic deformations or elongations (1500 to 2000 percent) without fracture. The process, which is accomplished at the annealing temperature of the material (1700°F), makes it possible to form geometric configurations to exacting tolerances that are not possible using conventional forming methods. Weldbrazing is a process developed at NASA Langley which combines the use of resistance spotwelding and brazing to join titanium and metal-matrix components efficiently and economically. Metal-matrix composites such as boronaluminum have a high specific strength and stiffness in the direction of the filaments and can be attached to titanium components by weldbrazing to significantly improve the load-carrying ability of compression members. Each of these technologies was incorporated to fabricate Ti-6Al-4V skin-stiffened compression panels. These panels were tested and the results compared with those for conventionally designed panels.

The specific compression buckling strengths of three superplastically formed and weldbrazed (SPF/WB) panel configurations which were selectively reinforced with boron-aluminum are compared with a conventional unreinforced hat-stiffened specimen. As shown, the use of selective reinforcement increased the strength of the panel with the conventionally shaped hat stiffener by 35 percent. Combining the selective reinforcement and the more efficient superplastically formed beaded-shaped hat stiffener or ribbed-shapped hat stiffener increased the strength of the panels by 80 percent and 120 percent, respec-

tively, compared to the panel with the conventional hat-shaped stiffener configuration. These results indicate an approach to significantly lower structural weight in advanced titanium airframes.

D. M. Royster, 3405





Buckling strength for SPF/WB selectively reinforced panels.

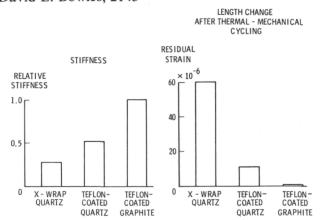
Improved Tension-Stabilized Cable Materials

Lightweight deployable cables are currently being used in certain antenna designs to shape the mesh reflector surfaces. Current cables are made of quartz fibers because quartz has a low thermal expansion, is inherently stable in the space environment, and can be made in small-diameter fibers. A typical cable, approximately 450 microstrain in diameter, is composed of approximately 2000 individual quartz fibers, 9 microstrain in diameter, held together

by a Teflon cross wrap. One of the problems with this type of construction is the difficulty in aligning the fibers and keeping them aligned during handling and storage of the cables. This results in a small (60×10^{-6}) but significant residual strain in the cable when subjected to repeated load or thermal cycles. Also, considerable variability is observed in this residual strain, making it difficult to accurately bias this out during fabrication when the precise length of each cable is determined.

As a result of a recent program conducted to develop improved cable materials, two major changes were made which significantly advanced space cable technology. Unidirectional composites were made by impregnating the bare fibers with Teflon while holding the fibers straight under tension to achieve a better alignment and minimize the amount of twist in the fiber along the cable. This resulted in an increase of about 100 percent in the relative stiffness of the cable and over 80 percent reduction in residual strain after repeated thermal-mechanical cycling. Further significant improvements were achieved by using graphite fibers in place of the quartz fibers.

David E. Bowles, 2143



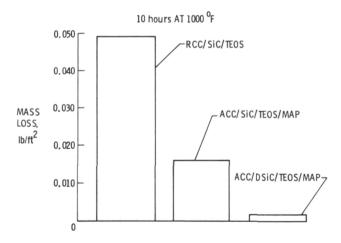
Comparison of characteristics of several cable materials.

Sealed and Doped Coatings Reduce Mass Loss of Carbon-Carbon Materials

Silicon carbide is widely used as an oxidationresistant coating for carbon-carbon materials and is the primary coating for the baseline material used as a thermal protection system in the leading-edge areas of the Shuttle. Silicon carbide will develop shrinkage cracks that allow the oxygen to enter the material. The technique used to reduce the entry of oxygen through these cracks is to coat the surface with TEOS (tetra-thyl-ortho-silicate), which forms a viscous glass sealer. This sealer is effective at the higher temperatures, but does not perform as well in the intermediate temperature range. In this intermediate temperature range, newly developed sealants show promise of dramatically reducing the mass loss due to oxidation. The Vought Corporation, under contract to Langley, has developed two techniques that have greatly improved oxidation resistance.

The figure shows mass loss after 10 hours of exposure at 1000°F for these two new materials compared to the Shuttle baseline material. The RCC/SiC/TEOS Shuttle baseline represents the state of the art in oxidation resistance. The ACC/SiC/TEOS/MAP is basically the Shuttle baseline with a substrate fabricated with PAN base graphite fibers instead of rayon base fibers and an additional overcoat of monoaluminum phosphate (MAP) applied to the surface. The addition of the MAP sealer reduced the mass loss rate to approximately 30 percent of the baseline. A further modification of the material was made which increased the oxidation resistance even more. The SiC coating was doped with boron. The doped and sealed coating (ACC/DSiC/TEOS/MAP) had 25 times the oxidation resistance of the baseline material in this temperature range. The sealed and doped material has potential uses in many other applications in addition to future Shuttle thermal protection systems.

C. W. Stroud, 2143



Effect of coatings and/or sealant on mass loss.

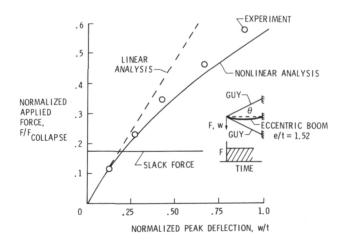
Guyed Space Boom Nonlinear Dynamic Response Predicted

Guyed-boom structures are presently being considered for space application as antenna feed masts.

As with any guyed boom, the guys must be pretensioned to provide boom stiffness, but in space applications the pretension loads are small to avoid buckling the slender boom. Thus, relatively small deflections of the boom tip due to maneuver or external disturbances can cause slackening of a guy. A slack guy provides no stiffness to the boom, and further boom deflection can cause the remaining taut guy(s) to overload the boom in compression, resulting in yet larger deflections and possible collapse. An analysis has been developed to study this problem parametrically for different configurations, material properties, and pretension levels, and the analysis was correlated with experimental measurements on a two-dimensional laboratory model.

The figure shows a comparison of experimental results with linear and nonlinear analytical predictions of peak lateral deflection values following an applied step load over a range of simulated maneuver loads. Also shown is the force level that would cause a guy to slacken if the load were applied statically. Due to the dynamic response of the system, slackening actually occurs at force levels lower than static, as reflected in the deviation of the linear and nonlinear predictions below the static force level. The nonlinear prediction follows the same trend as the experimental data, but overpredicts peak deflections by 13 to 15 percent. The reason for this discrepancy is not yet known, but in view of the highly nonlinear nature of the system, the correlation is considered quite good. The analysis has further been used to establish design regions for combinations of pulse level and duration for which boom tip deflections do not exceed given performance allowables.

Jerrold M. Housner, 2446

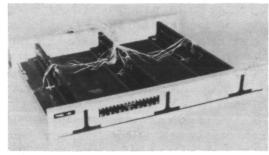


Analysis developed to predict nonlinear dynamic response of guyed space boom.

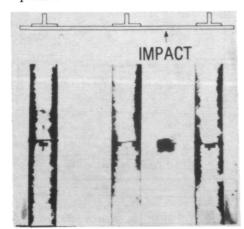
Damage Containment Concept Tested for Composite Compression Panels

Local damage can notably degrade the compression strength of graphite-epoxy structural components in aircraft, and current design practice is to limit allowable ultimate strain to around 0.0030 to allow for this possibility. For lightly loaded, stiffnessdesigned components such as control surfaces, this limit does not lead to significant mass penalties, but if graphite-epoxy is to be attractive for primary structures, the allowable ultimate strain should be increased to at least 0.0050. A promising method of achieving this increase is the stiffened-panel damage containment concept illustrated in the figure. The skin of this panel is composed totally of ±45°oriented plies (relative to the 0° load direction) which for a wing cover panel provides shear stiffness, while panel axial stiffness is provided by 0° plies placed in the stiffeners. The test panel was initially loaded to a strain of 0.0035 and impacted by a 1/2in.-diameter aluminum sphere at 300 ft/sec. The panel survived with local damage, as shown in the C-scan photograph.

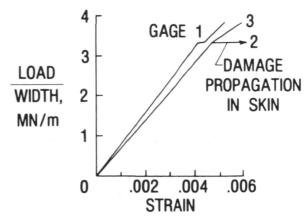
A subsequent load cycle resulted in the sequence of events indicated in the load-strain diagram and depicted in the three moire photographs. At a strain of 0.0034, the skin buckled into three halfwaves between stiffeners, and at a strain of 0.0040 the



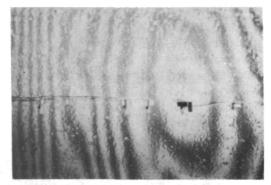
Stiffened panel.



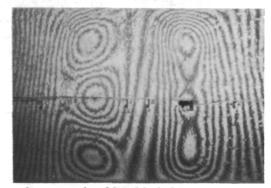
C-scan photograph.



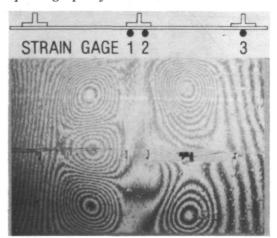
Load-strain diagram.



Moire photograph of zero load.



Moire photograph of buckled skin.



Moire photograph of local propagation.

damage propagated rapidly across the skin but was contained at two adjacent stiffener interfaces. The panel load was then increased to a strain of 0.0050 without further damage propagation, and C-scan inspection confirmed that skin damage did not extend beyond the stiffeners. This test demonstrates for the first time the potential of a structural configuration design for damage containment in a compression-loaded graphite-epoxy structure.

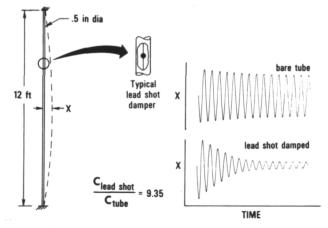
Jerry G. Williams, 3524

Impact Damping Substantially Reduces Slender-Strut Vibrations

High package efficiency for space-deployable antennas or platforms dictates the use of structural elements of extreme slenderness. Since such slender struts will vibrate easily, concepts are needed for damping these vibrations if structural stability is to be achieved. A relatively simple passive concept that can yield significant increases in system damping is illustrated here.

In this experiment, a slender, 1/2-in.-diameter steel tube 12 ft long was supported vertically on elastic end fixtures and a proximity gage was externally supported to measure lateral midpoint displacement (X). The tube was "plucked," and the resultant vibratory displacement time history showed the small amount of damping typical of support friction effects and/or inherent material damping. A single lightweight monofilament line was then installed in the tube, suspended from the top, and small-diameter lead shot were clamped to this line in varying numbers at different levels along the tube.

The displacement time history shown resulted when the tube was "plucked" with one lead shot suspended on the line at each of the quarter points



Impact damping to reduce slender-strut vibrations.

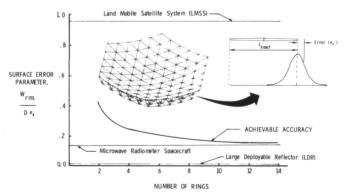
(for a total of three shots). Damping coefficients (C) were calculated by the logarithmic decrement method for both the bare tube and the lead-shot-damped tube, and the ratio shown on the figure reveals an increase in damping of almost an order of magnitude for the lead shot combination. Thus, such simple passive concepts should not be overlooked in the search for ways to control space structure vibrations.

Harold G. Bush, 2498

Limits of Achievable Accuracy Defined for Truss Antenna

Tetrahedral trusses are currently being considered for forming a stiff, stable reflector surface for large antennas. Even with careful manufacturing procedures, however, the many struts that form the truss structure possess length errors that can contribute to a nonideal reflective surface. To assess the magnitude of surface distortion errors, the length error of each strut is assumed to be random with a normal distribution, zero mean, and standard deviation $\sigma_{\mathcal{E}}$. The structural deformations caused by the imperfect struts are calculated with a finite-element analysis which is performed a large number of times with different sets of randomly selected member errors

A surface error parameter (the rms normal surface error nondimensionalized by reflector diameter and member error standard deviation) is plotted versus the number of rings in the truss. A typical ring is shown shaded on the five-ring deflector in the figure. The line denoted "achievable accuracy" was obtained from the results of the finite-element analysis. The requirements for the three antennas shown are based on the rather common assumption of the rms surface error being equal to 1/20 of the operating wavelength (regardless of number of rings).



Limits of achievable accuracy defined for truss antenna structure.

The Land Mobile Satellite System (LMSS) and the microwave radiometer have similar operating wavelengths, but because the LMSS is much smaller in diameter (55 m vs 750 m), its surface accuracy requirement is much more easily met. The Large Deployable Reflector (LDR) has only a 20-m-diameter surface, but because the operating wavelength is less than 1 mm, its surface accuracy requirement cannot be met by the truss structure alone. For such cases, the current analysis can be used to define the dimensional range that a control system will have to provide.

William H. Greene, 2892

Tendon-Controlled Boom Concept

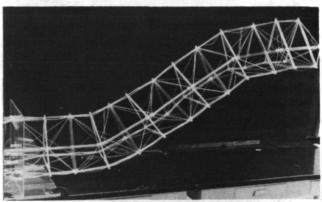
Deployable, controllable-geometry beams represent a class of structures with the potential of providing highly mobile and compactly packageable manipulator systems for space operations. One category of beam structure which appears to be particularly well suited for manipulator-boom applications is the tendon beam, which makes use of a segmented central column and flexible longerons ("tendons") supported on frames.

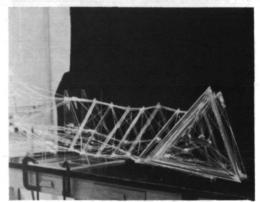
A workable concept for a tendon-controlled boom has been developed under a task agreement contract with Virginia Associated Research Campus, and a simple working model was designed and fabricated to demonstrate the concept. The model is shown deployed in three characteristic shapes: straight; bending upward in an S-curve; and bending laterally in a C-curve. The model is constructed of Plexiglas tubing and Dacron line and has six moveable segments, each of which has six tendon lines to control its angular orientation with respect to the adjacent supporting segment. The 36 tendons are led to the root of the beam and thus constitute the tension elements of the beam. For concept demonstration only, the model is controlled from the base by means of a three-arm lever to which the tendons are anchored, and constrains the motion of the model to four structural degrees of freedom.

The model has proved to be stable and controllable throughout the range of shapes thus permitted, and the concept is considered suitable for further development, especially in the areas of deployment and in more sophisticated, "joystick" controlled manipulations of the boom.

Martin M. Mikulas, Jr., 2551







Tendon-controlled boom concept.

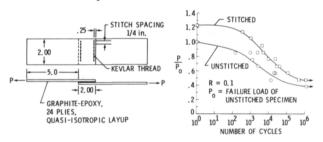
Stitching Improves Strength of Composite Joints

Transverse stitching has been found to have a beneficial effect on both static and fatigue strength of secondary bonded, cocured graphite-epoxy single-lap joints. Tests were conducted on similar specimens with and without Kevlar stitch reinforcement (stitched before curing with zero stitch thread tension) to determine ultimate strength and fatigue life. Static test variables included two adherend thicknesses, single and multiple rows of stitching, three stitch spacings, and four overlap lengths. Fatigue tests were

conducted on specimens with a 2-in. overlap length with and without a single row of stitching, and with the minimum-to-maximum cyclic load level ratio R = 0.1. As shown in the figure, test results indicate that a single row of stitches near each end of the overlap can offer up to a 38 percent improvement in static failure load compared to the unstitched specimen.

The improvement in static failure load was generally greater for longer overlap lengths and for thicker adherends, but no significant effects due to stitch spacing were observed for the load range investigated. Also, additional rows of stitching do not result in any further improvement in joint failure load. The figure also shows that, for joints with a 2-in. overlap length, stitching increased the fatigue life by an order of magnitude or more compared to the unstitched joints. The stitched specimens used for this investigation do not represent optimum configurations and the results probably represent a lower bound for improvements due to stitching; better manufacturing and stitching procedures would probably result in larger improvements in joint failure load.

James W. Sawyer, 2239



Transverse stitching improves strength of graphiteepoxy bonded single-lap joints.

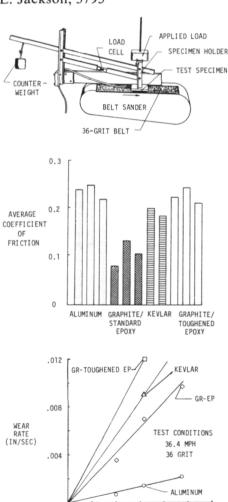
Friction and Wear Behavior of Composite and Aluminum Airplane Skins

Experimental tests were conducted to characterize the wear and frictional behavior of aluminum and advanced composite coupons under loading conditions typical of those occurring on a transport aircraft skin during emergency slideout on a runway surface. The experimental apparatus shown used a belt sander to provide the sliding surface for the tests. Standard aluminum oxide sanding belts of 30- to 60-grit size were determined to have a mean texture depth comparable to typical runway surfaces. Normal and frictional forces were calculated from a static analysis of the specimen (coupon) holder and used to determine the dynamic friction coefficient. Specimens

were weighed before and after test runs of approximately 5 seconds duration to determine material wear rates under loads ranging from 2 to 5 psi. Under identical test conditions, the standard graphite-epoxy materials exhibited a coefficient of friction of about half that obtained for aluminum, whereas the DuPont Kevlar and toughened resin composites showed frictional values similar to aluminum.

Material wear rates show a nearly linear increase in wear rate with increasing applied load for all materials, but show an order of magnitude larger wear rate for the composite materials compared with aluminum at a load of 3.2 psi. The toughened resin composites, which had a friction coefficient comparable to aluminum, show the highest wear rate of the materials tested. Further testing is planned to determine the effect of varying surface texture and velocity on specimen wear rate and coefficient of friction.

Karen E. Jackson, 3795



Comparisons of friction and wear behavior of aluminum and composite airplane skins.

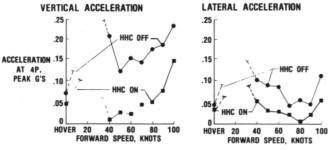
LOAD (PSI)

Higher Harmonic Control System Effective in Reducing Helicopter Vibrations

The goal of the Higher Harmonic Control (HHC) vibration reduction system is elimination of helicopter fuselage vibrations that occur at the helicopter blade passage frequency. Higher harmonic control is achieved by superimposing nonrotating swashplate sinusoidal motions at the blade passage frequency (four cycles per rotor revolution (4P) for a four-blade rotor) upon the basic collective and cyclic flight control input to the blades. This is accomplished by sensing the vibrations with accelerometers and feeding the signals via an electronic control unit back to a digital computer programmed with a selfadaptive optimal control law. Command signals from the computer are routed to hydraulic actuators attached to the swashplate. The amplitude and phase of these signals are such that the swashplate and the rotor blades are driven to minimize the vibrations.

A flight test program is under way to validate the success in vibration reductions achieved in tests conducted in Langley's Transonic Dynamics Tunnel and to assess factors that cannot be studied properly in the wind tunnel test, such as system power consumption and reaction of the system to maneuvers. The Hughes OH-6A aircraft shown has flown both manually operated and closed-loop HHC flights from hover to 100 knots with significant vibration reductions obtained with both systems in steady-state





Control system reduces helicopter vibrations.

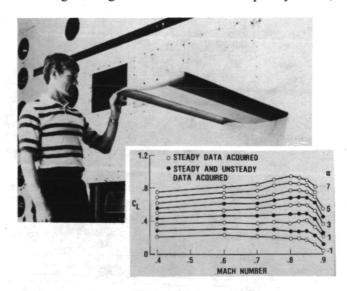
flight and considerable vibration reductions obtained in maneuvering flight. These flight tests represent the first in-flight application of an active control system for reducing helicopter vibrations.

John H. Cline, 2661

Transonic Pressure Distributions Measured on a Rectangular Supercritical Wing Oscillating in Pitch

Steady and unsteady transonic pressure data tests for aiding in the development and early assessment of new analytical computer codes are being made on a variety of wing configurations at NASA Langley. One of these, a rectangular wing model having a 12-percent supercritical airfoil section and a panel aspect ratio of 2 was recently tested in the Langley Transonic Dynamics Tunnel (TDT) in both freon and air. The model was attached to an electrohydraulic rotary actuator that was used to pitch the model both statically (at angles of attack up to 13°) and dynamically (at frequencies up to 20 Hz). The model is shown in the tunnel mounted with a splitter plate to divert the tunnel wall boundary layer.

Instrumentation included 123 pressure transducers, 8 accelerometers, and an angle-of-attack potentiometer. Steady and unsteady pressures were measured for a large number of model and tunnel conditions in the TDT using Freon as the test medium. The scope of this data base is shown in the plot of wing total lift coefficient versus Mach number for a range of angles of attack. For the open symbols,



Transonic pressure distributions measured on a rectangular supercritical wing oscillating in pitch.

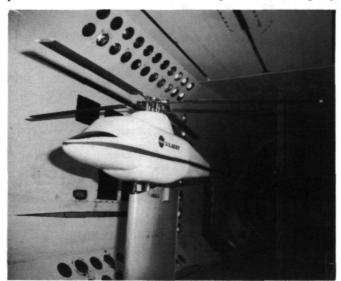
only steady pressure data were acquired. For the closed symbols, both steady and unsteady data were acquired. The unsteady data were measured with the wing oscillating at frequencies of 5, 10, 15, and 20 Hz. This newly acquired large data base is currently being used to assess the accuracy and efficiency of the new transonic computer code XTRAN3S.

Rodney H. Ricketts, 2661

Hingeless-Rotor Experiments Validate Analytical Method

The Aeroelastic Rotor Experimental System (ARES) is a generalized helicopter rotor test rig used in the Transonic Dynamics Tunnel (TDT) to study dynamic characteristics of new rotors. One goal of the ARES effort is to develop the capability to successfully test hingeless-rotor configurations. An important part of this capability is the prediction of aeromechanical stability characteristics before actual wind tunnel testing begins. In order to make pretest stability predictions and have confidence in them, a reliable analytical method is needed. To determine the suitability of one such analysis, a reseach program was conducted which involved correlating hingeless-rotor in-plane damping predictions with measurements made on the ARES in the TDT.

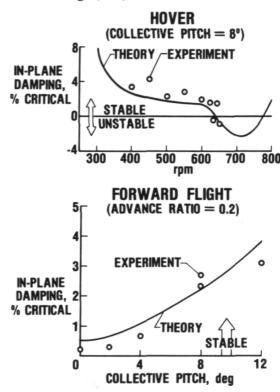
The analysis chosen to make the rotor in-plane damping predictions was the Comprehensive Analytical Model of Rotorcraft Aerodynamics and Dynamics (CAMRAD) Program developed at NASA Ames. Predictions were made of rotor in-plane damping as a function of rotor RPM and collective pitch for hover and forward flight. The damping



Hingless-rotor model in TDT.

predictions were made for a baseline rotor configuration as well as for configurations incorporating changes to blade sweep and droop, pre-cone of the blade pitch axis, and blade pitch-flap coupling. CAMRAD predictions were in good agreement with the values of damping obtained in hover, accurately predicting the instability that occurred at about 650 RPM. Good correlation is also seen between CAMRAD and values of in-plane damping obtained in forward flight at an advance ratio of 0.20.

William T. Yeager, Jr., 2661



Hingeless-rotor experiments validate analytical method.

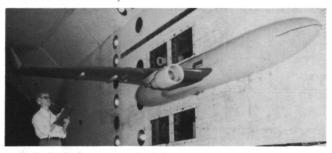
Transonic Flutter Studies of Effects of Winglets Extended to Twin-Engine Transport Type Wing

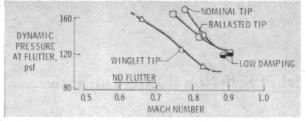
Transonic flutter tests were conducted in the Langley Transonic Dynamics Tunnel (TDT) using an existing, Boeing-built, 1/10-size semispan flutter model of a twin-engine transport type wing. The objectives were to determine experimentally the winglet effect on flutter for different variations in configuration parameters and to correlate these results with analysis. The model is shown cantilevermounted in the TDT. The model was equipped with three different wingtips: a nominal wingtip, a tip with

a winglet, and a nominally shaped wingtip that was ballasted to simulate the winglet mass properties. Model configuration parameters investigated included wing fuel loadings, pylon stiffness, and winglet cant angle. In addition, low-speed semispan model tests in the TDT were conducted to determine mass-density ratio effects on winglet flutter.

As an example of the test results, the winglet effects on the flutter dynamic pressure for the empty wing are shown. The winglet aerodynamic effect (the difference between the flutter boundary for the winglet tip and that for the ballasted tip) is much greater than the mass effect and has the deleterious effect of causing a reduction in wing flutter dynamic pressure of about 20 percent near the transonic dip. In general, pretest analyses were in good agreement with test results.

Charles L. Ruhlin, 2661





Transonic flutter studies of effects of winglets extended to twin-engine transport type wing.

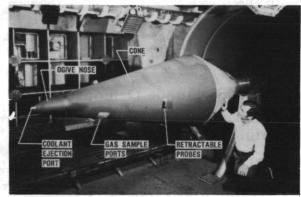
Mass Addition Film Cooling Tests at Mach 6.8

Mass addition film cooling (forced ejection of a fluid from the surface) is an attractive method of providing thermal protection from hostile aerodynamic heating. Film cooling is an active system that could benefit space transportation and reentry vehicles by supplementing passive thermal protection systems in local areas experiencing excessive heat loads. Although many experimental and analytical studies have been conducted on film cooling, very little experimental data exist for high-enthalpy hypersonic-flow conditions. Therefore, a test program was

conducted in the Langley 8-Foot High-Temperature Tunnel to study the cooling effectiveness of both forward-facing and surface-tangential coolant ejection of gaseous nitrogen using a large 12.5° cone with a base diameter of 3 feet. The model, shown in the figure with the forward-facing nose, also had solid nose tips to obtain baseline data with no coolant ejection. Shadowgraph and schlieren photographs of the nose region were obtained to help define the complex coolant flow field interaction. Three sets of retractable probes on the model were used to measure the shock flow field. Mach number, and temperature distributions with and without coolant ejection. Two surface ports were used to take gas samples that were analyzed by an on-line quadrupole mass spectrometer to obtain mixing ratios of the coolant and test gas. For these tests the nitrogen coolant was seeded with an inert tracer gas.

Test results with forward-facing coolant ejection show substantial reduction in surface heating rates, pressures, shock layer Mach numbers, and temperatures, even far downstream. Mass spectrometer analyses of gas taken through the sample ports confirm the presence of substantial coolant at the surface in the region where heating was reduced. Schlieren and shadowgraph pictures reveal that the coolant test gas interface was essentially stable. Only limited results were obtained with the tangential ejection nose. However, the heating reduction in the region near the nose was equivalent to the reduction for the forward-facing ejection nose.

Robert J. Nowak, 3115



Mass addition film cooling of a 12.5° cone at Mach 6.8

Noncatalytic Coating for Metallic TPS Reduces Heating

For the same entry conditions, a metallic surface of an entry vehicle will usually be subjected to a higher

heating rate than a nonmetallic surface. This difference occurs because metallic surfaces are generally catalytic to the recombination of dissociated air molecules, and the energy of dissociation released during recombination adds to the heat load. A noncatalytic coating will reduce the heat load to the surface and greatly increase the thermal efficiency of the metallic TPS.

A proprietary ceramic coating was evaluated by exposing coated and uncoated Inconel 617 specimens in an arc tunnel facility using both air and nitrogenonly test streams. The emittances of specimens were measured, and coated specimens were subjected to 80 thermal shock cycles in a 2000° F furnace to evaluate the adhesion of the coating to the metal. The measured emittance of the coated and uncoated (but oxidized) specimens was 0.65 and 0.8, respectively. The coating remained attached during the thermal shock cycles, and the emittance did not change. For the tests in air, arc tunnel test conditions were established which resulted in a temperature of 1753° F on the uncoated specimen. The coated specimen was tested at the same condition, but reached only 1353° F. Radiation equilibrium heating rates were calculated using the maximum measured surface temperatures and the measured emittances. The heating rate on the coated specimen in air was 37 percent of the heating rate on the uncoated specimen and in nitrogen the heating rate was reduced to 28 percent. Preliminary calculations show that about twice as much nitrogen was dissociated in the nitrogen test stream as in air. From these results, nitrogen recombination is shown to be the dominant surface catalytic effect.

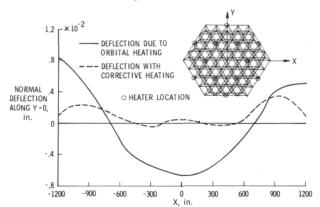
Claude M. Pittman, 3155

Analytical Technique Demonstrates Control of Space Structure Thermal Distortion by Applied Heating

As a first step in developing analytical procedures to demonstrate the feasibility of using applied heating to control thermal distortions in orbiting spacecraft, appropriate equations have been developed and solutions obtained to determine the corrective temperatures at specified control points which offset distortions caused by orbital heating. The optimum temperatures are those which minimize the overall (rms) distortions of the structure from its ideal shape. The calculations were performed using closed-form solutions for free-free beams and were then extended to the general case of a finite-element-modeled structure.

The procedure has been implemented in the EAL/SPAR finite-element analysis program and demonstrated for the reflector of a 750-m radiometer antenna. The antenna is in low Earth orbit and is distorted by a combination of solar, Earth, and albedo heating. A thermal analysis was performed and a worst-case temperature distribution selected. Twelve control points were located, as shown. The original and corrected distortions are compared in terms of the normal deflections along a diagonal of the dish. The rms distortion of the dish was reduced by a factor of 4 and the maximum distortion was reduced by a factor of 7.

Howard M. Adelman, 3451



Control of antenna thermal distortion by corrective heating.

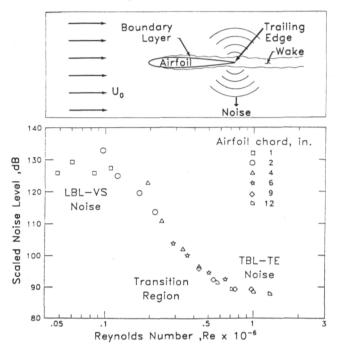
Airfoil Self-Noise: Effect of Scale

A comprehensive study of airfoil self-noise was performed in Langley's Aircraft Noise Reduction Laboratory quiet flow facility. Data were obtained for NACA 0012 airfoils of various chord lengths tested over a range of low subsonic velocities. In addition to acoustic measurements, hot-wire probes surveyed the boundary layer near the trailing edge to provide accurate parameters for the evaluation of scaling laws.

Two noise mechanisms are of particular interest here. At high Reynolds numbers (Re), the boundary layer is primarily turbulent, producing turbulent-boundary-layer trailing-edge (TBL-TE) noise. However, at lower Re, the boundary layer remains primarily laminar. Instabilities within the laminar boundary layer (LBL) result in vortex shedding (VS), which produces noise levels higher than that of the TBL-TE noise mechanism. An examination of the Re dependence of the overall noise level, normalized with an edge diffraction scaling law, has revealed an

important result. The scaling is found to collapse the noise data as a unique function of Re. This "reversed-S" curve is the first evidence indicating that the transition between the two noise mechanisms can be quantified. The result holds promise for increased understanding of these mechanisms and is valuable even now as a prediction tool (e.g., for broadband rotor noise).

Thomas F. Brooks, 4316

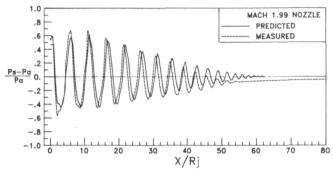


Normalized sound pressure levels.

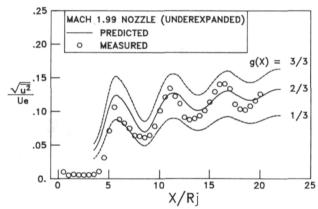
Shock Noise Associated With Supersonic Jet Plumes

Broadband shock noise, which originates from shock-turbulence interactions, was previously found to depend strongly on the shock wave and turbulent mixing layer characteristics near the end of the jet plume's potential core. A new parabolized Navier-Stokes code, SCIPVIS, has been investigated to determine its applicability to predict aerodynamic features of an evolving supersonic jet plume which are pertinent to broadband shock noise. The SCIPVIS code, which solves a fully coupled system of viscousinviscid equations, was specifically developed by Sanford Dash of Science Applications, Inc., to treat the strongly interactive processes that originate between the evolving turbulent mixing layer and decaying shock wave structure. The results of this investigation have shown that the SCIPVIS code provides a realistic description of jet plume development when compared to experimental observations.

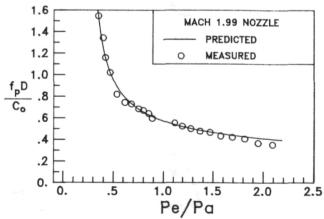
A good comparison between the computed and measured plume static pressure is shown over a region extending well beyond the end of the plume's potential core (see figure). This good agreement was obtained for several supersonic exit Mach number jets for both underexpanded and overexpanded flows where plume resonance was negligible (absence of screech mode). The evolution of the turbulent mixing layer in a shock containing supersonic flow was also



Computed and measured plume static pressure variation.



Computed and measured evolution of turbulent component.



Measured and computed acoustic far-field peak frequencies.

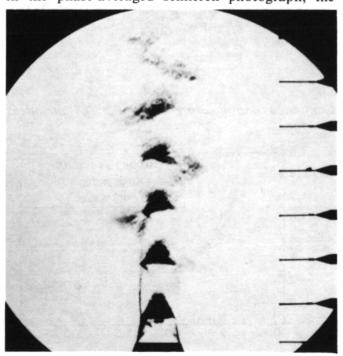
found to be realistically represented when compared to experimental measurements using a wedge-shaped hot-film probe (see figure). Using the simulated jet plume, as calculated by the SCIPVIS code, a good comparison was found between measured and computed acoustic far-field peak frequencies for the broadband shock noise component (see figure).

John M. Seiner, 3094

Shear Layer Instability Related to Screech Generation

A recent research program examined the role of shear layer instabilities in the generation and maintenance of jet screech. This acoustic component, which originates from a self-sustained aeroacoustic feedback resonance phenomenon, has been known to cause aircraft structural fatigue in sustained flight. The results of this research have clearly documented that a direct relationship exists between the generation of intense stable screech tones and a dominant helical instability wave in the jet column.

The experimental investigation included both near- and far-field microphone arrays to measure the radiated screech component, and a phase-locked flow visualization method to optically deduce the associated time-dependent aerodynamic features. As is shown in the phase-averaged schlieren photograph, the



Helical instability in Mach 2 nozzle. Phase-averaged schlieren photograph.

shock-containing supersonic plume for the case of intense stable screech exhibits a clearly visible helical structure as the dominant feature of the supersonic turbulent mixing layer. The measured acoustic far-field screech amplitudes for several supersonic nozzles demonstrate that intense stable screech is observed over a narrow Strouhal number region (reduced frequency) forming a peak near $S_D = 0.25$. A similar peak occurs near $S_D = 0.22$ for the maximum amplitude of a helical instability wave as computed from a linear inviscid stability analysis for the supersonic jet.

These results indicate that the apparent role of the shock waves is to provide the required coupling between the instability and the sound field. The helical structure is enhanced by the azimuthal excursions of the shock cells driven by the upstream propagating helical sound field.

James C. Yu, 2617

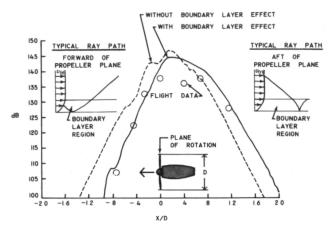
Boundary Layer Effect on Propfan Noise

Noise levels from a propfan model mounted on a business jet were measured at several locations on the fuselage and found to be considerably lower than those predicted by current noise prediction programs. The analysis used in these programs assumes that the sound propagates from source to receiver through a uniformly moving homogeneous medium. Since the microphones were located on the aircraft fuselage, the air near the microphones was stationary with respect to the microphones, whereas the air 3 in. above the microphones moved, with respect to the microphones, with a velocity equal in magnitude to the flight velocity. This velocity differential implies the presence of a boundary layer; that is, a layer of air within which the fluid velocity varies smoothly from zero to the flight velocity. Within this boundary laver. the acoustic field from the propfan model is altered from that which would be present if the flow velocity were constant. This alteration is in the form of refraction, the bending of the rays away from the fuselage forward of the propfan and toward the fuselage behind the propfan, as indicated in the figure.

Detailed analysis of the sound field within the boundary layer provides a boundary layer correction which, when applied to the predicted sound field for a uniformly moving medium, significantly improves the correlation. The figure shows the measured levels and the predictions with and without the boundary layer corrections. The data are for a flight Mach number of 0.8 at the fundamental blade passing

frequency of 1013 Hz. Here X/D is the distance in front of the propeller plane (negative values) or behind the propeller plane measured in propeller diameters.

Gerry L. McAninch, 2645



Boundary layer effect on propfan noise.

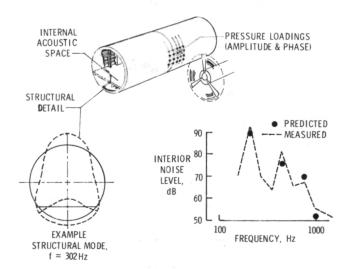
Comparison of Pusher and Tractor Propeller Noise

In response to the need for design information on possible noise penalties of advanced aircraft configurations, an experimental study was conducted. In this study a "pusher" configuration, in which the propeller is mounted behind the wing or tail of an aircraft, was simulated in a vertical-jet anechoic wind tunnel. Here the propeller was placed behind an airfoil that simulated a wing or horizontal tail. Noise measurements were made at several stations to determine the difference in propeller noise radiation with and without the wing upstream of the propeller. The study showed that the wake introduced additional noise at all measurement stations, with the maximum contribution being along the plane of the wing, fore and aft of the propeller plane. The wake produced as much as a 10-dB increase over the noise of the propeller without the wake. The study also showed that the frequency spectrum of the additional noise contains much higher sound pressure levels in the higher harmonics. These higher harmonics fall in the range known to have high annoyance factors, but they can be effectively treated with sound-absorbing materials at appropriate locations along the aircraft fuselage.

Analytical Prediction of Aircraft Interior Noise

In the absence of an accurate interior-noise analytical model, the usual industry procedure is to extrapolate sound pressure levels from similar aircraft operating under similar flight conditions. The obvious disadvantage of this procedure is the loss in accuracy with large design changes; in addition, the procedure is not conducive to new or novel noise reduction concepts. A new analytical prediction model being developed under contract with Bolt Beranek and Newman is illustrated here. One input to the analytical model is the complex pressure loading (amplitude and phase) of a propeller as calculated by the propeller noise prediction module from the Langley Aircraft Noise Prediction Program. Additional inputs can include the boundary layer or other sources of noise. The analysis then couples this pressure loading to the dynamic modal response of the shell structure using measured or estimated structural and acoustic loss factors. The analysis accounts for the acoustic radiation of the vibrating structure by using the impedance and the coupling of structural modes with interior acoustic modes to determine the sound pressure level for each selected harmonic of the propeller blade passage frequency.

Comparisons have been made between measured and predicted one-third-octave-band interior-noise spectra for a cylindrical fuselage model with propeller noise input and are indicated in the figure. The cylinder is stiffened with ring frames and stringers and has a floor, thermal-acoustic insulation, and interior trim. Good agreement was found for the first four harmonics of the propeller blade passage frequency. The model is undergoing further refinement



Propeller aircraft interior-noise validation tests.

to improve dynamic representation of interior trim. Additional validation studies will be made using aircraft ground runup and inflight data.

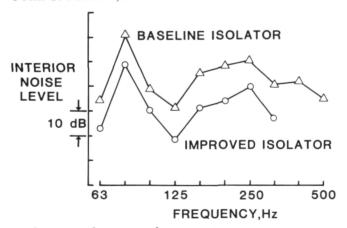
William H. Mayes, 3561

Reduction of Structureborne Noise

Results of ground tests at Southwest Research Institute showed that structureborne noise is a major source of noise in single-engine aircraft. Several analytical techniques for predicting the level of the structureborne noise were explored, including a finite-element model of the engine support system, fuselage, and cabin space. Best results were obtained using a semiempirical model that used finite elements for the engine, isolators, and engine support framework, and used measured dynamic properties to represent the fuselage and cabin space. This analytical model was verified through extensive laboratory tests on a single-engine aircraft using a mechanical shaker attached to a simulated engine mass. Good agreement was found between predicted interior-noise characteristics and measured levels over a wide range of shaker input conditions and interior measurement positions.

Following verification of the model, variations in isolator dynamic properties as well as variations in isolator designs were studied to determine the noise reduction that might be achieved with better isolator systems. No available isolator had the optimum stiffness and damping, so several configurations were tested, including off-the-shelf and special designs. Results are shown for the isolator that provided the greatest improvement. Substantial reductions (>10 dB) are indicated in the structureborne noise over a wide range of frequencies.





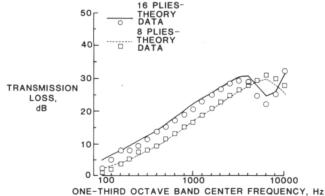
Reduction of structureborne noise.

Noise Transmission Loss of Advanced Composite Panels

Because of the increasing use of composites in aircraft construction, methods for the prediction of noise transmission of composite panels are needed to assess and/or tailor composite designs to ensure acceptable interior noise levels. An experimental and theoretical study has begun to provide noise transmission information for design of composite aircraft structures. Twenty-eight panels constructed (inhouse) of advanced composite materials (graphiteepoxy, fiberglass-epoxy, and Kevlar-epoxy) were tested in the Aircraft Noise Reduction Laboratory transmission loss apparatus. The panels of each material type generally had different numbers and orientations of plies, and two of the graphite-epoxy fabric panels had microballoon-epoxy cores. Noise transmission loss (TL) of each panel was measured in one-third octaves over the frequency range from 100 Hz to 10 kHz.

Typical results for two graphite-epoxy tape panels are shown. An anisotropic infinite-panel theory was developed and is shown to predict the TL of these two panels very well. Because of the factor-of-2 mass difference, the 16-ply panel had approximately 6 dB greater TL than the 8-ply panel over most of the frequency region. Because of the greater stiffness of the 16-ply panel, the "coincidence dip" occurs at a lower frequency than for the 8-ply panel. The coincidence dip occurs at frequencies for which the wavelength of the flexural waves in the panels coincides with the wavelength of the incident sound projected on the panel. The lowest coincidence frequency for a given panel is called the critical frequency. In general, for all the panels tested, the magnitude of prediction error (measured TL-predicted TL) was less than 3 dB except near the critical frequency.

The analytical model is being updated to predict TL for finite panels (including low-frequency stiffness and resonance-controlled regions). The models will



Noise transmission loss for graphite-epoxy panels.

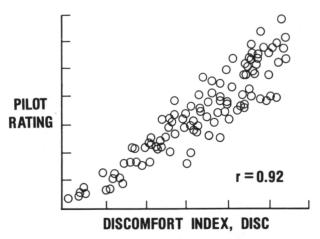
then be used to determine the potential of tailoring composites to obtain high noise reduction in selected frequency bands.

Clemans A. Powell, 3561

Evaluation of Ride Quality Prediction Methods for Operational Military Helicopters

A joint NASA-Army-Navy program was conducted to obtain in-flight measurements of cabin and/or cockpit interior noise and vibration levels during routine operational flights on eight military helicopters. These measurements were used as inputs for subjective tests in the NASA ride quality simulator. A total of 36 Army and Navy pilots made comfort ratings of 120 selected ride environments representative of those measured in flight. These ratings were analyzed and correlated with various ride comfort indices (e.g., one that includes separate acceleration and noise levels, and the NASA discomfort index). These indices were calculated from the noise and vibration environments reproduced on the simulator.

It was found that ride comfort indices based upon either noise or vibration alone were poor predictors of crew comfort. However, the NASA ride discomfort index (which accounts for both noise and vibration) correlated highly with obtained comfort ratings (correlation coefficient of 0.92) and also predicted comfort response accurately over the total range of vibration and interior noise conditions. Thus, the NASA Ride Comfort Model, which includes the discomfort index, is a useful and versatile



Comparisons of pilot discomfort rating and predicted discomfort for helicopter noise and vibration environments.

tool for predicting and assessing helicopter ride quality. The model should also provide a means of specifying ride comfort limits for design purposes in terms of a single discomfort index that inherently accounts for both noise and vibration.

Additional tests are being conducted to validate the NASA Ride Comfort Model for surface vehicle environments, such as those in automobiles, trucks, and trains.

Jack D. Leatherwood, 3561

Projects Directorate

The Projects Directorate is responsible for the implementation and management of specific tasks related to carrying out NASA Langley's research and technology role in aeronautics and space. These tasks include the following projects or functions: the Aircraft Energy Efficiency (ACEE) Project, the Earth Radiation Budget Experiment/Stratospheric Aerosol and Gas Experiment (ERBE/SAGE II) Project, the Long Duration Exposure Facility (LDEF) Project, the Scout Project, the Aeronautical Systems Office (ASO), and the Space Technology Flight Experiments Office (STFEO).

Management responsibilities explicitly include principal decisions concerning program content, scheduling, budgeting, operations planning, contract monitoring, and other aspects of project implementation. Responsibilities for assigned functions or projects include preparation of operating plans; negotiations with NASA Headquarters and other government agencies, universities, and industry; and administration of program funds and travel and manpower resources.

Advanced Composite Structures Technology

The NASA ACEE Composite Medium-Primary Program for large transport aircraft has completed ground tests of three full-scale empennage components. The last of these, the DC-10 composite vertical stabilizer, was successfully tested to failure at 167 percent of design limit load following a series of durability and damage tolerance tests. FAA certification of this composite design is expected in late 1984. Boeing has reached agreement with a commercial airline for installation of two shipsets of 737 composite horizontal stabilizers and flight service beginning in early 1984.

Focused technology development for application of composites to wing primary structure is under way with the transport companies. This development includes damage tolerance characterization, heavily loaded bolted-joint design and validation, and systems requirements for lightning protection and fuel containment. Tests of wing panel designs representing 40 percent less weight than current aluminum designs have demonstrated residual strains up to 0.005 µin./in.with highly visible structural damage. Design parameters for mechanically fastened composite joints have been obtained through tests and successfully applied to the design and analysis of heavily loaded

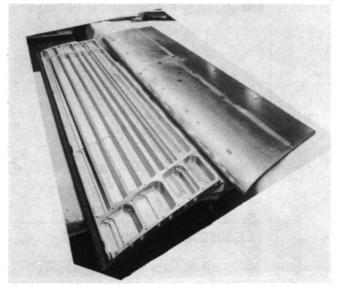
composite joints with multiple fasteners. Joint design strains of $0.005~\mu$ in./in. have been demonstrated by tests. Numerous tests to assess lightning protection techniques for wing box designs, which also serve as fuel tanks, have successfully reduced the severity and frequency of backface sparking from mechanical fasteners; however, further study is required to avoid sparking completely. The evaluation of new tougher resin systems and high-strain fibers are included in the focused technology program.

Herman L. Bohon, 3081

Laminar-Flow-Control Technology

Under a NASA Langley contract, the Douglas Aircraft Company designed and fabricated three laminar-flow-control (LFC) electron-beam-perforated (EBP) suction panels. The three EBP suction panels (total chord of 7 feet) will be installed and tested in place of three slotted suction panels currently under evaluation on an LFC airfoil model in the Langley 8-Foot Transonic Pressure Tunnel. Fabrication of these panels is a demonstration of an advanced structural technology for large EBP LFC panels for commercial transport applications. The forward panel and its understructure are illustrated in the photograph. The fabrication techniques used are applicable to a modern aircraft production line, with surface tolerances significantly improved compared to current production line practice.

Lockheed-Georgia Company and Douglas Aircraft Company (under contract to NASA Langley) have each designed, fabricated, and delivered leadingedge LFC test articles to Dryden Flight Research



LFC suction panel.

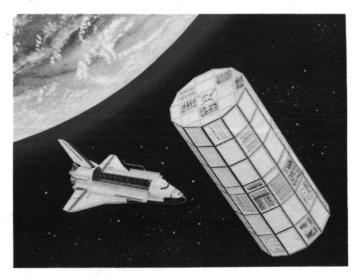
Facility (DFRF) under the Leading-Edge Flight Test (LEFT) Program. The test articles contain all the systems that could be required in the leading-edge box of a future commercial LFC transport. Each test article contains a suction system, an anti-insect contamination system, and an anti-icing system. The suction system is designed to allow the achievement of laminar flow to the front spar 12-percent chord). These 6-foot-span test articles and their supporting systems are currently being installed on the Lockheed JetStar at Dryden Flight Research Facility. Flight testing will be performed to obtain the operational sensitivity, maintenance, and reliability data needed to establish that practical solutions exists for the leading-edge area of a future commercial transport employing laminar flow.

Michael C. Fischer, 2045

New Thermal Design/Integration Concept

A new concept for the thermal design and integration of a large number of experiments on a single Shuttle-transported spacecraft has been developed. The concept, which was applied to the first mission of the Long Duration Exposure Facility (LDEF), substantially reduced the integration analysis effort and cost.

The concept has three phases. Phase I involves preliminary design, analysis, and parametric studies of the total spacecraft over a range of orbital conditions to provide thermal boundary conditions and thermal design guidelines. In Phase II, each experimenter has total responsibility for the design



LDEF spacecraft.

and thermal analysis of his experiment, based on Phase I results. Phase III involves conversion of each of the experimenter's final thermal models into a common, equivalent format. The equivalent experiment models are incorporated into the LDEF thermal model, and the facility thermal analysis is performed. Trade-off studies on experiment location on the spacecraft are conducted to satisfy thermal and other requirements. From this analysis, the final experiment configuration is established and documented for use in Shuttle integrated thermal analyses.

This new concept was used to integrate 48 experiments on the LDEF. It should be useful in processing large numbers of experiments for future LDEF missions and other similar Shuttle payloads.

Robert F. Greene, 4571

Technology Integration for Subsonic Transport Aircraft

Current studies of technology integration applied to subsonic transport aircraft (cruise Mach number = 0.8) have shown that large increases in operating efficiency are possible relative to current vehicles. The significant configuration features include high-aspect-ratio wings, advanced structures, advanced propulsion systems, natural-laminar-flow surfaces, and twin fuselages. Twin-fuselage configurations allow practical aspect ratios (AR) higher than those of single-fuselage configurations (AR = 18 as compared to 12) when both wings have the same wing root bending moment. High aspect ratios give low chord Reynolds numbers, resulting in increased natural laminar flow.

The advanced structures consisted of composite materials and metal sandwich fuselages; both result in reduced weights. In addition, composite materials yield smoother surface finishes to facilitate natural laminar flow. The metal sandwich fuselage gives an improvement in fuselage minimum drag by lessening fuselage contour distortions due to pressurization and reduced air leakage. The propulsion systems consisted of two aft-mounted propfan engines with counterrotating pusher propellers. Two engine technology levels were considered: near term (typical of the year 1987) and far term (typical of the year 2010). Large levels of natural laminar flow were achieved due to the high aspect ratio, composite-material surface finish, and off-wing engine location.

The payoff for this propulsion system configuration is 303 passenger miles per gallon (pmpg) for the near-term technology level and 409 pmpg for the far-term propulsion system configuration, as compared with 80 pmpg for a current-technology twinengine turbofan aircraft.

Charles E. K. Morris, Jr., 4576

Application of Emerging Technologies to Supersonic Fighter Concept

The application of emerging technologies has identified a new class of supersonic fighter aircraft. Technologies include advanced propulsion systems consisting of high-specific-thrust engines and twodimensional thrust vectoring/reversing nozzles, advanced materials, advanced aerodynamics, and conformal weapons. The engine nozzle deflection axis, vehicle center of gravity, and wing center of pressure are all nearly longitudinally coincident. Advanced engines with thrust-to-weight ratios of 10 or better can result in high vehicle thrust-to-weight ratios (1.4 for the configuration shown) without undue penalty in takeoff gross weight when sized for maximum sustained "g" capability. (Current fighters have thrustto-weight ratios slightly greater than 1.0.) The resulting high levels of thrust and low levels of pitching moment allow the use of thrust vectoring to enhance both maneuver and low-speed performance characteristics. Good high-speed performance is achieved by matching wing aerodynamics and engine characteristics to the Mach 2 cruise requirements.

The application of the emerging technologies offers advances over current fighters which are due in

Supersonic fighter concept.

large measure to the synergism of advanced-technology integration. The calculated performance of these configurations includes an all-supersonic-cruise 500-nautical-mile mission radius, unrefueled intercontinental ferry range, near-vertical takeoff and landing characteristics, and a sustained "g" capability equal to or greater than that of current fighters.

Samuel M. Dollyhigh, 4576

Systems Engineering and Operations Directorate

The function of the Systems Engineering and Operations Directorate is to support ongoing aeronautical and space research at NASA Langley. This workforce is divided into four divisions with specific support functions. The Systems Engineering Division is responsible for mechanical, electrical, and systems engineering functions required to provide research models and flight hardware for aerospace research, applications, and technology. The Facilities Engineering Division is responsible for engineering and design of aerospace research and development equipment and institutional facilities for aeronautical and space research, such as special handling equipment, model supports, and special test equipment. The Fabrication Division is responsible for developing and fabricating aeronautical and aerospace research hardware related to ground support equipment as well as research facilities test equipment. This Division provides developmental manufacturing technology and electronics technical support, including communications systems and instrumented hardware. The Operations Support Division is responsible for providing the technical, mechanical, electrical, and maintenance services for research and institutional facilities. This Division operates laboratory equipment and wind tunnels, and collects, records, and interprets test data. In addition to the four divisions, the Facilities Program Development Office, the National Transonic Facility Project Office, and the Systems Safety, Quality and Reliability Office are all responsible to the Directo-

Because of the unique requirements of some of the aerospace research performed at the Center, both engineer and technician are involved in doing limited applied research in solving finite engineering and fabrication problems. These problems relate to support hardware and software in providing the experimental systems requested by research. The following contributions represent typical support engineering and fabrication research and technology undertaken by the Systems Engineering and Operations Directorate.

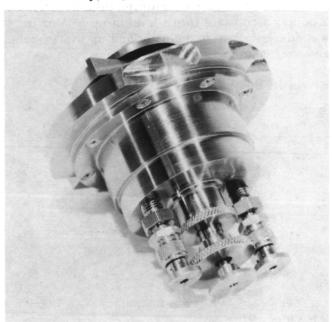
Five-Axis Adjusting Mechanism

The Laser Heterodyne Spectrometer (LHS) is an instrument developed at NASA Langley to optically measure the vertical profiles of atmospheric gasses that are currently believed to play a major role in depletion of stratospheric ozone. The Local Oscillator

Control Platform (LOCP), the core of the optical receiver, contains the tunable-diode laser (TDL) and associated components that cool, align, and focus the TDL with the optical system. One of the problems encountered in manufacturing a TDL is accurate alignment of the energy beam. Since no commercial device was available to correct this problem, the five-axis adjusting mechanism was developed to compensate for this misalignment as well as for misalignments caused by other manufacturing tolerances.

The five-axis mechanism consists of a jacking screw (0.025 in. pitch) arrangement in the vertical direction and one axis in the horizontal direction, a gear-driven lead screw (0.031 in. pitch, 15:1 ratio) in the other horizontal direction, and rack and pinion gears in the azimuth (211:1 ratio) and elevation (15:1 ratio) adjustments. This mechanism has a range of adjustment of ± 0.10 in. horizontal (two directions) and vertical, $\pm 6.0^{\circ}$ azimuth and $\pm 30.0^{\circ}$ elevation. Since the LOCP housing is evacuated (for thermal reasons), all appropriate joints have vacuum seals. A high degree of precision is required in machining most parts.

E. A. Crossley, Jr., 4621



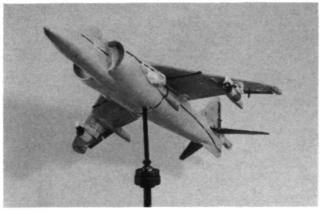
Five-axis adjusting mechanism.

Radio-Controlled Positive Propulsion System for Tunnel Model Spin Recovery

Miniaturized solid-propellant rockets and radiocontrolled circuitry have been combined into a safe, simple, lightweight, low-cost system being used to study stall/spin recovery of subscale aircraft models. The increasing severity of penalties associated with conventional spin recovery parachute systems, contrasted with significant improvements in performance, safety, and reliability levels of propulsion systems, has sparked renewed interest in rockets for spin recovery.

The effectiveness of positive-propulsion stall/ spin recovery, as compared to spin parachutes, for numerous aircraft types is being systematically investigated using the demonstrated capability of this radiocontrolled positive propulsion system. The first application defines full-scale propulsion requirements for the AV-8B Advanced Harrier V/STOL aircraft. Up to two rocket circuits are simultaneously initiated from a single electrical signal controlled by radio commands which sequentially operate a safe/arm relay and a motor firing servo. The model's on-board receiver only responds to commands with a correctly coded (modulated) pulse train at the proper frequency. When firing, the motor's thrust produces a yawing moment to counter the spin-induced inertia, and this initiates spin recovery by placing the aircraft into an aerodynamically recoverable mode. Aircraft recovery is considered optimum if spinning ceases two to three turns after motor ignition. Each motor produces a constant thrust level of up to 5 oz for 4 seconds, is 1/2 in. in diameter and up to 2 in. long, and weighs up to 12 g.

Melvin H. Lucy, 4621



AV-8B model.

Low-Temperature Cryoseals

One of the more difficult problems in cryogenic research is maintaining a seal when thermally cycling a pressure vessel at cryogenic temperatures. When opening and closing the vessel at these extremely low temperatures (-200° F and below), elastomeric and

rubber seal materials are very inelastic and in some cases brittle. This is because the sealing material passes through the glass transition temperature common to all organic materials subjected to cryogenic regimes. This phenomenon, plus a differential thermal expansion coefficient (on the order of 10) between the metal and the elastomeric or rubber material, produces tensile stress on the sealing material, limiting its usefulness in a cryogenic seal.

A seal made of room-temperature vulcanized (RTV) rubber encapsulating a spiral nichrome wire heater produced a seal with elasticity in excess of 100 percent. The RTV rubber has 200 percent elasticity at -170° F, and this drops to 0 percent at -200° F. The heater encapsulated in the rubber maintains a temperature in the seal of approximately -170° F even when the vessel temperature is below -200° F, thus keeping the seal material elastic and preventing leaks.

John D. Buckley, 3131



Low-temperature RTV cryoseal.

Structural Verification Test and Dynamic Analysis for LDEF

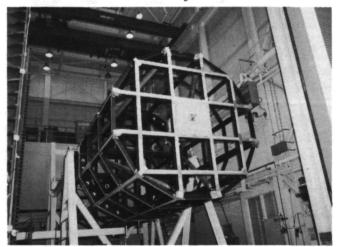
Dynamic analyses have been performed on the Long Duration Exposure Facility (LDEF) primary structure to determine stresses, deflections, and accelerations. This analysis was performed using a specially developed digital computer program for a class of problems which have a statically determinant support system. This approach allows a more cost-effective way of evaluating the structure using "canti-

levered" modal properties. Analysis of 34 discrete events representing the response of the Space Shuttle LDEF at lift-off and landing included data generation and evaluation for 84 grid points and 347 structural elements. At each integration time step, accelerations, deflections, member loads, and member stresses were calculated and the maximum and minimum values were saved. A data base for this information was developed to make evaluation practicable. Queries for overall maximums/minimums could be made very quickly by taking advantage of the random-access features of the data base program. In addition to tabular comparisons, plots of selected data versus time were developed to evaluate cumulative structural damage.

A series of structural load tests on the LDEF primary structure have been conducted. These tests had a three-fold purpose: (1) to demonstrate structural adequacy of the assembled LDEF primary structure when subjected to anticipated flight loads; (2) to verify analytical models and methods used in loads and stress analysis; and (3) to perform tests to comply with the Space Transportation System (STS) requirements.

Test loads were based on predicted limit loads considering all flight events. Simulation of these limit loads on specified structural elements was accomplished by applying discrete load sets to the LDEF. Four physical tests were required to subject all critical structural elements to verification test levels. Hydraulic jacks in combination with fabric straps distributed test loads on the structure at 34 locations to simulate the predicted landing condition. The data monitored were load (both applied and reacted) strain, and deflection measurements.

Evaluation of the test results shows good agreement between predicted and observed load, strain, and deflection data. In addition, test data show that the LDEF structure was subjected to 1.2 times limit



LDEF in test support frame.

load to meet the STS requirements. The structural adequacy of the LDEF was demonstrated as a result of this test.

T. C. Jones, 4508

Improved GN₂ Flow Blocker for NTF Fan Shaft

The main drive fan hub and part of the drive shaft of the National Transonic Facility (NTF) are housed in the upstream nacelle, which provides both structural support and an aerodynamic fairing for the assembly. Inside the nacelle, nitrogen gas (GN2) flow is restricted by a flow blocker (seal) around the fan shaft at the upstream nacelle bulkhead. Operational temperatures from +150° F to -320° F and pressures from 8 psia to 130 psia (2 psi ΔP), combined with severe bulkhead thermal distortions, result in a very serious design problem. The problem is compounded by the 600-RPM shaft speed. A conventionally designed seal utilizing fiberglass and Teflon materials proved to have a useful life of only a few hours operational time. Analysis of the seal failure revealed two causes: bulkhead thermal distortion, which was corrected by relocating the seal to another part of the shaft, and shaft surface speed, which at 7600 FPM is much too high for most materials.

For the final design, a high-density wool felt that was treated with a fire retardant was chosen. The 1/4-in.-thick sheets of felt were cut into 90° segments, with four segments to a ring. Teflon spacers were cut in a similar manner from 1/8-in.-thick tetrafluoroethylene sheets. The seal is made up of five felt rings separated by four Teflon rings and held in place by an aluminum structure. Since the Teflon rings are slightly larger than the shaft, a small cavity is formed on either side of the felt rings, which provides the labyrinth effect that improves seal efficiency. The seal runs on a 9-percent nickel-steel shaft treated with a MoS_2 surface-bonded lubricant.

Edward A. Crossley, 4621

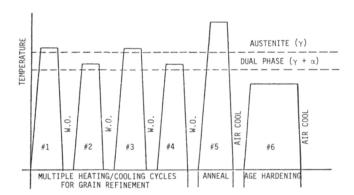
Grain Refining Heat Treatments To Improve Cryogenic Toughness of High-Strength Steels

The development of two high Reynolds number wind tunnels at NASA Langley which operate at cryogenic temperatures with high dynamic pressures

has imposed severe requirements on materials for model construction. Existing commercial high-strength steels lack sufficient toughness to permit their safe use at temperatures approaching liquid nitrogen (77 K). Therefore, a program to improve the cyrogenic toughness of commercial high-strength steels was conducted at Langley.

Significant improvement in the cryogenic toughness of commercial high-strength martensitic and maraging steels has been demonstrated through the use of grain-refining heat treatments. Charpy impact strength at 77 K was increased from 50 to 180 percent for the various alloys without significant loss in tensile strength. The grain sizes of the 9-percent Ni-Co alloys and 200-grade maraging steels were reduced to 1/10 of the original size or smaller, with the added benefit of improved machinability. The grain refinement process consists of multiple heating and cooling cycles alternating between the austenite (γ) and the dual-phase austenite-plus-ferrite ($\gamma + \alpha$) region, followed by rapid cooling to reduce the grain size. The grain refinement cycles are followed by annealing and age hardening or tempering as required to restore strength. This technique should permit these alloys with ultimate strengths of 220 to 270 ksi to receive consideration for cryogenic service.

H. F. Rush, 4666



Typical grain-refining heat treatment.

Solid-Particle Seeding for Laser Velocimeters

Laser velocimetry is the first nonintrusive wind tunnel flow measurement system to gain wide acceptance. The main problem that remains has been the development of an artificial seeding mechanism that will deliver an adequate number of particles of the desired size, which will result in less tunnel operating time per data point. A relatively inexpensive particle seeding system that meets this criterion has been developed at NASA Langley. The system employs commercially available particles suspended in 95 percent ethanol which are injected by an agitated, pressure pot paint sprayer.

A data rate of 4500/sec was obtained in the smoke tunnel at Langley using a 1-W laser seeded with 4.9 cc of 50 percent polystyrene latex (in water) per gallon of ethanol. The injection rate of the ethanol suspension was 0.125 gallons per hour. The same data rate is obtained by substituting 2.25 g of 0.7-\mu kaolin for the 4.9 cc of polystyrene latex (all other conditions remaining the same). Some visible attachment of particles to the tunnel screens has been noted when using the kaolin, but not with polystyrene latex. Kaolin is available inexpensively in 1.1-\mu m and 1.5-µ m particle sizes for situations where larger particles are necessary. Polystyrene latex is also available in sizes larger than 0.5 µm but is extremely expensive. A dry-particle seeding system is also under development at Langley.

Cecil E. Nichols, Jr., 4641

Technology Utilization Office

One of NASA's Congressionally mandated responsibilities is to promote economic and productivity benefits to the nation by facilitating the transfer of aerospace-generated technology to the public domain. NASA's means of meeting this objective is its Technology Utilization Program, which provides a link between the developers of aerospace technology and those in either the public or private sectors who might be able to employ the technology productively.

One important facet of NASA's Technology Utilization Program is its applications engineering projects, which involve the use of NASA expertise to redesign and/or re-engineer existing aerospace technology to solve problems encountered by federal agencies or other public-sector institutions. Applications engineering projects originate in various ways. Some stem from requests for NASA assistance from other government agencies and some are generated by NASA engineers or scientists who perceive possible solutions to public-sector problems through the adaptation of NASA technology. In addition, NASA employs various applications teams throughout the country. These teams contact public-sector agencies, medical and public-health institutions, and professional organizations to uncover significant problems in fields such as health care, public safety, transportation, and industrial processes which might be amenable to solution by the application of NASA technology. The projects reported on here are typical of the applications engineering efforts conducted at NASA Langley in support of the Technology Utilization Program

Ultrasonic Temperature Monitor for Hyperthermia

Localized hyperthermia has been demonstrated to be an effective method for preferentially destroying malignant tumor cells. Hyperthermia irradiation (typically microwave energy) affects primarily the malignant cells interior to the tumor, since those cells have an inadequate blood supply and are unable to conduct away much of the induced heat. Thus, cells within the tumor can be destroyed by the hyperthermia treatment.

Currently, hyperthermia treatment is inhibited by the inability to monitor temperature within the tumor. Temperature must be maintained within the narrow range of 43°C to 44°C over a period of time, perhaps in excess of 1 hour. Below this zone, little cell destruction occurs; above it, normal tissue destruction results. To date, little success in monitoring temperature within the tumor has been achieved using microwave or infrared techniques. Other methods, particularly invasive sensors, are undesirable due to the added health risk attendant in embedding devices in tissue. In contrast, ultrasound has the potential for providing long-term accurate temperature monitoring with minimum risk to the patient. Additionally, simultaneous imaging of the tumor and its temperature distribution can provide a convenient means of routinely assessing the progress of tumor destruction.

The initial phase of this Technology Utilization project was completed this year and involved the investigation and development of ultrasonic techniques to characterize the solid/liquid state of suitable fats or waxes and test the feasibility of using ultrasonic techniques to measure the temperature of various sizes of "indicator" beads (of fats or waxes) embedded in inhomogeneous tissue-like media. Among the materials investigated, phenyl salicylate has been found to have very good phase transformation characteristics, and its state change over the temperature gradient from 43° C to 44° C can be detected ultrasonically by the change in acoustic impedance.

Joseph S. Heyman, 3418

Lightweight Composite Wheelchair

Over 700,000 people in the United States rely on wheelchairs for mobility. Conventional chairs consist of tubular metal frames with metal wheels and typically weigh from 50 pounds to 60 pounds, which makes the chair difficult to manipulate, particularly for the elderly or handicapped person.

Since 1981, Langley Research Center and the University of Virginia Rehabilitation Engineering Center have been engaged in a cooperative project whose main objective is to develop, at a competitive cost, a foldable wheelchair weighing less than 25 pounds and having a normal complement of accessories. To accomplish this objective, extensive use of modern aerospace composite materials, which offer very high strength and low weight, was incorporated in the design. NASA Langley's role was to apply its expertise in materials technology to the selection of materials and to the design, structural analysis, and fabrication of the chair. The University of Virginia developed the design specification for the chair and will conduct the clinical evaluation.

Structurally, the chair is comprised of skinstiffened foam sandwich elements. The foam is a high-temperature polyimide, and the skins are a

combination of Du Pont Kevlar and graphite composite bonded directly to the foam core. The panel elements are 1/2 in. thick and weigh approximately 1/2 lb/ft². The hand rim (used for propelling the chair) is also formed from a foam core with a Kevlar skin covering. The backrest is a nylon-coated fiberglass cloth material which is exceptionally strong, durable, and lightweight. The collapsed dimension (thickness) of the chair is under 8 in. The prototype chairs to be used in the clinical evaluations will incorporate conventional off-the-shelf metal wheels, and in this configuration the chair weighs 23 pounds. Second-generation designs will have composite wheels, which further reduce chair weight to about 20 pounds. The first prototype chair was scheduled for delivery to the University of Virginia in early fall 1983. Two additional prototypes will be completed by the end of 1983. Clinical evaluations are expected to encompass 6 months to 1 year.

Robert M. Baucom, 4581



Lightweight composite wheelchair.

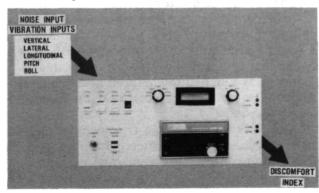
Vehicle Ride Quality Meter

In support of a NASA broad-based commuter aircraft technology requirements program, a generalized model for estimating passenger ride comfort in the presence of complex vehicle vibrations and interior noise has been developed at NASA Langley. The model (algorithm) has the unique capability of transforming individual elements of the combined

noise and vibration environment into subjective units and then combining these units to produce a single "discomfort index" typifying passenger acceptance of the environment. Over 3,000 persons were subjected to controlled testing in a simulator to produce the ride quality algorithm. As part of this research, a portable, self-contained instrument for use in obtaining real-time estimates of passenger ride comfort during actual vehicle operation was developed. This ride quality meter is a direct hardware/software implementation of the generalized ride comfort algorithm.

The ride quality meter incorporates a sensor package to simultaneously measure five axes of vehicle vibrations and includes a microphone for measuring interior vehicle noise. Signals from the vibration sensors and the microphone are fed to the ride quality meter, which processes each according to the ride comfort algorithm. A printed tape output identifies contributing sources of passenger discomfort.

The initial phase of a program to transfer this NASA technology to the commercial land vehicle industry (auto and rail) was completed this year. In a collaborative effort with the Ford Motor Company, a test program was conducted to assess the applicability of Langley's ride comfort model to the automobile ride environment. Several basic elements were involved in the test; these included measurements by Ford Motor Company of actual ride environments in several autos operating on various road surfaces, reproduction of the measured environments on the Langley ride quality simulator, subjective evaluations of the ride environments (as reproduced on the simulator) from a group of 60 passenger subjects, and correlation of passenger comfort evaluations with NASA ride comfort model estimates. Three auto models, each operating on three road surfaces, were investigated, and accelerations were measured and reproduced on the LaRC simulator. Results of this NASA-Ford Motor Company cooperative investigation clearly indicated that the ride comfort model



Ride quality meter.

performed consistently well. More significantly, the model correlated higher with passenger ratings than did standard physical metrics, such as rms acceleration.

Jack D. Leatherwood, 3561

1. Report No. NASA TM-85702	2. Government Accession No.	3. Rec	ipient's Catalog No.	
4. Title and Subtitle		5. Rep	ort Date	
Research and Technology		No	vember 1983	
1983 Annual Report of the Langley Research Center		6. Perf	orming Organization Code	
7. Author(s)		8. Perf	orming Organization Report No.	
Performing Organization Name and Address		10. Wor	k Unit No.	
NASA Langley Research Center Hampton, VA 23665			11. Contract or Grant No.	
12. Sponsoring Agency Name and Address			e of Report and Period Covered	
National Aeronautics and Space Administration				
Washington, DC 20546		14. Spo	nsoring Agency Code	
15. Supplementary Notes				
16. Abstract				
The role of the Langley Research Center is to engage in the basic and applied				
research necessary for the advancement of aeronautics and space flight, to generate				
new and advanced concepts for the accomplishment of related national goals, and				
to provide research advice, technological support, and assistance to other NASA				
installations, other government agencies, and industry. This Langley Research				
Center 1983 Annual Report on Research and Technology contains highlights of our major accomplishments and applications made during the past year. The highlights				
illustrate both the broad range of the research and technology activities at the				
Langley Research Center and the contributions of this work toward mainta				
United States leadership in aeronautics and space research. For further information				
about the report contact Robert H. Tolson, Chief Scientist, Mail Stop 103, Langley				
Research Center, Hampton, Virginia 23665, (804) 865-3316.				
17. Key Words (Suggested by Author(s))		18. Distribution Statement		
Research and technology				
		Unclassified - Unlimited		
			Subject Category 99	
19. Security Classif. (of this report) 20.	Security Classif. (of this page)	21. No. of Pages	22. Price*	
Unclassified	Unclassified	96	A05	
		I	I	

Postage and Fees Paid National Aeronautics and Space Administration NASA-451



Washington, D.C. 20546

Official Business
Penalty for Private Use, \$300

H.F. Wochholz

Vice President Engineering
MCDONNELL-DOUGLAS CORPORATION
McDonnell Douglas Electronics Co.
2600 N. Third Street
St. Charles, Missouri 63301

NHQ FORM 150A NOV 81

NASA

POSTMASTER:

If Undeliverable (Section 158 Postal Manual) Do Not Return

6 MAR84 CT R. R. Denn 1313/33/48/496 4 MAY 14 S 3 JUL 1980 7. G. Lacry 341/32/282/34414 113 AUG